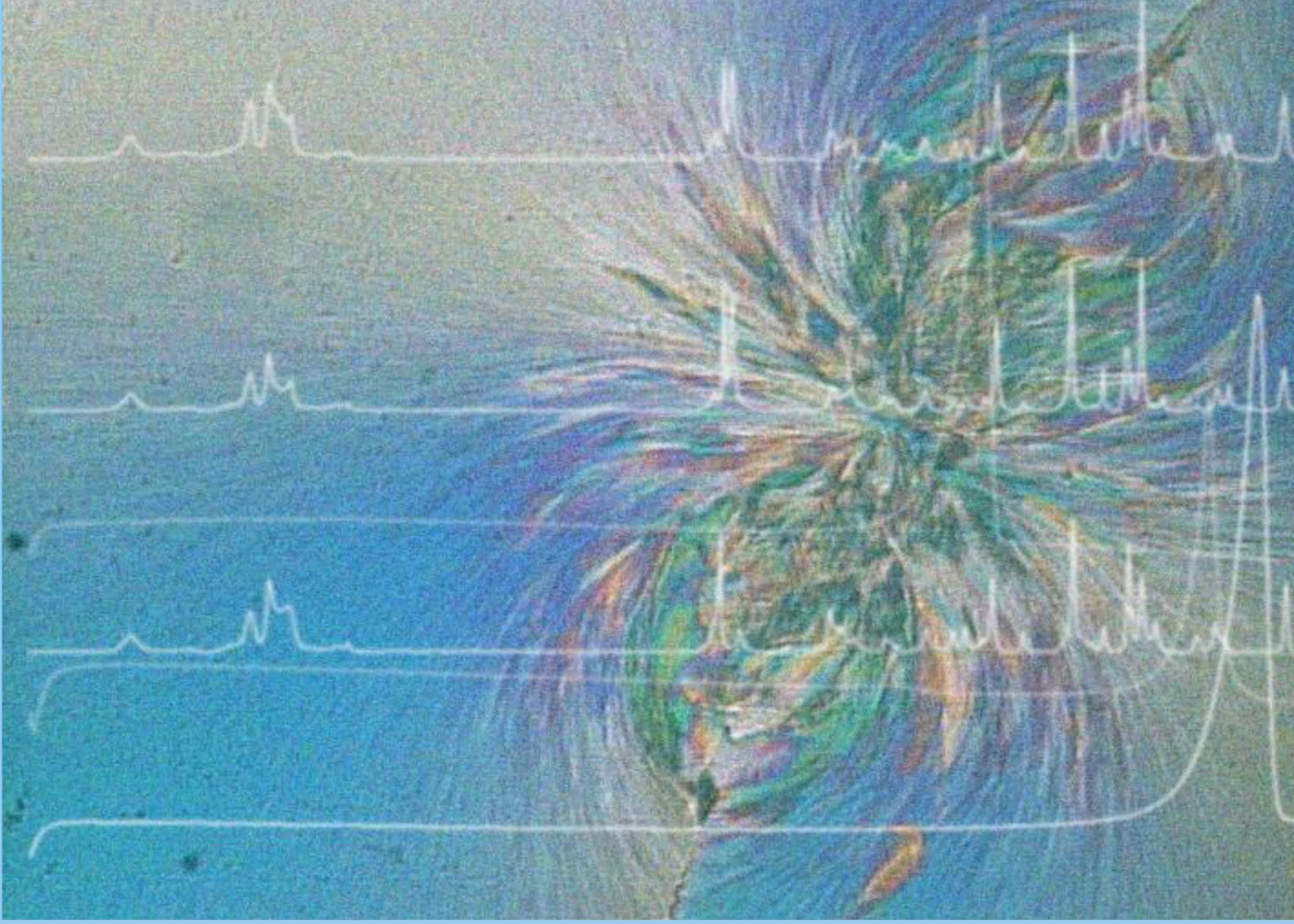

Bernardo Albuquerque Nogueira

Structural and Spectroscopic Characterization of Hydantoins, Investigation of their Thermal Properties, and of their Photochemistry in Cryogenic Matrices

Mestrado em Química

Departamento de Química

FCTUC

Setembro 2016

· U C ·

Universidade de Coimbra

Bernardo Albuquerque Nogueira

Structural and Spectroscopic Characterization of Hydantoins, Investigation of their Thermal Properties, and of their Photochemistry in Cryogenic Matrices

Dissertação apresentada para provas de Mestrado em Química,
Área de Especialização em Química Avançada e Industrial

Orientador: Professor Doutor Rui Fausto M. R. S. Lourenço

Setembro de 2016

Universidade de Coimbra

"If you're walking down the right path and you're willing to keep walking, eventually you'll make progress."

Barack Obama

Acknowledgements

First of all, I would like to thank to Prof. Rui Fausto, group leader and my supervisor, for giving me the opportunity to work at Laboratory for Molecular Cryospectroscopy and Biospectroscopy (LMCB) of the Department of Chemistry, Faculty of Science and Technologies of the University of Coimbra, for the last three years. It is my will that this is just the beginning of a long journey at LMCB. I also owe Professor Rui Fausto a special thanks for all his guidance, support and encouragement in many different ways, throughout the course of this Thesis.

To Profs. Maria Ermelinda Eusébio and João Canotilho I would like to thank for the kind welcome at the Molecular Thermodynamics and Solid State Chemistry Laboratory, and for all the help in the investigation of the thermal properties of the studied compounds. I sincerely wish that this collaboration can be continued and developed in the future.

I also owe a very special acknowledgement to Dr. Gulce O. Ildiz for all her help and patience in the beginning of this project, when I first joined LMCB. Her words of guidance were absolutely decisive for the development of all this study.

I also thank all the members of LMCB for the supportive words and companionship.

To Prof. Doutor José António Paixão and Marta Henriques, Centro de Estudos de Materiais por Difracção de Raios-X (CEMDRX), I owe an ackowladgement for their availability to perform the single crystal X-ray measurements.

To Joana Cunha, a special thanks for the help in the design of the lovely cover image.

To the Department of Chemistry, Faculty of Science and Technologies of the University of Coimbra, and to the Portuguese Foundation for Science and Technology I thank for having provided the financial support and facilities used in this study, and for the grant that helped me to accomplish this project.

To all my friends, especially to all of those from Braga and Coimbra, who felt my absence in important moments of their lives and even so were there to cheer me up whenever I needed, I owe a very special acknowledgement.

To my parents, brothers and sister I owe a very special acknowledgement for the unconditional encouragement and for being always there for me. I would also like to thank to my aunt and godmother Alexandra for the scientific advices and support throughout these years.

I am also very grateful to Carolina, for all the support, without which would be impossible to accomplish this goal.

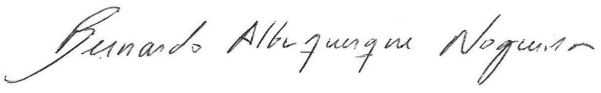

Table of Contents

Abbreviations

1-MH: 1-Methylhydantoin

5-HAA: 5-Hydantoin acetic acid

5-MH: 5-Methylhydantoin

ATR: Attenuated Total Reflectance

DFT: Density Functional Theory

DSC: Differential Scanning Calorimetry

DTGS: Deuterated Triglycine Sulfate detector

FIR: Far-infrared

FTIR: Fourier Transform Infrared Spectroscopy

GGA: Generalized Gradient Approximation

H-bond: Hydrogen Bond

HF: Hartree-Fock

HIV: Human immunodeficiency virus

HK theorems: Hohenberg-Kohn theorems

HSAB theory: Hard and soft (Lewis) acids and bases theory

IR: Infrared

LDA: Local Density Approximation

LP: Lone electron pair orbital

LSDA: Local Spin Density Approximation

MIR: Mid-infrared

MP: Møller-Plesset

NBO: Natural Bond Orbital

NIR: Near-infrared

NMR: Nuclear Magnetic Resonance

PED: Potential Energy Distributions

PLTM: Polarized Light Thermal Microscopy

Ry: Rydberg type orbital

T_{fus}: Melting point

THF: Tetrahydrofuran

UV: Ultraviolet

XRD: X-ray diffraction

$\Delta_{fus}H$: Enthalpy of fusion

λ: Wavelenght

Resumo

Neste trabalho foi realizado o estudo estrutural e vibracional da 1-metil-hidantoína (1-MH, $C_4H_6N_2O_2$), 5-metil-hidantoína (5-MH, $C_4H_6N_2O_2$), e 5-carboximetil-hidantoína (5-HAA, $C_5H_6N_2O_4$) por espectroscopia de infravermelho com isolamento em matriz (matriz de árgon; 10 K) complementado por cálculos de química quântica DFT (B3LYP)/6-311++G(d,p). Os cálculos teóricos apresentaram a simetria C_s para 1-MH e a simteria C_1 para 5-MH e 5-HAA como as estruturas de energia mínima na superfície de energia potencial destas moléculas. As estruturas electrónicas destes mínimos energéticos de cada moléula foram estudadas em detalhe por análise das suas orbitais naturais de ligação, permitindo a caracterização dos seus sistemas electrónicos σ e π. As atribuições completas dos espectros de infravermelho das moléculas 1-MH, 5-MH e 5-HAA foram feitas com a ajuda dos espectros dos compostos previstos teoricamente.

A fotoquímica induzida por UV ($\lambda \geq 230$ nm) dos monómeros da 1-MH também foi estudada. Foi constatado que a molécula da 1-MH se fragmenta em monóxido de carbono, ácido isociânico, N-metil-metilenimina e em metilenimina por dois caminhos de reacção diferentes.

A investigação das propriedades térmicas dos três compostos foi realizada por calorimetria diferencial de varrimento (DSC), termomicroscopia da luz polarizada (PLTM) e espectroscopias de infravermelho e de Raman. Foi identificada uma nova forma polimórfica do composto 1-MH, que foi caracterizada estruturalmente pela primeira vez por difração de raios-X de monocristal. Foram também identificados quatro polimorfos diferentes da 5-MH, tendo sido caracterizados por espectroscopia de Raman. Por último, por PLTM foi possível observar a existência de cinco formas polimórficas da 5-HAA, sendo que quatro desses polimorfos foram caracterizados por espectroscopia de Raman.

Foram sintetizados três novos complexos de coordenação com o composto 1-MH. Os diferentes tipos de ligação do ião metálico com o ligando 1-MH foram investigados e identificados por espectroscopia de Raman, tendo-se verificado que as ligações de coordenação nos complexos estudados estão de acordo com o conceito HSAB.

Abstract

In this Thesis, the structural and vibrational study of 1-methylhydantoin (1-MH, $C_4H_6N_2O_2$), 5-methylhydantoin (5-MH, $C_4H_6N_2O_2$), and 5-hydantoin acetic acid (5-HAA, $C_5H_6N_2O_4$) was performed by matrix isolation infrared (IR) spectroscopy (in argon matrix; 10 K), complemented by quantum chemical calculations performed at the DFT (B3LYP)/6-311++G(d,p) level of approximation. The theoretical calculations yielded the C_s symmetry for 1-MH and the C_1 symmetry for 5-MH and 5-HAA minimum energy structures on the ground state potential energy surfaces of the molecules. The electronic structure of these minimum energy species were then studied by means of the natural bond orbital (NBO) approach, allowing the elucidation of the main characteristics of the σ and π electronic systems of the molecules. The IR spectra of the matrix-isolated 1-MH, 5-MH and 5-HAA were fully assigned, also with the help of the theoretically predicted spectra of the compounds.

The UV-induced photochemistry ($\lambda \geq 230$ nm) of the 1-MH matrix-isolated monomer was also studied. The 1-MH molecule was found into fragment to carbon monoxide, isocyanic acid, *N*-methyl-methylenimine and methylenimine, *via* two different reaction pathways.

The investigation of the thermal properties of 1-MH, 5-MH and 5-HAA was undertaken by differential scanning calorimetry (DSC), polarized light thermal microscopy (PLTM) and infrared and Raman spectroscopies. A new polymorph of 1-MH was identified and characterized structurally for the first time by single crystal X-ray diffraction. Four different polymorph of 5-MH were identified and characterized spectroscopically by Raman spectroscopy. PLTM experiments allowed the observation of five different polymorphs of 5-HAA, four of them being characterized by Raman spectroscopy.

Finally, three novel coordination complexes of 1-MH were synthesized. The different types of bonds between the metal ion and the 1-MH ligand were investigated and identified by Raman spectroscopy, and found to be in agreement with the HSAB principle.

Chapter 1
Introduction

Chapter 1

Introduction

1.1 1-methylhydantoin, 5-methylhydantoin and 5-hydantoin acetic acid

1-methylhydantoin (Scheme 1.1), 5-methylhydantoin (Scheme 1.2) and 5-hydantoin acetic acid (Scheme 1.3) are compounds that belong to the hydantoin family. Hydantoins are heterocyclic organic compounds that derive from imidazolidine, with two carbonyl groups bounded to C2 and C4 atoms. Hydantoins may have substituents bounded to the remaining atoms of the ring, namely at N1, N3 and C5 positions. This family of compounds shows relevant physiological activities, particularly as anticonvulsive, anti-inflammatory, anti-epileptic and anticancer drugs.[1–5] Moreover, the use of some substituted hydantoins has also been suggested for the treatment of HIV-1.[6,7] Despite the practical relevance of hydantoins, specifically in the pharmaceutical field, there are not many studies on their electronic structures, spectroscopic and thermal properties and photochemistry. In fact, most of the reported studies on hydantoins deal with the determination of their crystal structures and the investigation of chirality effects in the solid state, as the asymmetrically substituted hydantoins in C5 position are enantiomeric compounds.[8–14]

Our research group has recently investigated the parent hydantoin ($C_3H_4N_2O_2$).[15,16] Monomers of the compound were isolated in an argon matrix a 10 K, and their structure, vibrational properties and unimolecular photochemistry were studied by infrared spectroscopy, complemented by quantum mechanical calculations.[16] In the crystalline state (monoclinic $C2/c$; Z = 8),[14] hydantoin molecules are linked by N−H···O hydrogen bonds, forming chains where each molecule is connected to its two neighbors in a total of four H-bonds, and the average enthalpy per H-bond and r(N···O) H-bond distance amount to −11.2 kJ mol^{-1} and 0.288 nm, respectively.[14,16] Upon UV-irradiation (λ = 230 nm) of matrix-isolated hydantoin, photochemical transformation of the compound was observed, leading to the formation of isocyanic acid (HNCO), carbon monoxide and methylenimine (H_2C=NH).[16] H-bonded dimers of the compound have also been theoretically investigated[15], and simple correlations extracted, which relate the shifts in the NH stretching and bending modes with H-bond formation.

1-methylhydantoin (1-MH; see Scheme 1.1) is one of the smallest and structurally simplest substituted hydantoins, with a single methyl substituent at N1. Substituted hydantoins at the nitrogen atoms have been shown to induce growth inhibition followed by apoptosis in leukemia cells, and their cytotoxity found to be substantially influenced by the nature of the substituents.[1,3]

Scheme 1.1 1-methylhydantoin molecule, with atom numbering.

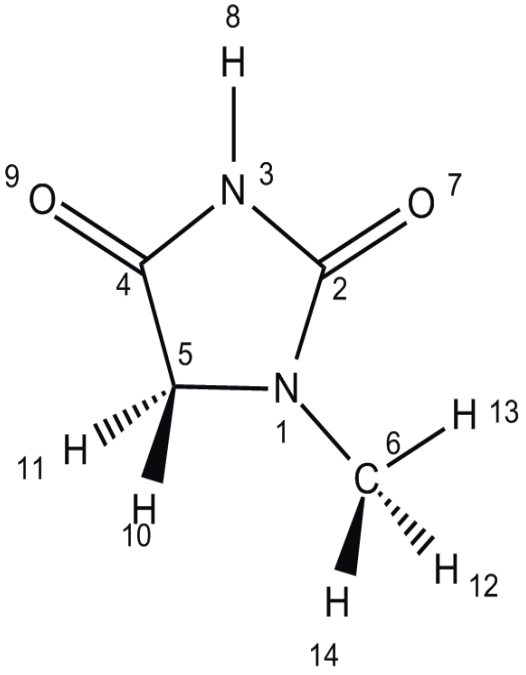

The present work on 1-MH aims to shed light on the details of its electronic structure (in particular performing a detailed investigation of the σ and π electronic systems of the molecule in the ground electronic state), to interpret its infrared spectrum and investigate its photochemistry. This investigation also includes the thermal study of the neat compound, using infrared and Raman spectroscopies, differential scanning calorimetry (DSC) and polarized light thermal microscopy (PLTM). A new polymorph of 1-MH was successfully identified and its crystalline structure was resolved by single crystal X-ray crystallography. Finally, three metal complexes with the 1-MH ligand were synthesized, which were then investigated by Raman spectroscopy.

5-methylhydantoin (5-MH; see Scheme 1.2) is other of the structurally simplest substituted hydantoins, bearing, in this case, a single methyl substituent at C5 position. Therefore, 5-MH is an enantiomeric compound, as it is an asymmetrically substituted hydantoin.

The present study on 5-MH is focused on the detailed characterization of the electronic structure of the molecule, with special emphasis on the characterization of the *σ* and *π* systems in the electronic ground state. This work also includes the interpretation of the infrared spectrum of monomeric 5-MH. The thermal investigation of the neat compound was also undertaken, particularly of its polymorphs, which were identified and studied by Raman spectroscopy, DSC and PLTM techniques.

5-hydantoin acetic acid (5-HAA; see Scheme 1.3) is still a simple hydantoin, though the substituent that is bonded to the C5 atom is a structurally more complex group than that presented in both 1-MH and 5-MH. 5-HAA is also an enantiomeric hydantoin.

Scheme 1.2 5-methylhydantoin molecule, with atom numbering.

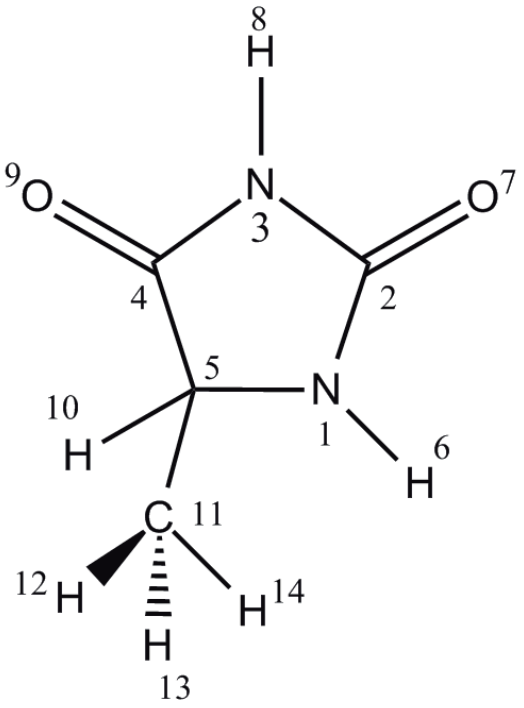

Scheme 1.3 5-hydantoin acetic acid molecule, with atom numbering.

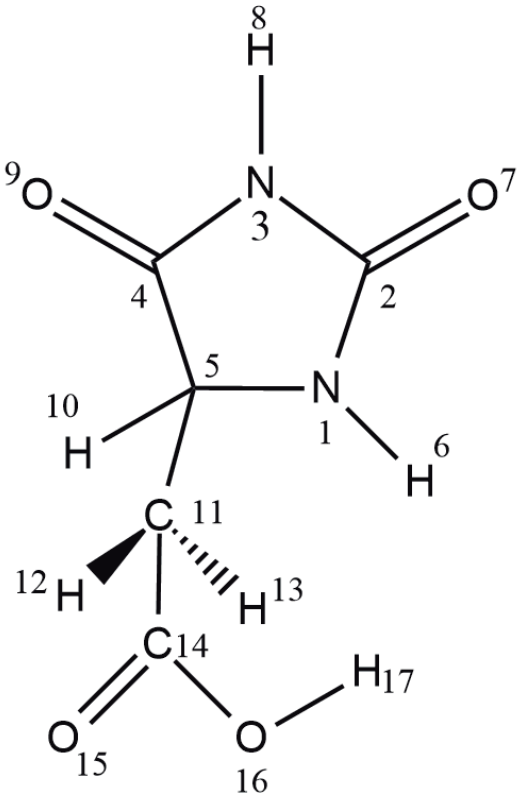

As for the remaining hydantoins studied in this project, the electronic structure of 5-HAA in particular the electronic ground state was investigated in detail, and the study of its infrared spectrum was also undertaken. The present work on 5-HAA also includes its thermal investigation, particularly of its polymorphism, by using different experimental techniques (Raman spectroscopy and PLTM).

1.2 Theoretical methods

1.2.1 Density Functional Theory

The Density Functional Theory (DFT) method is nowadays one of the most used computational approach in chemistry due to its high computational efficiency and very good accuracy compared to both Hartree-Fock (HF) and Møller-Plesset (MP) perturbation methods.[17–20] The main advantage of DFT is that the system under analysis is defined in terms of its electronic density, $\rho(\vec{r})$, instead of in terms of a wave function (as in HF and MP methods).

Considering a system with *n* electrons, $\rho(\vec{r})$ represents the total electron density at a particular point in space, r. The electronic energy is regarded as a functional of the electron density, $E[\rho(\vec{r})]$.

The Hohenberg-Kohn theorems (HK theorems) relate the electron density with the energy and other properties of the system. The HK Existence Theorem demonstrates that all properties of a molecule in the ground electronic state are uniquely defined by $\rho(\vec{r})$, and the HF Variational Theorem affirms that only the functional with the ground state density input delivers the lowest energy to the ground state energy of the system.[21]

In the present days, DFT calculations are based on Kohn and Sham approach,[22] that allowed to overcome the problems related to the kinetic energy functional definition, by splitting it in two parts, one considering the non-interacting electrons, that can be calculated exactly, and the other one being a small correction term accounting for electron-electron interactions.

$E[\rho(\vec{r})]$ can be expanded in terms of the electronic kinetic energy, E_T, the nuclear-electronic attraction potential energy, E_V, a classic Coulombic inter-electronic repulsion term, E_J, and the so-called exchange correlation-energy functional, E_{XC}:

$$E[\rho(\vec{r})] = E_T[\rho(\vec{r})] + E_V[\rho(\vec{r})] + E_J[\rho(\vec{r})] + E_{XC}[\rho(\vec{r})] \quad (1.1)$$

There are many approximations in order to calculate the electron exchange-correlation functional. The simplest approximation is the Local Density Approximation (LDA), which assumes that the electron density is uniform throughout the molecule. The LDA exchange-correlation energy functional can be written as:

$$E_{XC}^{LDA}[\rho] = \int \rho(\vec{r})\, \varepsilon_{XC}(\rho(\vec{r}))\, \mathrm{d}\vec{r} \tag{1.2}$$

where $\varepsilon_{XC}(\rho(\vec{r}))$ is the exchange-correlation energy per particle of uniform gas of density $\rho(\vec{r})$. The $\varepsilon_{XC}(\rho(\vec{r}))$ term can be further divided into two different terms, the exchange energy, ε_X, and the correlation energy, ε_C.[23–25]

Though LDA yields good results for certain systems, as the simplest approximation for $E_{XC}[\rho(\vec{r})]$, that is not the case for the majority of molecules. Since the electron density is not uniform in most of the molecules, there was a need to create functionals that combine electron density and gradient corrections, the Generalized Gradient Approximation (GGA) methods. The GGA exchange-correlation energy functional can be written as:

$$E_{XC}^{GGA}\left[\rho^{\alpha}, \rho^{\beta}\right] = \int f(\rho^{\alpha}(\vec{r}), \rho^{\beta}(\vec{r}), \nabla\rho^{\alpha}(\vec{r}), \nabla\rho^{\beta}(\vec{r}))\ \mathrm{d}\vec{r} \tag{1.3}$$

where f is any given function of the spin densities $\rho^{\alpha}(\vec{r})$ and $\rho^{\beta}(\vec{r})$, and of their corrected gradients $\nabla\rho^{\alpha}(\vec{r})$ and $\nabla\rho^{\beta}(\vec{r})$. As for the LDA, the GGA exchange-correlation energy can also be split into two parts, exchange and correlation energies.[17–20]

Hybrid methods, which combine exchange and correlation energy functionals from *ab initio* or empirical sources with the Hartree-Fock exact exchange energy functional, have also been developed. Among the most common and widely used hybrid functionals are the exchange functional created by Becke in 1988 (B ou B88)[26], the exchange functional developed by Pardew and Wang in 1986 (PW86)[27] and modified in 1991 by the same authors (PW91),[28] and the correlation functional of Lee, Yang and Parr (LYP).[29,30]

The hybrid functional used in this work, B3LYP,[26,29–31] is one of the most popular functional used in theoretical calculations nowadays, and can be written as:

$$E_{XC}^{B3LYP} = (1-a)E_X^{LSDA} + aE_X^{HF} + b\Delta E_X^{B} + (1-c)E_C^{VWN} + cE_C^{LYP} \tag{1.4}$$

where E_X^{LSDA} is the exchange energy functional using the Local Spin Density Approximation (LSDA), E_X^{HF} is the HF exact exchange functional, and E_C^{VWN} is the correlation functional developed by Vosko, Wilk and Nusair (VWN).[31] The three Becke parameters (a, b and c) have the values of 0.2, 0.72 and 0.81, respectively. E_X^{B}, the exchange functional created by Becke, can be written as:

$$E_X^{B} = E_X^{LSDA} - b\sum_{\sigma=\alpha,\beta}\int \frac{(\rho^{\sigma})^{\frac{4}{3}}\chi_{\sigma}^{2}}{1+6b\chi_{\sigma}\sinh^{-1}\chi_{\sigma}}\ \mathrm{d}\vec{r} \tag{1.5}$$

where $\chi_{\sigma} \equiv \left|\nabla_{\rho}\right|/(\rho^{\sigma})^{4/3}$ and b is an empirical parameter, usually equal to 0.042 atomic units.

LYP, the correlation functional of Lee, Yang and Parr, can be written as:

$$E_C^{LYP} = -a \int \frac{\rho + b\rho^{2/3}\,[t_{HF} - 2t_W]\, e^{c\rho^{1/3}}}{1 + d\rho^{1/3}} \tag{1.6}$$

where a, b, c and d are constants (0.049, 0.132, 0.2533 and 0.349, respectively) and t_{HF} and t_W are the kinetic energy density of Hartree-Fock and Weizsacker, respectively.

1.2.2 Basis sets

In this work, the standard 6-311++G(d,p) basis set, where the molecular orbitals are defined by linear combinations of Gaussian-type atomic functions, was used.[32] This is a triple-ζ (TZ) basis set, where each valence atomic orbital is split in a more compact inner shell and a more diffuse outer shell. 6-311 means that the core orbitals are represented by six Gaussian-type atomic functions, and the valence orbitals are represented by three contracted Gaussian-type atomic functions and two independent single Gaussian-type atomic functions. Additionally, ++ represent the added diffuse functions, which correspond to small coefficient generic functions used to describe regions of space far away from the center to where they are attached.[33] Diffuse functions are necessary for correct description of weak bonds or anions and are frequently used for calculations of such properties as polarizabilities, dipole moments, hydrogen bonds, etc. The 6-311G(d,p) basis set also includes polarization functions, which are included to add some additional flexibility to the basis set and are important to represent accurately the atom bonds within a molecule (in this case, d-type orbitals and p-type orbitals are used in the description of the non-hydrogen and hydrogen atoms, respectively).[34]

1.2.3 Normal Coordinate Analysis

The characterization of the vibrational modes can be obtained from the normal coordinate analysis. The normal coordinate analysis is usually performed using the Wilson's FG method.[35] This method is based on the classical mechanics and allows the calculation of the normal mode frequencies in terms of the force constants, masses and geometry of a molecule. It is also possible, through this formalism, to obtain the composition of each vibrational normal mode in terms of internal (or symmetry) coordinates as described by the elements of the potential energy distribution (PED) matrix.[36,37]

A molecule with N atoms has 3N–6 non-redundant internal coordinates (3N–5 for linear molecules) that allow to describe its vibrations. Briefly, according to the laws of the classical mechanics, the vibrational energy of a molecule can be described as the sum of kinetic and potential energies.

The kinetic energy, *T*, can be described in terms of the internal coordinates by the matrix equation:

$$T = \frac{1}{2}\, \boldsymbol{D'^{t} G^{-1} D'} \tag{1.7}$$

and the potential energy, V, by the matrix equation:

$$V = \frac{1}{2}\,\boldsymbol{D^t F D} \tag{1.8}$$

Where $\boldsymbol{D}$ and $\boldsymbol{D'}$ represent column vectors of the internal coordinates and their time derivatives, respectively, $\boldsymbol{F}$ is the force constant matrix in terms of the internal coordinates and $\boldsymbol{G}$ is a matrix that is related to the reduced mass of the various molecular oscillators.
The G matrix can be defined as:

$$\boldsymbol{G = B\,M^{-1}\,B^t} \tag{1.9}$$

where $\boldsymbol{M^{-1}}$ is a (3N x 3N) diagonal matrix containing the inverse nuclear masses and $\boldsymbol{B}$ is a matrix that converts the Cartesian displacement coordinates, $\boldsymbol{R}$, into the internal coordinates of the molecule, $\boldsymbol{D}$:

$$\boldsymbol{D = BR} \tag{1.10}$$

The normal coordinates of a molecular system, *i.e.*, the nuclear movements in a molecule along the vibrations, can be defined as a vector, $\boldsymbol{Q}$, which is related with the internal coordinates by a linear transformation:

$$\boldsymbol{D = LQ} \tag{1.11}$$

where, $\boldsymbol{L}$ is the matrix resulting from the juxtaposition of the 3N–6 eigenvectors of the $\boldsymbol{FG}$ matrix.
In this way, the kinetic and potential energies are given by the following matrix equations:

$$T = \frac{1}{2}\boldsymbol{Q'^t L^t G^{-1} L Q'} = \frac{1}{2}\boldsymbol{Q'^t E Q'} \tag{1.12}$$

$$V = \frac{1}{2}\boldsymbol{Q^t L^t F L Q} = \frac{1}{2}\boldsymbol{Q^t \Lambda\, Q} \tag{1.13}$$

where $\boldsymbol{E}$ is the diagonal identity matrix and $\boldsymbol{\Lambda}$ is the diagonal matrix formed by the eigenvalues of the $\boldsymbol{FG}$ matrix, which are related to the vibrational frequencies: $\lambda_i = 4\pi^2 \nu_i{}^2$, where ν_i represents the frequency of a vibrational mode identified as *i*.
Combining the equations (1.12) and (1.13), the vibrational energy of a molecule within the mechanical harmonic approximation is obtained:

$$E_{vib} = \frac{1}{2}\boldsymbol{Q'^t E Q'} + \frac{1}{2}\boldsymbol{Q^t \Lambda\, Q} \tag{1.14}$$

Since $\boldsymbol{L^t G^{-1} L = E}$ or $\boldsymbol{L^t = L^{-1} G}$, and $\boldsymbol{L^t F L = \Lambda}$,

$$\boldsymbol{L^{-1}FGL = \Lambda} \tag{1.15}$$

The determination of the normal coordinates is therefore equivalent to find the $\boldsymbol{L}$ matrix that diagonalizes the product $\boldsymbol{FG}$, by a similarity transformation. The solution of such linear system of homogenous equations implies the resolution of the secular determinant given by the equation:

$$|\boldsymbol{FG} - \boldsymbol{E}\lambda_i| = 0 \tag{1.16}$$

The roots of this equation, λ_i, are the eigenvalues of the product matrix $\boldsymbol{FG}$. Each eigenvalue is corresponded by a group of eigenvectors, $\boldsymbol{L_i}$, which determine the form of the vibrational normal modes.

In order to characterize the different vibrational normal modes of a molecule, the potential energy distribution (PED) in terms of contributions associated to each force constant of the internal coordinates can be used. For a given vibrational mode, the kinetic energy term is zero when the atoms are in their maximum distance from the equilibrium position. The vibrational energy is, thereby, equal to the potential energy, which is proportional to λ_i. In turn, the latter is related to the normal coordinate $\boldsymbol{Q_i}$ (see Equation 1.13) and can be expanded in terms of the force constants and internal coordinates, as:

$$\boldsymbol{L_i^t F L_i} = \lambda_i \tag{1.17}$$

The first member of this equation corresponds to the following sum:

$$\sum_{(\alpha,\beta)} \boldsymbol{L_i^{\alpha} L_i^{\beta} F_{(\alpha,\beta)}} \tag{1.18}$$

where the indexes α and β refer to the internal coordinates. Then, the potential energy distribution by the different force constants, $\boldsymbol{F_{(\alpha,\beta)}}$, is given in percentage by the equation:

$$[PED]_i^{\boldsymbol{F_{(\alpha,\beta)}}} = \frac{100\, \boldsymbol{L_i^{\alpha} L_i^{\beta} F_{(\alpha,\beta)}}}{\lambda_i} \tag{1.19}$$

In this Thesis, the normal coordinate analysis of the infrared spectra of 1-MH, 5-MH and 5-HAA molecules and the corresponding characterization of the PEDs were realized with the help of the programs, referred to in Section 2.1.2.

1.3 Matrix isolation spectroscopy

The expression matrix isolation was firstly introduced by Pimentel, Whittle and Dows,[38] in 1954, to describe the technique of trapping guest molecules or atoms in solidified host gases (inert gases in most cases and occasionally reactive gases).[39,40] The purpose of the matrix isolation method is to simulate the gas phase for the investigated species by surrounding it with an inert and transparent solid (often rare gas solids such as Ar, Kr, Xe, or cryogenic solids as N_2, O_2, CO, CH_4), so that the interactions between the solute molecules are negligible, as in the case of molecules in the gas phase.

The extremely low working temperatures (usually around 10 K or even lower) allow species that are normally short-lived, such as reactive intermediates and other unstable species resulting from chemical processes, to be preserved and studied with convenience. A variety of spectroscopic methods can then be applied to the detection and characterization of the trapped species, as infrared, ultraviolet/visible, nuclear magnetic resonance (NMR) and Raman spectroscopies.

The low concentration of the trapped species makes negligible the interactions between guest molecules, while the usual chemical inertia of the host minimizes host-guest interactions. This leads to a decrease in the dispersion of the vibrational levels, increasing spectral resolution and facilitating the comparison of the experimental spectra with theoretical results, which normally treat the molecule like an isolated species *in vacuo*. Nowadays, the interpretation of experimental IR spectra is greatly simplified due to the development of accurate theoretical methods for their calculation, such as those relying on Density Functional Theory (DFT) approaches complemented by a classic harmonic or even anharmonic treatment of molecules vibrations.[41]

The rigidity of the matrix inhibits diffusion of the molecules and minimizes aggregation, contributing also to increase the spectral resolution. Furthermore, when the trapped molecules are made to react by *in situ* irradiation with UV light, in general the fragments resulting from the precursor species are unable to escape from the matrix cage where they were formed, precluding cross recombination reactions between fragments originated in different molecules. Such feature strongly simplifies the possible chemistry, thus making matrix isolation a very useful method to study reaction mechanisms. Photochemical excitation by UV irradiation of the matrix-isolated molecules can yield new species by photofragmentation of the original molecules or by its structure rearrangement, either through bond cleavage and bond formation or by conformational isomerism.[40,42–49]

Significant sharpening of the bands and increase in the peak intensities are observed in matrix isolation when compared to spectra obtained in most of common experimental conditions, where bands due to different vibrations are frequently overlapped. However, caution should still be taken in the band assignment, since it is frequent that matrix isolation spectral bands show splittings caused by matrix (or site) anisotropy. Thus, the nature of the observed splittings can be due to different chemical species (different conformers, for example) or to the same species in different trapping sites. Changing the matrix host is the most common method for distinguishing between these two possibilities. This procedure usually does not have a significant effect on the

bands due to different chemical species but produces a drastic change in the profile of the signals due to distinct trapping sites.

A matrix-isolated sample can be prepared by deposition of a pre-mixed gaseous mixture or by co-deposition of the species to be studied (or a suitable precursor) and the host gas. In both situations, the gas mixture is directed towards a cold window kept typically in the 4-60 K temperature range and at very low pressure (10^{-8} – 10^{-10} atm) inside a cryostat.

Matrix isolation is a a quite powerful technique to investigate aggregation and H–bonding, since control of temperature of a pre-deposited matrix (or of the substrate, during deposition) can allow to efficiently control the levels of aggregation in a sample. The technique is then suitable for study of dimers and small aggregates.[50–54]

1.4 Molecular Spectroscopy

There are two main types of molecular spectroscopy, absorption spectroscopy and emission spectroscopy. In the first case, a molecule undergoes a transition from a lower energy state to a state of higher energy, when it absorbs a photon. This typically occurs between the ground state E_0 and the first excited state E_1, for example, in infrared spectroscopy (Section 1.5.1). Oppositely, in emission spectroscopy, the molecule goes from a higher energy state E_1 to a state of lower energy E_0, emitting a photon. The photon absorbed or emitted, has the energy of $E = h\nu$, which can be defined as:

$$h\nu = |E_0 - E_1|(1.20) \quad (1.20)$$

where h is the Planck constant (6.626 x 10^{-34} J Hz^{-1}), ν is the frequency of the radiation absorbed or emitted and, E_0 and E_1 represent the lower and higher energy states, respectively.

However, there is an alternative way to study the difference on the energy between two states, specifically between two vibrational states, that can be explored by examining the frequencies that exist in the radiation scattered by the molecules, such as in Raman Spectroscopy, as it will be described in Section 1.5.2. [36,55]

The molecular spectroscopy techniques used in this work are infrared and Raman spectroscopies that are briefly described below.

1.4.1 Infrared Spectroscopy

Infrared (IR) spectroscopy is a spectroscopy technique aiming to investigate the vibrations of the atoms in a molecule. Commonly, an infrared spectrum is collected by making a light beam in the infrared region pass through a sample and analyzing the fraction of the incident radiation that is absorbed at each frequency.

Roughly, the frequencies where the peaks appear in an infrared spectrum correspond to the frequencies of the vibrations of the sampled molecules.

A vibration that can lead to absorption of infrared light must obey to a specific feature: the electric dipole moment of the molecule must change during the vibration, so that its derivative at equilibrium geometry does not vanish. Therefore, homonuclear diatomic molecules are inactive in IR spectroscopy, as their dipole moments remain zero along the vibration, while heteronuclear diatomic molecules are infrared active.

Infrared radiation can be divided in three main regions, known as near-infrared (NIR), mid-infrared (MIR) and far-infrared (FIR) that cover the wavelength of 0.7-1.4, 1.4-15 and 15-1000 μm respectively, corresponding to the wavenumbers of ca. >4000, 4000-400 and <400 cm^{-1}, respectively. In infrared spectroscopy, the region most commonly used is MIR, since the common spectra are collected between approximately 4000 and 400 cm^{-1}.

The relationship between the intensities of the incident light (I_0) and the transmitted IR radiation (I) and the analyte concentration (c) is generally given by the Beer-Lambert law

$$A = \frac{I_o}{I} = \varepsilon\, c\, l \tag{1.21}$$

where A is the absorption of the analyte, ε is the molar absorption coefficient and l represents the thickness of the sample.

In terms of quantum mechanics, the infrared absorption is an electric dipole operator mediated transition where the variation in the dipole moment, μ, with respect to a change in a vibrational amplitude, Q, is greater than zero

$$\left(\frac{\delta\mu}{\delta Q}\right)_0 \neq 0 \tag{1.22}$$

The measured IR band intensity, A; corresponding to the vibration, Q, is proportional to the square of the change in the dipole moment during that vibration

$$A \propto \left(\frac{\delta\mu_x}{\delta Q}\right)_0^2 + \left(\frac{\delta\mu_y}{\delta Q}\right)_0^2 + \left(\frac{\delta\mu_z}{\delta Q}\right)_0^2 \tag{1.23}$$

Nevertheless, the fact that a molecular vibration changes the electric dipole moment of the molecule is not enough for that vibration to be observed in an IR spectrum, since sometimes its intensity is too low to be detected.

There are some factors that may complicate the interpretation of an infrared spectrum, such as the appearance of an overtone or Fermi resonances. Overtone frequencies are nearly multiples of the fundamental absorption frequency. For a stretching vibration the energy required for the first overtone transition is slightly less than twice the fundamental, due to the anharmonicity of the vibration. The Fermi

resonances appear when two transitions (one fundamental and on overtone or combination tone) are nearly degenerate and belong to the same symmetry species, and give rise to characteristic (Fermi) doublet spectral features.[55,36,56–58]

1.4.2 Raman Spectroscopy

Raman scattering spectroscopy is less widely used than infrared absorption, mainly because of the problems with sample degradation and fluorescence found in Raman spectroscopy. Nevertheless, the recent advances in instrumentation have simplified the equipment and reduced those problems significantly. There is also the possibility to conjugate an optical microscope with Raman spectroscopy, leading to the Confocal Raman Microspectroscopy technique, which was used in the present work.

The Raman scattering consists in the phenomena of inelastic scattering of light and was first postulated by Smekal in 1923[59] and observed experimentally for the first time in 1928 by C. V. Raman and K. S. Krishnan[60] and independently by G. Landsberg and and L. Mandelstam.[61] Raman was rewarded with the Nobel Prize in Physics in 1930 due to "*his work on the scattering of light and for the discovery of the effect named after him*".[62]

Besides the possibility of a photon to be absorbed when light interacts with a sample, there is also the possibility of a photon to interact with matter by scattering from it. That is what happens in Raman spectroscopy and, contrarily to IR spectroscopy, there is no need for the photon to have the same energy of the difference between two energy levels of the molecule. In Raman spectroscopy, the sample is irradiated with a single frequency beam that can be scattered from the molecule one vibrational unit different from the incident beam, and then detected.

In Raman scattering, the light beam interacts with the molecule polarizing (or distorting) the electron cloud around the nuclei to produce a virtual unstable short-lived state that quickly re-radiate a photon.

If only the cloud of electron is distorted in scattering, the photons will be scattered with very small or zero frequency changes, since the electrons are very light compared to the nucleus. This elastic process is the dominant scattering process, and it is known as Rayleigh scattering. Oppositely, if nuclear motion is induced during the scattering process, there will be energy transfer either from the incident photon to the molecule or from the molecule to the scattered photon. This is the Raman scattering, an inelastic scattering process where the energy of the scattered photon is different from the incident one by one vibrational unit. Thus, the selection rule for vibrational Raman scattering is that the polarizability should change as the molecule vibrates

Raman scattering is an inherently weak process, since only one in every 10^6 –10^8 photons undergoes inelastic scattering. However, due to the attachment of modern lasers and microscopes to the Raman spectrometers, very high power densities can be delivered to very small samples, allowing a very efficient detection of the Raman scattered photons. Nonetheless, these powerful improvements in the equipment might also result in undesired degradation and fluorescence of the sample.

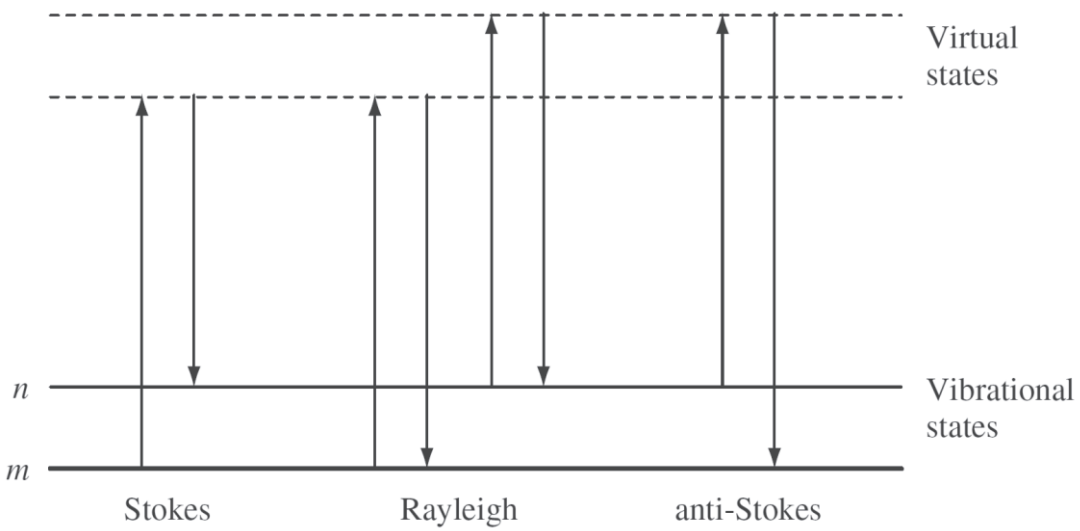

Figure 1.1 Diagram of the Rayleigh and Stokes and anti-Stokes Raman scattering processes. In most cases, *m* represents the ground vibrational state and *n* is the first excited vibrational state. Figure taken from the reference [63].

Figure 1.1 illustrates the different scattering processes that might happen when a single frequency light beam interacts with a molecule. The virtual states presented in Figure 1.1 are determined by the frequency of the light source used, since they are not real states of the molecule, but only virtual states created by the interaction of the laser with the electron that causes polarization of the molecule.

The Raman scattering process from a lower vibrational state *m* causes absorption of energy by the molecule and leads to a promotion to a higher energy excited state, is known as the Stokes Raman scattering. The opposite process is known as anti-Stokes Raman scattering.

At room temperature, some molecules may be present in a vibrational excited state, e.g. in the first excited vibrational state *n* of the Figure 1.1, what justifies the possibility of observation of both Stokes and anti-Stokes bands in a Raman spectrum.

Since the relative intensities of Stokes and anti-Stokes processes depend on the population of the different states of the molecule, the anti-Stokes Raman scattering is usually much weaker than the Stokes scattering process, because the number of molecules expected to be in a higher-energy vibrational state is smaller.[56-60,65–67]

1.5 Differential scanning calorimetry

There are two different types of calorimeters to perform differential scanning calorimetry experiments: power compensation calorimeters and heat flux calorimeters. The calorimeter used throughout this study was a power compensation one (see Section 2.1.7).

The differential scanning calorimetry (DSC) technique measures the differential heat flow between a sample and a reference material, monitoring the thermal response of a sample to temperature changes, or isothermically. The same temperature program is applied to both the sample and reference pans (typically, the later one is an empty pan), and the difference in heat flow to each pan is measured (the sample and the reference pans are maintained at the same temperature throughout the experiment). The sample transitions appear as endothermic peaks if the sample absorbs heat or as exothermic peaks if the sample releases energy. The basic principle of DSC is that when a sample undergoes a physical transformation, such as a crystallization or melting processes, different quantities of heat need to flow to the different pans to maintain the sample and the reference at the same temperature. If it is needed less heat flowing to the sample pan the process is exothermic. On the contrary, if it must flow more heat to the sample pan, the process is endothermic. For example, as a pure liquid sample crystallizes into a solid one, it will be required less heating flowing to the sample pan in order to maintain the temperature at the same rate as the reference, since the crystallization process is exothermic. On the other hand, if the sample undergoes an endothermic process, such as melting or enantiotropic solid-solid transitions, more heat is needed to flow to the sample pan to maintain the temperature rate between the two pans. Thus, differential scanning calorimeters are able to measure the amount of energy that is absorbed or released during these thermodynamic events by observing the difference in heat flow between the sample and the reference pans.[66–69]

The power compensation calorimeters use separate heaters for the sample and the reference pans.[69] The pans are maintained at the same temperature while the electric power used by their heaters is monitored. The substances are investigated in small amount (weighing less than 2.5 mg, in our calorimeter) in order to ensure that heating, cooling or thermal equilibration can be reached as quick as possible. Both pans are located over their respective heaters and the temperatures are monitored using electronic temperature sensors located right beneath the samples. Typically, in power compensated DSC, the temperature is monitored by platinum resistance thermometers, because of the high melting point of the platinum.

1.6 Polarized light thermal microscopy

Polarized light thermal microscopy (PLTM) is the most widely used microscopy technique in characterization of properties of solid state compounds, specifically in investigation of polymorphic forms, and is often used as a complementary technique of DSC.[70–72]

PLTM technique consists in the microscopic direct observation of samples submitted to temperature programs similar to those used in DSC experiments. The main advantage of this technique regarding DSC is that one can visualize the physical transformations that occur in the sample, frequently allowing the detection of some processes with low heat transfer that, for that reason, might be difficult to follow by DSC. It is also possible to study and characterize different transformations that might occur in a heterogeneous sample, as

long as the different analytes are in the observable image of the experiment. However, the temperature and heat flow control is not as accurate as in DSC standard experiments.[73,74]

PLTM uses light that has been modified by a polarizer, allowing obtaining structural information about the sample. The substances can be classified as anisotropic or isotropic, depending on their optical behavior. Anisotropic substances have a refractive index that varies with the direction of the propagation of light along the crystal lattice. On the other hand, isotropic samples have the same refractive index along all directions of light propagation (e.g. amorphous solids and crystalline solids with cubic crystal systems). Therefore, the use of polarized light facilitates the identification of phase transitions and other processes, as vitrification.[71]

Through the use of the microscope, these observed physical transformations can also be recorded and later studied in more detail, for example, slowing up the video in order to observe carefully the process.

1.7 X-ray analysis

X-rays were discovered by W.C. Roentgen in 1985 and since then have been playing an important role in many fields, especially in materials science. The fact that the interatomic distances in a crystalline sample have the same order of magnitude as X-rays wavelength (~0.01 to 10 nm) makes it possible for crystals to diffract an X-ray beam.

Electrons and nuclei, which are charged particles, interact with electromagnetic waves such as X-rays. Since electrons are much lighter than nuclei, their contribution for X-ray scattering is much weaker. The distribution of electron density is probed in an X-ray diffraction (XRD) experiment and, since the crystalline structure is periodic, it is possible to determine the contents of a unit cell from the XRD diffraction pattern.

The diffraction from a crystalline sample can be understood by the Braggs (William and his son Lawrence, both Physical Nobel Prize laureates in 1915) description of the van Laue theory, in which an incident X-ray beam would be reflected by sets of parallel planes (*h*,*k*,*l*) of atoms, uniformly spaced by a distance *d*. The condition for diffraction from such set of planes is known as Bragg Law and can be written as:

$$n\lambda = 2d \sin\theta \tag{1.24}$$

where θ is the angle of incidence of the beam to the planes and n is the order of reflection (n = 1, 2. 3, …, as we get reflections of first, second, third, …, order regarding the same set of planes (*h*,*k*,*l*). Bragg Law affirms that in order to get a constructive interference condition, the path length difference between two incident waves in consecutive planes must be a multiple of the wavelength, λ, as illustrated in Figure 1.2.

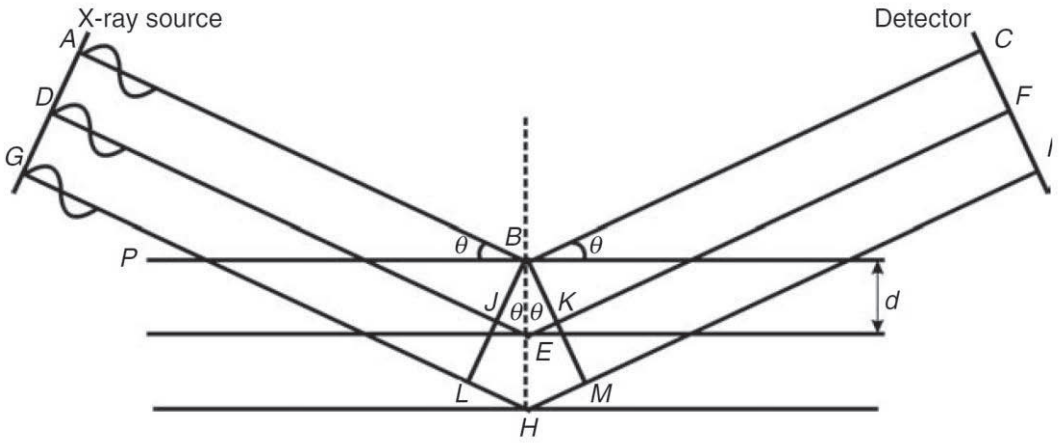

Figure 1.2 illustration of Bragg reflection planes from a set of parallel planes. Figure taken from the reference 75.

The structure factor F_{hkl} represents the scattering amplitude from one unit cell and can be written as

$$F_{hkl} = \sum_i f_i e^{2\pi i(hx_i+ky_i+lz_i)} \tag{1.25}$$

where f_i is the atomic scattering factor for atom i in the unit cell, described by the fractional coordinates x_i, y_i and z_i. I_{hkl} represents the intensity of the diffracted beam and is proportional to the square of the structure factor, as

$$I_{hkl} \propto |F_{hkl}|^2 \tag{1.26}$$

The XDR experiments consist in measuring the scattered intensity as a function of the scattering angle. The last expression is valid for X-ray elastic scattering that is responsible for Bragg reflections. Additionally, inelastic processes may also occur, but since they are incoherent, do not contribute to diffraction.

The unit cell and its contents are the two main crystallographic parameters which essentially define the structure of a diffraction pattern that can be constructed as following: *a)* positions of the Bragg peaks are established from Bragg Law as function of λ and *d*-spacing, with the latter being calculated from the unit cell dimensions; *b)* the intensities are calculated for individual Bragg peaks from the structural model, which includes the atomic coordinates in the unit cell; *c)* the peak shape function is a convolution of the instrumental broadening, wavelength dispersion and intrinsic specimen broadening due to crystalline size and strain, and represents the shape of the Bragg peaks; *d)* the result pattern is the sum of the individual peaks and a background function.[55,75]

1.8 Metal complexation

Inorganic small molecules have a long history in both biology and medicine areas, as ancient civilization used gold and copper for healing purposes. Nowadays, complexation of metal ions with small organic molecules is frequently studied in order to attempt the improvement of their characteristics as pharmaceutical agents. That interest started when arsenic-containing salvarsan was found to be an antisyphilis agent and become the world's first blockbuster drug.[76]

Inorganic compounds have particular features, such as distinctive electronic, chemical and photophysical properties that make them notably useful for a wide range of applications.[77–79]

The most interesting chemical properties of metals that are used in the complexation with small organic molecules are: *a)* metal ions are positively charged in aqueous solution, and that charge can be manipulated on the coordination environment so that a metal can be complexed to cationic, anionic or neutral ligands; *b)* metal ions bind to organic ligands *via* interactions that are often strong and selective. The ligands can impart their own functionalities and can also tune properties of the overall complex that are distinct from those of the isolated different components of the complex; *c)* such complexes span a range of coordination geometries that give them peculiar shapes compared with organic molecules. The geometry properties as bond lengths, bond angles and the number of coordination sites vary depending on the metal ion and on its charge; *d)*: metal ions with high electron affinity can significantly polarize groups that are present in the molecules bonded to them, facilitating some chemical processes, such as hydrolysis reactions, thus behaving as Lewis acids; *e)* the transition metals have a variable number of electrons in the d-shell orbitals and that characteristic confers interesting electronic and magnetic properties to transition metal complexes; *f)* coupled with the variability of the number of electrons in the d-shell is the ability, for a large number of transition metals, to undergo one-electron oxidation or reduction processes.[80,81]

There are already some metal complexes with 1-methylhydantoin known in the literature, namely with gold,[82] platinum,[83] silver[84,85] and nickel,[86] and their crystallographic structures have already been described. In this work, we have started the study of three novel metal complexes with 1-MH. Three different metals were chosen, magnesium (II), iron (II) and copper (I), that have different properties according to the principle of hard and soft acids and bases (HSAB). The HSAB principle essentially states that hard acids prefer to coordinate to hard bases and soft acids prefer to coordinate to soft bases. A soft base is a chemical species where the donor atom or group has high polarizability, low electronegativity, is easily oxidized and has low-lying orbitals. Contrarily, a hard base has a donor atom or group of low polarizability, high electronegativity, is hard to oxidize and has inaccessible empty orbitals of high energy. In a soft acid, the acceptor atom or group has a low positive charge, is large-sized and has various easily excitable outer electrons. On the other hand, in a hard acid species, the acceptor atom or group has a large positive charge, is small-sized and has no easily excitable outer electrons.[87] There are also borderline acids and bases that show intermediate properties between hard and soft acids and bases, respectively.

The 1-MH molecule can bind to a metal complex in two different positions, *via* O7 and O9 carbonyl atoms and *via* the N3 atom. Since these two binding sites in 1-MH have different HSAB properties (the oxygen sites present properties closer to a hard base than the nitrogen site) it is interesting to investigate if the three different metal ions (Mg^{2+} is a hard acid, Fe^{2+} a borderline metal, and Cu^{+} a soft metal)[81] can interact with 1-MH ligand and if so, how they are bound.

Chapter 2
Experimental

Chapter 2

Experimental

2.1 Materials and Methods

2.1.1 1-MH, 5-MH and 5-HAA commercial samples

1-Methylhydantoin, 5-mehtylhydantoin and 5-hydantoin acetic acid were purchased from Sigma-Aldrich (97%, 97% and 98% purity, respectively).

2.1.2 Theoretical methods

All density functional theory (DFT) calculations were carried out using the Gaussian 09 program.[88] The three parameter B3LYP density functional, including the Becke's gradient exchange correction[89] and the Lee, Yang and Parr correlation functional,[90] was used together with the 6-311++G(d,p) basis set.[91] The vibrational spectra of 1-MH, 5-MH and 5-HAA were calculated at the same level of theory. In order to correct for the basis set limitation and anharmonicity effects, the calculated B3LYP/6-311++G(d,p) harmonic vibrational frequencies were scaled by 0.957 above 3400 cm^{-1}, and by 0.980 below 3400 cm^{-1}. The normal coordinate analysis was performed using a locally modified version of BALGA, according to the methodology described by Schachtschneider and Mortimer.[92] The symmetry internal coordinates used in this analysis were defined as recommended by Pulay et al.[93] Natural bond analysis (NBO) was performed according to Weinhold and co-workers, using NBO 3.1, as implemented in Gaussian 09.[94,95]

2.1.3 Argon matrices

The matrices were prepared by co-deposition of 1-MH, 5-MH or 5-HAA and argon (Air Liquide, N60) onto a CsI window, mounted at the cold (10 K) tip of the cryostat (APD Cryogenics closed-cycle helium-cooled refrigerator system with a DE-202A expander). 1-MH, 5-MH and 5-HAA vapors were obtained by *in situ* vacuum sublimation of the compound placed in a thermoelectrically heatable furnace assembled inside the

cryostat. The temperature of the sample holder (CsI window) was measured by a silicon diode temperature sensor, connected to a digital controller (LakeShore Model 331), with an accuracy of 0.1 K.

2.1.4 Matrices irradiation

The 1-MH matrices were irradiated through an outer quartz window of the cryostat with broadband UV light produced by a 500 W Hg(Xe) lamp (Newport, Oriel Instruments) set up to provide an output of 200 W at the sample or narrowband (fwhm 0.2 cm^{-1}) UV light provided by a Spectra Physics MOPO-SL tuned at 230 nm (repetition rate = 10 Hz, pulse energy 10 mJ, duration = 10 ns). The MOPO was pumped by a pulsed Quanta Ray Pro-Series Nd:YAG laser. In the broadband irradiation experiments, the Hg(Xe) lamp was fitted with a water filter (8 cm long) to absorb heat, and appropriate UV-cutoff filters were used to select wavelength range (λ > 367, 328, 295, 234 nm).

2.1.5 Infrared spectra

The infrared spectra were recorded with 0.5 cm^{-1} resolution, using a Thermo Nicolet 6700 Fourier transform infrared (FTIR) spectrometer, equipped with a Ge/KBr beam splitter and a deuterated triglycine sulfate (DTGS) detector. To avoid interferences from H_2O and CO_2, a flux of air free of water vapor and carbon dioxide continuously purged the optical path of the spectrometer. ATR infrared spectra were collected with 1 cm^{-1} spectral resolution in a Thermo Nicolet IR300 FTIR spectrometer, equipped with a Smart Orbit ATR accessory, a DTGS detector and a Ge/KBr beam splitter.

2.1.6 Raman spectra

Macro Raman spectra were collected using a Thermo Scientific DXR SmartRaman Spectrometer, with 780 nm laser exictation. Single crystal Raman spectra were obtained, in the wavenumber range 200-4000 cm^{-1}, using a Raman micro-system (Horiba LabRam HR Evolution, equipped with a Synapse CCD detector, a high-stability BXFM open space confocal microscope, and a 600 gr mm^{-1} grating), with 633 nm HeNe laser excitation. The laser power at the sample was approximately 17 mW, and the exposure time between 10 and 100 s. A 100x objective lens was used, giving a laser spot diameter of 0.8 μm at the sample. Individual spectra were obtained with 1.5 cm^{-1} resolution. The final spectra were the mean of 50 scans for every sample.

In the temperature variation Raman studies, the sample was placed in a hot stage (THMS 600, Linkam Scientific Instruments Ltd. Surrey, UK), and the spectra obtained with the spectrometer and irradiation source conditions described above. The hot stage temperature was controlled by a T95-PE Linkpad controlling unit. The heating rate was set up at 10 °C min^{-1}. At each selected temperature, the Raman spectrum, in the 1000-1850 cm^{-1} range, was recorded with a 30 s acquisition time and 2 accumulations.

2.1.7 Differential scanning calorimetry

Differential scanning calorimetry (DSC) measurements were done using a Pyris-1 power compensation calorimeter from Perkin-Elmer, with an intra-cooler cooling unit at a –25 ºC (ethylene glycol-water, 1:1 v/v, cooling mixture) under a 20 mL min^{-1} nitrogen purge flow. Samples (0.8-2.5 mg) were hermetically sealed in aluminum pans, with an empty pan used as reference. Temperature and enthalpy calibrations were performed with indium (Perkin-Elmer, x= 99.99%, T_{fus} = 156.60 ºC) and byphenyl (CRM LGC, T_{fus} = 68.93ºC ± 0.03 ºC).[96] In the DSC experiments, the samples were scanned from 25 to 162 ºC for 1-MH experiments, from 25 to 155 ºC for 5-MH experiments and from 25 to 222 ºC for 5-HAA experiments, at a scan rate β = 10 ºC min^{-1}.

2.1.8 Polarized light thermal microscopy

Polarized light thermal microscopy (PLTM) was used to obtain images of the compound within the same range of temperature used in DSC experiments. A hot stage Linkam system (model DSC600) was used, with a Leica DMRB microscope and a Sony CCD-IRIS/RGB video camera. The image analysis was performed using the Real Time Video Measurement System software from Linkam. The images were obtained by combined use of polarized light and wave compensators, using a 200x magnification.

2.1.9 X-ray crystallography

The single crystal X-ray measurements were carried out using a Bruker APEX II diffractometer, at 293(2) K, using graphite monochromated MoK_α (λ = 0.71073 Å) excitation. Absorption corrections were made using SADABS.[97] Refinements were carried out with the SHELXL-2014/7 package.[98] All refinements were made by full-matrix least-squares on F^2 with anisotropic displacement parameters for all non-hydrogen atoms. All

hydrogen atoms could be located by difference Fourier synthesis; their positions were refined as riding on parent atoms with an isotropic temperature factor using SHELXL-2014/7 defaults.[98]

2.1.10 Recrystallization of 1-MH, 5-MH and 5-HAA

1-MH, 5-MH and 5-HAA ~35 mg samples were recrystallized using different solvents. Solutions of dichloromethane, 1,4-dioxane, tetrahydrofuran (THF), acetone, water, methanol and ethanol (with volumes of 4 to 20 cm^3) were prepared and allowed to evaporate at room temperature.

2.1.11 Preparation of 1-MH coordination complexes

The 1-MH coordination complexes were prepared as follows: 0.15 mM of $MgCl_2 \cdot 6H_2O$, $FeCl_2 \cdot 4H_2O$ or CuCl dissolved in 10 cm^3 of water were added to 0.3 mM of 1-MH also dissolved in 10 cm^3 of water. Finally, to adjust pH to ~8.0, 1 cm^3 of 0.05 M KOH aqueous solution were added. The obtained solutions were allowed to evaporate at room temperature and the products were then filtered off.

Chapter 3

Results and Discussion

Chapter 3

Results and Discussion

3.1 Structure of 1-MH, 5-MH and 5-HAA molecules

The calculated geometrical parameters for ground state minimum energy conformation of 1-MH, 5-MH and 5-HAA are presented in Tables 3.1, 3.2 and 3.3, respectively.

Table 3.1. Optimized geometry of 1-methylhydantoin calculated at the B3LYP/6-311++G(d,p) level of theory

Bond length		*Angle*	
N1-C2	1.369	N3-C4=O9	127.7
N1-C5	1.451	C5-C4=O9	127.3
N1-C6	1.448	N1-C5-C4	103.3
C2-N3	1.414	N1-C5-H10,11	112.7
C2=O7	1.210	C4-C5-H10,11	109.8
N3-C4	1.376	H10-C5-H11	108.4
N3-H8	1.009	N1-C6-H12,14	111.0
C4-C5	1.531	N1-C6-H13	108.0
C4=O9	1.207	H13-C6-H12,14	109.0
C5-H10,11	1.096	H12-C6-H14	108.9
C6-H12,14	1.095		
C6-H13	1.089	*Dihedral Angle*	
		C2-N1-C5-H10	118.5
Angle		C2-N1-C5-H11	-118.5
C2-N1-C5	112.3	C6-N1-C5-H10	-61.5
C2-N1-C6	123.5	C6-N1-C5-H11	61.5
C5-N1-C6	124.3	C2-N1-C6-H12	-119.4
N1-C2-N3	105.9	C2-N1-C6-H14	119.4
N1-C2=O7	128.6	C5-N1-C6-H12	60.6
N3-C2=O7	125.5	C5-N1-C6-H14	-60.6
C2-N3-C4	113.5	N3-C4-C5-H10	-120.5
C2-N3-H8	122.0	N3-C4-C5-H11	120.5
C4-N3-H8	124.5	O9=C4-C5-H10	59.53
N3-C4-C5	105.0	O9=C4-C5-H11	-59.53

[a] Bond lengths in Å, angles in degrees. See atom numbering in Scheme 3.1.

According to the performed calculations, the 1-MH molecule has C_s symmetry, with a planar ring and the methyl substituent oriented so that the hydrogen atom located in the ring plane points toward O7 (see Scheme 3.1), and the 5-MH and 5-HAA molecules have C_1 symmetry (see Scheme 3.1) with a quasi-planar ring. The orientation of the methyl group in 1-MH ensures stabilization of the molecule through an

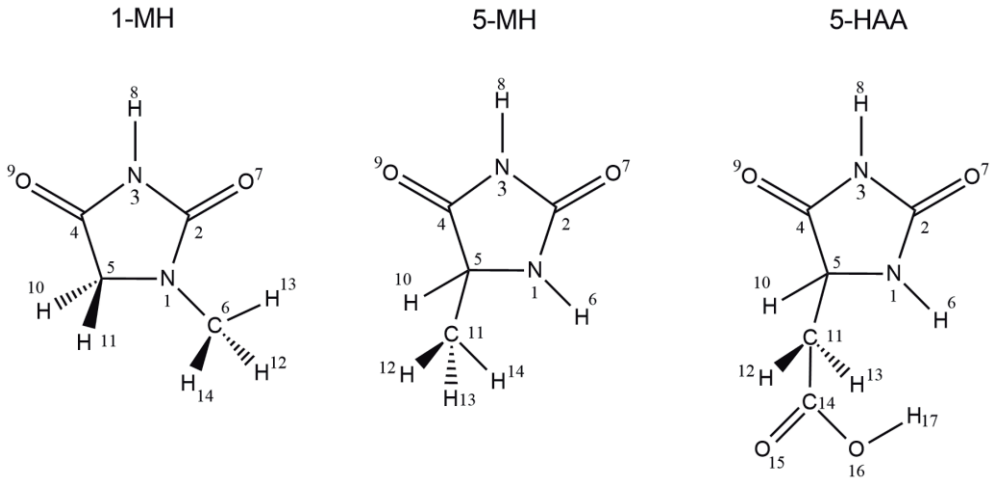

Scheme 3.1 1-MH, 5-MH and 5-HAA molecules, with atom numbering

intramolecular electrostatic interaction resulting from the nearly antiparallel alignment of the dipoles of the C6–H13 and C2=O7 bonds. The most interesting results regarding the geometry of 1-MH, 5-MH and 5-HAA are the following: (i) for 1-MH and 5-MH, the bond length of the carbonyl group C2=O7 (1.210 and 1.208 Å, respectively), which is bonded to two nitrogen atoms, is longer than that of the carbonyl group C4=O9 (1.207 Å), that is connected to a single nitrogen atom, in consonance with the expected larger total π electron delocalization from the nitrogen atoms to O7, compared to O9. For 5-HAA, the length of both carbonyl groups is the same, because the larger π delocalization from the nitrogen atoms to O7 is compensated by the σ electronic system effects due to the presence of the electro attractor acetic acid substituent, onto the C4=O9 bond; (ii) the ring C_{sp2}–N bond lengths follow the order C2–N3 > C4–N3 > C2–N1 (1.414, 1.376, 1.369 Å, respectively, for 1-MH; 1.412, 1.378, 1.369 Å, for 5-MH; and 1.410, 1.377, 1.376 Å, for 5-HAA), pointing out to a maximum N-to-O electron delocalization in the fragment N1–C2=O7, i.e., when the nitrogen atom has only one oxygen atom as acceptor, while the minimum N-to-O electron donation occurs in the N3–C2=O7 fragment because the N3 atom has to donate electronic charge to both O7 and O9 and, since O7 has another donor (N1), N3 donates electronic charge preferentially to O9; (iii) the two C_{sp3}–N bond lengths in 1-MH (exocyclic C6–N1 and ring C5-N1) do not differ very much (1.448 and 1.451 Å, respectively), and the C4–C5 bond length in 1-MH (1.531 Å) is relatively longer than the typical C_{sp3}–C_{sp2} length (~1.50 Å)[99], indicating that in the C4–C5–N1–C6 fragment the electron delocalization is minimal. In both 5-MH and 5-HAA, the C4–C5 bond length (1.539 Å) is longer than in 1-MH, indicating that the substituent bonded to C5 atom reduces even more the π delocalization in the C4–C5–N1–H6 fragment (the N1–C5 bond length is also longer in these molecules than in 1-MH); (iv) the internal angles of the ring with a nitrogen atom in the apex (C4–N3–C2 and C5–N1–C2) are much larger (112–114º in 1-MH and around 113º in 5-MH and in 5-HAA) than those with carbon atoms in the apex (N1–C2–C3, N1–C5–C4 and N3–C4–C5; ~103-106º in 1-MH, ~101-106º in 5-MH and ~102-106º in 5-HAA), suggesting relatively different *s–p* composition of the hybrid orbitals of the N and C atoms used to make the ring bonds (we will

Table 3.2. Optimized geometry of 5-methylhydantoin calculated at the B3LYP/6-311++G(d,p) level of theory

Bond length		*Dihedral Angle*	
N1-C2	1.369	C5-N1-C2-N3	-4.2
N1-C5	1.459	C5-N1-C2-N7	176.1
N1-H6	1.007	H6-N1-C2-N3	-171.0
C2-N3	1.412	H6-N1-C2-N7	9.4
C2=O7	1.208	C2-N1-C5-C4	4.6
N3-C4	1.377	C2-N1-C5-H10	-109.0
N3-H8	1.010	C2-N1-C5-C11	126.1
C4-C5	1.539	H6-N1-C5-C4	170.6
C4=O9	1.207	H6-N1-C5-H10	57.0
C5-H10	1.097	H6-N1-C5-C11	-67.9
C5-C11	1.528	N1-C5-C11-H12	65.9
C11-H12	1.093	N1-C5-C11-H13	-174.5
C11-H13,14	1.092	N1-C5-C11-H14	-54.5
		C4-C5-C11-H12	-178.8
Angle		C4-C5-C11-H13	-59.2
C2-N1-C5	113.6	C4-C5-C11-H14	60.8
C2-N1-H6	120.1	N1-C2-N3-C4	2.0
C5-N1-H6	124.8	N1-C2-N3-H8	-177.1
N1-C2-N3	105.3	O7=C2-N3-C4	-178.3
N1-C2=O7	128.9	O7=C2-N3-H8	2.6
N3-C2=O7	125.8	C2-N3-C4-C5	0.8
C2-N3-C4	113.5	C2-N3-C4=O9	-179.1
C2-N3-H8	122.1	H8-N3-C4-C5	179.9
C4-N3-H8	124.4	H8-N3-C4=O9	0.0
N3-C4-C5	105.9	N3-C4-C5-N1	-3.1
N3-C4=O9	127.4	N3-C4-C5-H10	113.3
C5-C4=O9	126.8	N3-C4-C5-C11	-126.0
N1-C5-C4	101.6	O9=C4-C5-N1	176.8
N1-C5-H10	110.9	O9=C4-C5-H10	-66.8
N1-C5-C11	114.5	O9=C4-C5-C11	53.9
C4-C5-H10	107.1	H10-C5-C11-H12	-59.7
C4-C5-C11	112.5	H10-C5-C11-H13	59.9
H10-C5-C11	109.8	H10-C5-C11-H14	179.9
C5-C11-H12	110.6		
C5-C11-H13	109.6		
C5-C11-H14	110.7		
H12-C11-H13	108.5		
H12-C11-H14	108.6		
H13-C11-H14	108.8		

[a] Bond lengths in Å, angles in degrees. See atom numbering in Scheme 3.1.

return to this point later; (v) one of the most interesting conclusions that we can extract results from the comparison of the geometrical features of 1-MH, 5-MH and 5-HAA with the parent hydantoin molecule:[16] the geometry of 1-MH is very similar to that of the hydantoin, indicating that the electronic effects due to the methyl substituent at N1 are not much relevant. In turn, the overall geometry of 5-MH is also similar to that

Table 3.3. Optimized geometry of 5-hydantoin acetic acid calculated at the B3LYP/6-311++G(d,p) level of theory

Bond length		*Angle*	
N1-C2	1.376	C14-O16-H17	107.4
N1-C5	1.458		
N1-H6	1.009	*Dihedral Angle*	
C2-N3	1.410	C5-N1-C2-N3	-8.1
C2=O7	1.206	C5-N1-C2-N7	172.4
N3-C4	1.377	H6-N1-C2-N3	-162.0
N3-H8	1.010	H6-N1-C2-N7	18.5
C4-C5	1.539	C2-N1-C5-C4	9.6
C4=O9	1.206	C2-N1-C5-H10	-105.6
C5-H10	1.096	C2-N1-C5-C11	130.3
C5-C11	1.534	H6-N1-C5-C4	162.1
C11-H12	1.095	H6-N1-C5-H10	46.9
C11-H13	1.090	H6-N1-C5-C11	-77.1
C11-C14	1.516	N1-C2-N3-C4	2.9
C14=O15	1.205	N1-C2-N3-H8	-173.8
C14-O16	1.349	O7=C2-N3-C4	-177.6
O16-H17	0.970	O7=C2-N3-H8	5.8
		C2-N3-C4-C5	2.9
Angle		C2-N3-C4=O9	-176.0
C2-N1-C5	112.8	H8-N3-C4-C5	179.5
C2-N1-H6	118.3	H8-N3-C4=O9	0.5
C5-N1-H6	123.0	N3-C4-C5-N1	-7.2
N1-C2-N3	105.5	N3-C4-C5-H10	110.8
N1-C2=O7	128.5	N3-C4-C5-C11	-129.3
N3-C2=O7	126.0	O9=C4-C5-N1	171.8
C2-N3-C4	113.4	O9=C4-C5-H10	-70.2
C2-N3-H8	122.2	O9=C4-C5-C11	49.7
C4-N3-H8	124.3	N1-C5-C11-H12	47.2
N3-C4-C5	105.6	N1-C5-C11-H13	-71.2
N3-C4=O9	127.5	N1-C5-C11-C14	164.4
C5-C4=O9	126.8	C4-C5-C11-H12	162.1
N1-C5-C4	101.8	C4-C5-C11-H13	43.8
N1-C5-H10	111.9	C4-C5-C11-C14	-80.7
N1-C5-C11	114.0	H10-C5-C11-H12	-78.5
C4-C5-H10	108.1	H10-C5-C11-H13	163.2
C4-C5-C11	112.0	H10-C5-C11-C14	38.7
H10-C5-C11	108.9	C5-C11-C14=O15	-36.8
C5-C11-H12	108.8	C5-C11-C14-O16	145.7
C5-C11-H13,14	111.7	H12-C11-C14=O15	81.8
H12-C11-H13	107.3	H12-C11-C14-O16	-95.6
H12-C11-C14	106.4	H13-C11-C14=O15	-161.9
H13-C11-C14	110.6	H13-C11-C14-O16	20.6
C11-C14=O15	124.8	C11-C14-O16-H17	178.7
C11-C14-O16	111.8	O15=C14-O16-H17	1.2
O15=C14-O16	123.4		

[a] Bond lengths in Å, angles in degrees. See atom numbering in Scheme 3.1.

of parent hydantoin, except the geometrical features directly related to the C5 atom, where the methyl substituent is bonded [the bond lengths of the N1-C5, C4-C5 and C5-H10 bonds are longer in 5-MH than in hydantoin (1.459, 1.539 and 1.097 Å *vs.* 1.451, 1.534 and 1.094 Å), the C5-N1-H6 angle increases (124.8º in 5-MH *vs.* 123.8º in hydantoin), and the angles where C5 is the apex, N1-C5-H6, N1-C5-H10 and C4-C5-H10 reduce (angle values in 5-MH are 101.6, 110.9 and 107.1º, respectively, *vs.* 102.4, 113,3 and 109.4º in hydantoin)]; the presence of the methyl substituent in C5 atom also changes the C_s symmetry of hydantoin to C_1 symmetry in 5-MH.

Finally, while the geometry of 5-HAA have some parallelism with that of the parent hydantoin, it exhibits some differences in certain features, namely in those corresponding to the C4-C5(H10)-N1-H6 fragment, because of the presence of the substituent [for example, the N1-C2, the N1-C5 and the C4-C5 bond lengths are longer in 5-HAA (1.376, 1.458 and 1.539 Å) than in hydantoin (1.370, 1.451 and 1.534 Å, respectively), and the C2-N1-H6 and C5-N1-H6 angles are smaller (118.3º and 123.0º, compared to 120.8º and 125.8º in parent hydantoin)].

The major difference between 5-HAA and 5-MH is the reduction of the C2-N1-H6 and C5-N1-H6 angles, and also of the N1-C5-H-10 and C4-C5-H10 angles in the first molecule. These differences can be essentially explained as resulting of the electron attractor characteristics and bigger size of the substituent in 5-HAA, as the C5-C11 bond length increases 0.6 Å in this molecule compared to 5-MH, while the N1-C5-H11 angle is larger and the N1-C2 bond length increases (by 0.7 Å).

As described in detail in the next section, most of the noted characteristic geometrical attributes of the 1-MH, 5-MH and 5-HAA molecules can be correlated with their electronic features.

3.2 Natural Bond Orbital Analyses of 1-MH, 5-MH and 5-HAA

The analyses of the charge distribution in the molecules of 1-MH, 5-MH and 5-HAA allowed to further our understanding on their fundamental structural features, and to extract some relevant conclusions regarding their chemical reactivity.

The performed NBO analysis was particularly successful to get across the specific characteristics of the σ and π electronic systems of the molecules.

The total NBO atomic charges, as well as their σ and π partition, are presented in Tables 3.4, 3.5 and 3.6, for 1-MH, 5-MH and 5-HAA, respectively. As shown in the tables, the total charges of both nitrogen atoms are negative, as we could expect, because the nitrogen atoms are more electronegative than the carbon atoms to which they are bonded. Analogously, the C2 and C4 carbon atoms (and also the C14 carbon atom in 5-HAA),

Table 3.4. Natural bond orbital (NBO) atomic charges (in units of electron; e = 1.60217646 x 10^{-19} C) for 1-MH, obtained from the DFT(B3LYP)/6-3111++G(d,p) calculations[a]

	NBO charge		
atom	total	σ	π
N1	-0.516	-0.805	0.289
C2	0.819	0.645	0.174
N3	-0.654	-0.991	0.336
C4	0.683	0.466	0.216
C5	-0.247	-0.030	-0.217
C6	-0.355	-0.156	-0.199
O7	-0.621	-0.091	-0.530
H8	0.421		
O9	-0.578	-0.121	-0.457
H10	0.218		
H11	0.218		
H12	0.190		
H13	0.233		
H14	0.190		

[a] See Scheme 3.1 for atom numbering.

which are connected to more electronegative oxygen and nitrogen atoms, have positive total charges, while C5 (and C6 in 1-MH, or C11 in 5-MH and 5-HAA) are bonded to hydrogen atoms and, therefore, have negative total charges. In 1-MH, as C6 is connected to 3 hydrogen atoms, this carbon atom is more negative than C5, which is bonded only to two hydrogen atoms. The same happens in 5-MH and in 5-HAA, with C11 being more negative than C5. The oxygen atoms O7 and O9 (and also O15 and O16 in 5-HAA molecule) are the most electronegative atoms in the molecules and present total charges that are considerably negative (between -0.677 and -0.572 e).

The total NBO charges do not provide more than a very general (and simplified) picture of the electronic structure of the molecules. Here we present the NBO charges partition in terms of σ and π systems. This analysis brings to light some considerably more interesting details of the electron distribution in the molecules. From this analysis, it could be noticed that, although the nitrogen atoms have a negative total charge, they present a positive π charge, in agreement with the mesomeric structures II, III and IV illustrated in Scheme 3.2. It should also be noted that the N3 nitrogen atom has a π charge that is more positive than N1, in agreement with the fact that N3 shows a positive charge in mesomeric structures III and IV (see Scheme 3.2), while N1 only shows a positive charge in mesomeric structure II. A similar reasoning can be applied to understand the relative values of the π charges of the two oxygen atoms connected to the ring.

Table 3.5. Natural bond orbital (NBO) atomic charges (in units of electron; e = 1.60217646 x 10^{-19} C) for 5-MH, obtained from the DFT(B3LYP)/6-3111++G(d,p) calculations[a]

	NBO charge		
atom	total	σ	π
N1	-0.661	-0.948	0.287
C2	0.809	0.637	0.172
N3	-0.656	-1.010	0.354
C4	0.689	0.484	0.205
C5	-0.095	0.082	-0.176
H6	0.408	-	-
O7	-0.610	-0.078	-0.532
H8	0.421	-	-
O9	-0.581	-0.098	-0.483
H10	0.214	-	-
C11	-0.578	-0.417	-0.160
H12	0.205	-	-
H13	0.225	-	-
H14	0.210	-	-

[a] See Scheme 3.1 for atom numbering.

Scheme 3.2 (I) Dominant Canonic Forms of 1-Methylhydantoin (1-MH), 5-Methylhydantoin (5-MH) and 5-Hydantoin Acetic Acid (5-HAA); (II, III and IV) Mesomeric Structures Assuming Delocalization of π Electrons in the NCO Moieties of the Molecule

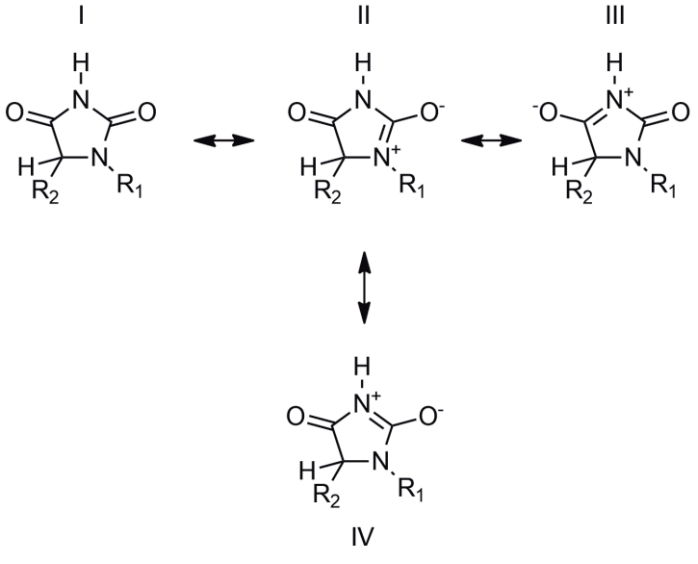

Table 3.6. Natural bond orbital (NBO) atomic charges (in units of electron; e = 1.60217646 x 10^{-19} C) for 5-HAA, obtained from the DFT(B3LYP)/6-3111++G(d,p) calculations[a]

	NBO charge		
atom	total	σ	π
N1	-0.660	-0.942	0.282
C2	0.810	0.635	0.176
N3	-0.654	-1.005	0.351
C4	0.690	0.483	0.207
C5	-0.099	0.084	-0.183
H6	0.408	-	-
O7	-0.602	-0.080	-0.522
H8	0.422	-	-
O9	-0.572	-0.102	-0.470
H10	0.241	-	-
C11	-0.481	-0.307	-0.174
H12	0.239	-	-
H13	0.236	-	-
C14	0.811	0.589	0.222
O15	-0.598	0.001	-0.599
O16	-0.677	0.051	-0.728
H17	0.487		

[a] See Scheme 3.1 for atom numbering.

Since O7 shows a negative charge in two mesomeric structures (II and IV) and O9 is negatively charged only in mesomeric structure III, the O7 atom has a more negative π charge than O9.

Another remarkable feature concerns the σ charges of the two oxygen atoms, since they are considerably less negative than the corresponding π charges and have opposite relative values (the O9 σ charge is more negative than the O7 σ charge; see Tables 3.4, 3.5 and 3.6). This shows that, in comparison with C4=O9, the more extended C2=O7 π bond polarization toward the oxygen atom leads to reduce the trend for the associated σ bond to be polarized in the same direction. The O7 atom is, nevertheless, more negatively charged than O9, in result of its highly polarized π bond through mesomerism. Indeed, these results are in full agreement with the structural results (in particular with the relative C2=O7 and C4=O9 bond lengths in both 1-MH and 5-MH) discussed in Section 3.1, which indicated a larger π electron delocalization from the nitrogen atoms to O7, compared to O9. The special case of 5-HAA have already been discussed in Section 3.1.

The relative values of the π charges in the nitrogen atoms are also in agreement with the relative values of the ring C_{sp2}–N bond lengths that, as discussed in the previous section, point to a maximum N-to-O electron delocalization in the N1–C2=O7 fragment. In fact, the positive π charge of the N1 atom (+0.289, +0.287 and +0.282 e, in 1-MH, 5-MH and 5-HAA, respectively), resulting essentially from the π delocalization to O7 (as presented in Scheme 3.2), is considerably larger than half of the positive charge of the atom N3 (+0.168, +0.177 and 0.176 e, in 1-MH, 5-MH and 5-HAA, respectively), which donates π electron charge to both O7 and O9 oxygen atoms.

The relative relevance of the mesomerism within the different NCO fragments of the 1-MH, 5-MH and 5-HAA molecules, as well as other important intramolecular interactions, can also be evaluated by considering the most relevant NBO interactions. Those interactions are presented in Tables 3.7, 3.8 and 3.9.

Orbital interaction energies, $-E(2)$, between filled and empty NBOs, including non-Lewis extra valence Rydberg orbitals, are obtained from the second-order perturbation approach:

$$E(2) = \Delta E_{ij} = q_i \frac{F_{ij}^2}{\varepsilon_j - \varepsilon_i} \tag{3.1}$$

where F_{ij}^2 is the Fock matrix element between *i* and *j* NBO orbitals, ε_j and ε_i are the energies of the acceptor and donor NBOs, and q_i is the occupancy of the donor orbital.

As it is presented in Tables 3.7, 3.8 and 3.9, the most relevant NBO interactions (designated A, B and C in all tables) involve electronic charge transfer from the nitrogen atoms to the carbonyl bonds, and can be directly related with the mesomeric structures II, III and IV in Scheme 3.2, respectively.

In the case of N1, the electronic charge transfer is exclusive to the π^*(C2=O7) anti-bonding orbital, whereas N3 donates electronic charge to both π^*(C2=O7) and π^*(C4=O9) anti-bonding orbitals. As we could expect, due to the competition between these two interactions involving the N3 atom, the $-E(2)$ relative interaction energies for LP(N3) → π^*(C2=O7) (47.23 and 47.70 kJ mol^{-1} for 1-MH and. 5-MH respectively) and LP(N3) → π^*(C4=O9) (55.70 and 54.65 kJ mol^{-1} for 1-MH and 5-MH respectively) orbital interactions are smaller than that corresponding to the LP(N1) → π^*(C2=O7) (64.23 and 57.88 kJ mol^{-1} for 1-MH and 5-MH respectively) orbital interaction. This phenomenon does not happen in the case of 5-HAA molecule, where the orbital interaction between LP(N3) → π^*(C4=O9) (53.89 kJ mol^{-1}) has the higher $-E(2)$ interaction energy. The presence of the electron attractor carboxylic acid substituent close to C4=O9 may justify this observation. On the other hand, because the π^*(C2=O7) anti-bonding orbital receives electronic charge from both nitrogen atoms, the LP(N3) → π^*(C2=O7) interaction energy in 5-HAA is the smallest among the LP(N) → π^*(C=O) orbital interactions (see Table 3.9). Nevertheless, as a whole, the electronic charge transferred from N1 and N3 atoms to π^*(C2=O7) anti-bonding orbital is considerably higher than the one that results from the single interaction associated with the π^*(C4=O9) anti-bonding orbital, even in 5-HAA (compare the total interaction values of A + B with C in Tables 3.7, 3.8 and 3.9). This is a result that is consistent with the more negative π charge on O7 (-0.530, -0.532, -0.522 *e* in 1-MH, 5-MH and 5-HAA respectively) compared to O9 (-0.457, -0.483, -0.470 *e* in 1-MH, 5-MH and 5-HAA respectively). All these values are truly consistent with the conclusions that were extracted from the structural data presented in Section 3.1, in particular the relative lengths of the different C=O and C_{sp2}–N bonds (C2=O7 ≥ C4=O9; C2–N1 < C4–N3 < C2–N3).

Table 3.7. Stabilization energies for selected NBO pairs as given by second order perturbation theory analysis of the Fock matrix in the NBO basis for 1-MH obtained from the B3LYP/6-311++G(d,p) calculations

Pair name	Donor NBO	Acceptor NBO	–E(2) Energy (kcal mol^{-1})
A	LP (N1)	π* (C2 – O7)	64.23
B	LP (N3)	π* (C2 – O7)	47.23
C	LP (N3)	π* (C4 – O9)	55.70
D	LP2 (07)	σ* (N1 – C2)	24.58
E	LP2 (07)	σ* (C2 – N3)	28.43
F	LP2 (09)	σ* (N3 – C4)	27.05
G	LP2 (09)	σ* (C4 – C5)	22.11
H	LP1 (07)	RY* (C2)	18.01
I	LP1 (09)	RY* (C4)	17.89

[a]See atom numbering in Scheme 3.1. LP, lone electron pair orbital. Ry, Rydberg type orbital.

The other main NBO interactions (D-I in Tables 3.7 and 3.8, and D-M in Table 3.9) are correlated with other types of intramolecular interactions:

(a) The NBO orbital interactions named as D, E, F and G occur between the non-bonded electron pair (LP2; *σ*) of O7 and O9 oxygen atoms and the anti-bonding *σ** orbitals of the neighbor C–N bonds. This type of interaction represent the well-known electron back donation effect involving carbonyl oxygen atoms[100–102] that explains, for example, the unusually long C–H bond length in aldehydes and derivatives of formic acid, and that reflects also in the uncommonly low *ν*(C–H) stretching vibrational frequency in these types of molecules. In 1-MH, these interactions also contribute to determine the relative lengths of the C2–N3, C4–N3 and C2–N1 bonds (1.414, 1.376 and 1.369 Å respectively): the stronger the back-donation from the donor carbonyl lone pair to the acceptor anti-bonding orbital of a given C_{sp2}–N ring-bond, the longer the bond. The same happens in 5-MH where the bond lengths of the C2–N3, C4–N3 and C2–N1 bonds are 1.412, 1.378 and 1.369 Å, respectively, as well as in 5-HAA, where these bond lengths are 1.410, 1.377 and 1.376 Å.

(b) The NBO orbital interactions designated H and I describe the electronic charge transfer from the second non-bonded electron pair (LP1; *σ*) of the oxygen atoms O7 and O9 to one Rydberg orbital of the corresponding carbonyl carbon atom. These interactions are associated with effects related to the carbonyl bond polarization, working specifically as moderators of the *σ* polarization of the carbonyl bonds to compensate the effects of the increased *π* polarization due to the interactions A, B and C.

(c) The NBO orbital interactions named as J, K and L in Table 3.9 represent the electronic charge transfer between the non-bonded electron pair (LP2; *σ*) of oxygen atoms O15 (J and K) or O16 (L) to the anti-bonding *σ** (J and K) or *π** (L) orbitals of the neighbor C–C (J), C–O (K) and C=O (L) bonds. Interactions K and L are considerably more negative than J, as expected considering the electron

Table 3.8. Stabilization energies for selected NBO pairs as given by second order perturbation theory analysis of the Fock matrix in the NBO basis for 5-MH obtained from the B3LYP/6-311++G(d,p) calculations

Pair name	Donor NBO	Acceptor NBO	–E(2) Energy (kcal mol^{-1})
A	LP (N1)	π* (C2 – O7)	57.88
B	LP (N3)	π* (C2 – O7)	47.70
C	LP (N3)	π* (C4 – O9)	54.65
D	LP2 (07)	σ* (N1 – C2)	24.74
E	LP2 (07)	σ* (C2 – N3)	28.49
F	LP2 (09)	σ* (N3 – C4)	27.36
G	LP2 (09)	σ* (C4 – C5)	21.76
H	LP1 (07)	RY* (C2)	18.57
I	LP1 (09)	RY* (C4)	18.21

[a]See atom numbering in Scheme 3.1. LP, lone electron pair orbital. Ry, Rydberg type orbital.

Table 3.9. Stabilization energies for selected NBO pairs as given by second order perturbation theory analysis of the Fock matrix in the NBO basis for 5-HAA obtained from the B3LYP/6-311++G(d,p) calculations

Pair name	Donor NBO	Acceptor NBO	–E(2) Energy (kcal mol^{-1})
A	LP (N1)	π* (C2 – O7)	50.78
B	LP (N3)	π* (C2 – O7)	47.58
C	LP (N3)	π* (C4 – O9)	53.89
D	LP2 (07)	σ* (N1 – C2)	25.24
E	LP2 (07)	σ* (C2 – N3)	28.40
F	LP2 (09)	σ* (N3 – C4)	27.65
G	LP2 (09)	σ* (C4 – C5)	21.95
H	LP1 (07)	RY* (C2)	18.55
I	LP1 (09)	RY* (C4)	18.25
J	LP2 (015)	σ* (C11 – C14)	18.57
K	LP2 (015)	σ* (C14 – O16)	32.92
L	LP2 (016)	π* (C14 – O15)	43.16
M	LP1 (015)	RY* (C14)	17.49

[a]See atom numbering in Scheme 3.1. LP, lone electron pair orbital. Ry, Rydberg type orbital.

delocalization within the O=C–O fragment should be more extended than from the carbonyl moiety to the adjacent C–C bond.

(d) The NBO orbital interaction M in Table 3.9 occurs between the second electron pair (LP1; *σ*) of O15 oxygen atom and one Rydberg type orbital of the corresponding carbonyl carbon atom, expressing the polarization of the C14=O15 bond in an identical way as interactions H and I do in relation to the C2=O7 and C4=O9 bonds.

The analysis of the *s-p* composition of the hybrid NBO's of the ring carbon and nitrogen atoms (Tables 3.4, 3.5 and 3.6) allows us to explain why the internal angles of the ring are considerably larger when we have a

nitrogen atom in the angle apex (C4–N3–C2 and C2–N1–C5) than when it is the carbon in the angle apex (N1–C2–N3, N3–C4–C5 and N1–C5-C4). As mentioned in the previous section, this observation suggests different *s-p* composition of the hybrid orbitals of the C and N atoms that are presented in the ring bonds. A smaller *p* contribution to the hybrid orbital correlates with larger angles,[103,104] so that the average *p* contribution to the hybrid orbitals used to establish the ring bonding NBO's by the nitrogen atoms N1 and N3 is smaller than the used by the carbon atoms C2, C4 and C5.

3.3 IR Spectra of Matrix-Isolated 1-MH, 5-MH and 5-HAA

The matrix isolation spectra of 1-MH, 5-MH and 5-HAA in argon matrix (at 10 K) are presented, together with the B3LYP/6-311++G(d,p) calculated spectra of the compounds, in Figures 3.1, 3.2 and 3.3. The proposed band assignments, based on the calculated potential energy distributions (PED) resulting from the performed normal coordinates analysis, are provided in Tables 3.11, 3.13 and 3.15. Tables 3.10, 3.12 and 3.14 provide the definitions of the internal symmetry coordinates used in the PED analysis.

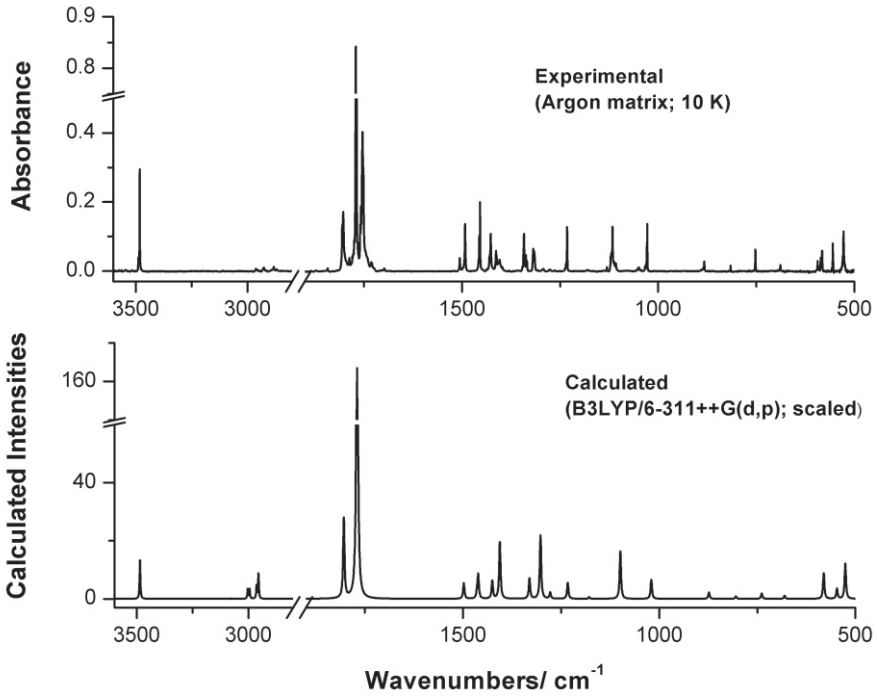

Figure 3.1 – Experimental infrared spectrum of monomeric 1-MH isolated in an argon matrix at 10 K (*top*) and simulated spectrum of 1-MH monomer using Lorentzian functions centered at the scaled B3LYP/6-311++G(d,p) calculated wavenumbers (*bottom*). Note that the calculated intensities correspond, in the simulated spectrum, to the areas below the Lorentzian functions, not to peak intensities.

Table 3.10 Internal coordinates used in the normal modes analysis of 1-MH

Coordinate	Definition [b]	Approximate description [c]
S_1	$r_{1,6}$	ν(NC)
S_2	$r_{3,8}$	ν(NH)
S_3	$r_{5,10} - r_{5,11}$	$\nu(CH_2)_{as}$
S_4	$r_{5,10} + r_{5,11}$	$\nu(CH_2)_s$
S_5	$r_{2,7} + r_{4,9}$	$\nu(C{=}O)_s$
S_6	$r_{2,7} - r_{4,9}$	$\nu(C{=}O)_{as}$
S_7	$4r_{3,4} - r_{5,4} - r_{1,5} - r_{2,1} - r_{3,2}$	ν_1(ring)
S_8	$r_{5,4} + r_{1,5} - r_{2,1} - r_{3,2}$	ν_2(ring)
S_9	$r_{5,4} - r_{1,5} - r_{2,1} + r_{3,2}$	ν_3(ring)
S_{10}	$r_{5,4} - r_{1,5} + r_{2,1} - r_{3,2}$	ν_4(ring)
S_{11}	$r_{3,4} + r_{5,4} + r_{1,5} + r_{2,1} + r_{3,2}$	ν_5(ring)
S_{12}	$r_{12,6} + r_{13,6} + r_{14,6}$	$\nu(CH_3)_s$
S_{13}	$2r_{13,6} - r_{12,6} - r_{14,6}$	$\nu(CH_3)_{as}'$
S_{14}	$r_{12,6} - r_{14,6}$	$\nu(CH_3)_{as}''$
S_{15}	$\beta_{2,4,3} - 0.809\beta_{3,5,4} - 0.809\beta_{3,1,2} + 0.309\beta_{1,4,5} + 0.309\beta_{2,5,1}$	δ_1(ring)
S_{16}	$-1.118\beta_{3,5,4} + 1.118\beta_{3,1,2} - 1.809\beta_{1,4,5} + 1.809\beta_{2,5,1}$	δ_2(ring)
S_{17}	$\beta_{4,8,3} - \beta_{2,8,3}$	δ(NH)
S_{18}	$\beta_{3,7,2} - \beta_{1,7,2} + \beta_{3,9,4} - \beta_{5,9,4}$	$\delta(C{=}O)_s$
S_{19}	$\beta_{2,6,1} - \beta_{5,6,1}$	δ(NC)
S_{20}	$\beta_{3,9,4} - \beta_{5,9,4} - \beta_{3,9,4} + \beta_{5,9,4}$	$\delta(C{=}O)_{as}$
S_{21}	$5\beta_{10,11,5} - \beta_{1,10,5} - \beta_{1,11,5} - \beta_{4,10,5} - \beta_{4,11,5}$	$\delta(CH_2)$
S_{22}	$\beta_{1,10,5} - \beta_{1,11,5} + \beta_{4,10,5} - \beta_{4,11,5}$	$\gamma(CH_2)$
S_{23}	$\beta_{1,10,5} + \beta_{1,11,5} - \beta_{4,10,5} - \beta_{4,11,5}$	$w(CH_2)$
S_{24}	$\beta_{1,10,5} - \beta_{1,11,5} - \beta_{4,10,5} + \beta_{4,11,5}$	$tw(CH_2)$
S_{25}	$2\beta_{12,14,6} - \beta_{12,13,6} - \beta_{13,14,6}$	$\delta(CH_3)_{as}'$
S_{26}	$\beta_{12,13,6} - \beta_{13,14,6}$	$\delta CH_3)_{as}''$
S_{27}	$2\beta_{13,1,6} - \beta_{12,1,6} - \beta_{14,1,6}$	$\gamma(CH_3)'$
S_{28}	$\beta_{12,1,6} - \beta_{14,1,6}$	$\gamma(CH_3)''$
S_{29}	$\beta_{13,1,6} + \beta_{12,1,6} + \beta_{14,1,6} - \beta_{12,13,6} - \beta_{12,14,6} - \beta_{13,14,6}$	$\delta(CH_3)_s$
S_{30}	$0.309\tau_{3,4,5,1} + 0.309\tau_{2,3,4,5} - 0.809\tau_{4,5,1,2} - 0.809\tau_{1,2,3,4} + \tau_{5,1,2,3}$	τ_1(ring)
S_{31}	$-1.118\tau_{1,2,3,4} + 1.118\tau_{4,5,1,2} - 1.809\tau_{2,3,4,5} + 1.809\tau_{3,4,5,1}$	τ_2(ring)
S_{32}	$\tau_{2,1,6,12} + \tau_{2,1,6,13} + \tau_{2,1,6,14}$	$\tau(CH_3)$
S_{33}	$\gamma_{6,2,1,5}$	γ(NC)
S_{34}	$\gamma_{7,3,2,1}$	γ(C=O7)
S_{35}	$\gamma_{8,4,3,2}$	γ(NH)
S_{36}	$\gamma_{9,5,4,3}$	γ(C=O9)

[a] See Scheme 3.1 for atom numbering. [b] $r_{i,j}$ is the distance between atoms A_i and A_j; $\beta_{i,j,k}$ is the angle between vectors A_kA_i and A_kA_j; $\tau_{i,j,k,l}$ is the dihedral angle between the plane defined by A_i, A_j, A_k and the plane defined by A_j, A_k, A_l atoms; $\gamma_{i,j,k,l}$ is the angle between the vector A_kA_i and the plane defined by atoms A_j, A_k, A_l. [c] w, wagging; tw, twisting; γ, rocking; ν, stretching; δ, bending; τ, torsion; s, symmetric; as, anti-symmetric.

Table 3.11 Infrared spectrum of monomeric 1-MH in argon matrix (10 K) and DFT(B3LYP)/6-311G++(d,p) calculated infrared spectrum and potential energy distributions (PED).[a]

Experimental (Ar matrix; 10 K)	Calculated		
Freq [b]	Freq [b]	I_{IR} [c]	PED [d] (%)
3488/ 3482	3486	85	$\nu(NH)$ (100)
n.obs.	3076	1	$\nu(CH_3)_{as}'$ (91)
2962/ 2960	3004	21	$\nu(CH_3)_{as}''$ (93)
2951	2995	21	$\nu(CH_2)_a$(93)
2930	2964	28	$\nu(CH_2)_s$ (95)
2927/ 2883[e]	2956	55	$\nu(CH_3)_s$ (87)
1805/ 1803	1804	174	$\nu(C=O)_s$ (82)
1771/ 1768/ ~1753	1770	1053	$\nu(C=O)_{as}$ (76) + ν_2(ring) (12)
1505/ 1492	1498	34	$\delta(CH_3)_{as}'$ (98) + $\delta(CH_2)$ (12) +$\gamma(CH_3)'$ (12)
1457/ 1455	1464	12	$\delta(CH_3)_{as}''$ (92)
1456/ 1454	1461	52	$\delta(CH_2)$ (67) + $\delta(CH_3)_{as}'$ (25)
1430/ 1427	1426	39	$\delta(CH_3)_s$ (50) + $\delta(CH_2)$ (14) + $\delta(CH_3)_{as}'$ (12)
1413/ 1412/ 1407/ 1404/ 1401/ 1396	1406	124	ν_2(ring) (32) + $\delta(CH_3)_s$ (31) + w(CH_2) (11) + δ_2 (ring) (11)
1343/ 1342/ 1337/ 1335	1331	45	$\delta(NH)$ (53) + ν_1(ring) (25) + $\nu(C=O)_{as}$ (11)
1319/ 1316	1303	138	ν_4(ring) (20) + ν_1(ring) (19) + $\delta(C=O)_s$ (17) + $\delta(NH)$ (11)
1295/ 1292	1278	14	$\gamma(CH_3)'$ (18) + ν_2(ring) (15) + ν_4(ring) (15) + ν(NC) (15)
1237/ 1235/ 1232	1233	35	w(CH_2) (60) + ν(NC) (19)
1180/1176	1178	4	tw(CH_2) (82)
1131	1125	0.2	$\gamma(CH_3)''$ (80) + tw(CH_2) (11)
1121/ 1119/ 1116/ 1112/ 1108	1099	103	ν_1(ring) (29) + ν_3(ring) (15) + $\gamma(CH_3)'$ (11) + $\delta(NH)$ (10)
1029/ 1028	1020	42	$\gamma(CH_3)'$ (44) + ν_2(ring) (23) + ν_3(ring) (10)
995/ 986	990	0.2	$\gamma(CH_2)$ (75)
884/ 883	873	15	ν_5(ring) (30) + δ_2 (ring) (21) + ν_4(ring) (20)
816	805	6	ν_5(ring) (24) + ν(NC) (19) + ν_3(ring) (19) + ν_2(ring) (16)
752	739	12	γ(C=O7) (96)
688	680	7	δ_1 (ring) (39) + ν_3(ring) (13) + $\delta(C=O)_{as}$ (13)
594/ 591/ 588/ 586/ 582	581	49	γ(C=O9) (70) + γ(NH) (29) + $\gamma(CH_2)$ (12)
	580	8	δ_1 (ring) (24) + $\delta(C=O)_{as}$ (24) + ν_5(ring) (16) + ν_3(ring) (15)
555/ 554	547	22	δ_2 (ring) (43) + $\delta(C=O)_{as}$ (31) + ν(NC) (14)
530/ 527	526	77	$\gamma(NH)$ (76)
n.i.	377	22	$\delta(C=O)_s$ (65) + ν_1(ring) (12)
n.i.	280	2	δ(NC) (76) + ν_2(ring) (10) + $\delta(C=O)_{as}$ (10)
n.i.	191	1	τ_1 (ring) (102)
n.i.	157	6	γ(NC) (43) + τ_2 (ring) (24) + $\tau(CH_3)$ (22) + τ_1 (ring) (11)
n.i.	119	2	τ_2 (ring) (72) + $\tau(CH_3)$ (38)
n.i.	79	0.4	γ(NC) (88) + $\tau(CH_3)$ (36)

[a] See Table 3.10 (Supporting Information) for definition of the symmetry coordinates and Scheme 3.1 for atom numbering. Abbreviations: w, wagging; tw, twisting; γ, rocking; ν, stretching; δ, bending; τ, torsion; s, symmetric; as, anti-symmetric;. [b] Wavenumbers in cm^{-1}; n.obs., not observed; n.i., not investigated. [c] IR intensities in km mol^{-1}. [d] PED's lower than 10% are not shown; symmetry of the vibrations are given in square brackets. [e] The $\nu(CH_3)_s$ mode participates in a Fermi resonance interaction with the first overtone of the $\delta(CH_3)_{as}''$ mode, whose fundamental is observed at 1457/1455 cm^{-1} (matrix-site split band); other overtones and combination tones observed in the CH stretching region of the spectrum appear at 2983 (2x1492), 2868 (1455+1412), 2846 (2x1426) and 2802 (2x2808) cm^{-1}.

For 1-MH, the good overall agreement between the calculated and the experimental spectra assures a reliable assignment of the experimental IR bands. In the following discussion, only the structurally most relevant features of the spectrum of 1-MH will be considered.

The most intense features in the infrared spectra of 1-MH (1771/1768 and 1753 cm^{-1}) are due to the anti-symmetric carbonyl stretching vibration, $\nu(C=O)_{as}$, interacting by Fermi resonance with the first overtone of the ring skeletal vibration which fundamental vibration mode is observed at 884/883 cm^{-1}. A similar Fermi resonance interaction was found to take place in the case of the parent hydantoin.[16] The relatively intense band associated with the symmetric carbonyl stretching vibration (calculated at 1804 cm^{-1}) is observed as a site-split doublet at 1805 and 1803 cm^{-1}. The bands due to the three vibrations of the NH group are observed as site-split features at 3488/3482 (stretching ν(NH)), ~1340 (in-plane bending δ(NH), exhibiting four components), and 530/527 cm^{-1} (out-of-plane rocking, γ(NH)). These are the features which can be anticipated to undergo larger changes with the sampling conditions, in particular in going from the matrix-isolated monomer to the condensed phases. As described in detail below, in the spectra of the neat compound in solid state (either in amorphous or in crystalline phases) these bands shift considerably to higher and lower frequencies, respectively in case of the bending and stretching modes. These characteristic frequency shifts upon hydrogen bond formation in the solid states, as well as the strong dependence with temperature of the bands position, intensity and profile, and good reproduction of the spectra for the isolated monomer by theoretical calculations (calculated values: 3486, 1331, and 526 cm^{-1}, for stretching, in-plane bending and rocking modes, respectively), allowed for a secure assignment of the three vibrations originated in the NH group.

As it is usual for matrix-isolated molecules, the bands in the CH stretching region appear with a comparatively reduced intensity, and the proposed assignments are tentative (the spectra obtained for the neat solid compound do not help to increase the certainty of the assignments because in these cases the CH stretching bands appear superimposed to the strong downshifted bands due to the hydrogen-bonded NH stretching modes). On the other hand, the assignments for the CH bending and rocking modes are unequivocal (see Table 3.13 and Figure 3.1).

The skeletal vibrations could also be easily assigned, since these vibrations were very well predicted by the calculations. Two of the ring stretching modes are predicted by the calculations to have a relevant contribution from the δ(NH) coordinate (bands calculated at 1303 and 1099 cm^{-1}, mainly associated with the ν_4(ring) and ν_1(ring) coordinates; see Tables 3.10 and 3.11). Accordingly, the corresponding observed bands (1319/1316 and multiplet at ca. 1120-1108 cm^{-1}) were also found to exhibit larger frequency shifts in going from the isolated monomer to the neat solid compound (details will be provided in Section 3.5).

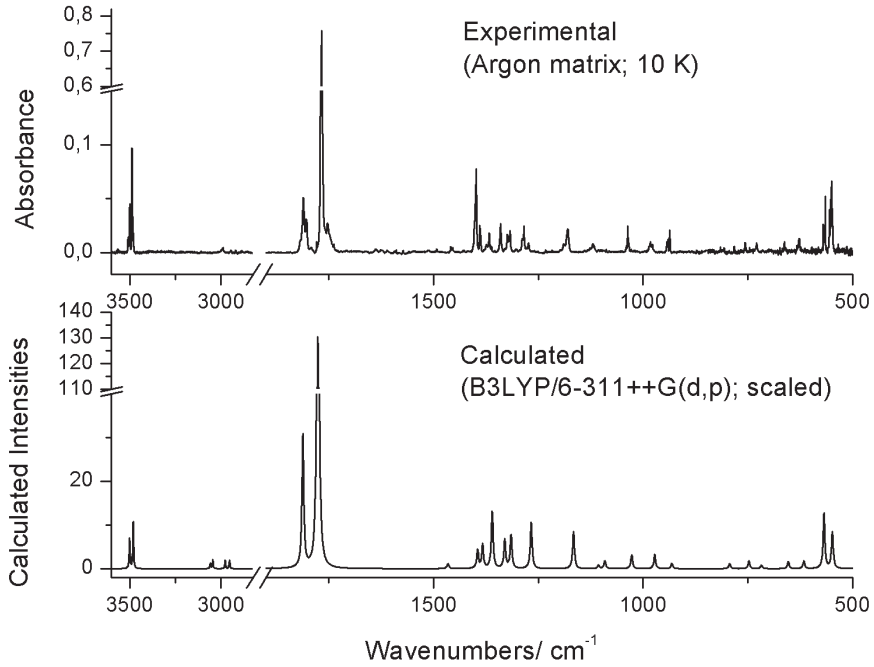

Figure 3.2 – Experimental infrared spectrum of monomeric 5-MH isolated in an argon matrix at 10 K (*top*) and simulated spectrum of 5-MH monomer using Lorentzian functions centered at the scaled B3LYP/6-311++G(d,p) calculated wavenumbers (*bottom*). Note that the calculated intensities correspond, in the simulated spectrum, to the areas below the Lorentzian functions, not to peak intensities.

As for 1-MH, the good global agreement between the experimental and calculated spectra for 5-MH assures an accurate assignment of the experimental IR bands. The most relevant features are considered in the following discussion.

The most intense band in the infrared spectrum of 5-MH corresponds $\nu(C=O)_{as}$, and it is observed at 1768 cm^{-1} (in the calculated spectrum this band appears at 1776 cm^{-1}). Similarly to both the parent hydantoin[16] and 1-MH, the band at ~1753 cm^{-1} can be interpreted in terms of Fermi resonance interaction between $\nu(C=O)_{as}$ and the first overtone of the ring skeletal vibration which fundamental appears at 782 cm^{-1}. The band associated with the symmetric carbonyl stretching vibration appears at 1811 cm^{-1} in the experimental spectrum, matching very well the calculated frequency for this vibration (1812 cm^{-1}).

The bands due to the NH group vibrations are observed as site-split features at 3510/3499 cm^{-1} (stretching, ν(N1-H6)), 3491/3487/3481 cm^{-1} (stretching, ν(N3-H8)), 1403/1399 and 1341 cm^{-1} (in plane bending, δ(NH), of N1-H6 and N3-H8, respectively) and 570/565 cm^{-1} (out-of-plane rocking, γ(NH), of N3-H8). The calculated frequency for the out-of-plane rocking of N1-H6 (347 cm^{-1}) is below the limit of the investigated frequencies in the argon matrix experiment.

Table 3.12 Internal coordinates used in the normal modes analysis of 5-MH

Coordinate	Definition [b]	Approximate description [c]
S_1	$r_{1,6}$	ν (NH)′
S_2	$r_{3,8}$	ν (NH)″
S_3	$r_{5,10}$	ν(CH)
S_4	$r_{5,11}$	ν(CC)
S_5	$r_{2,7} + r_{4,9}$	ν(C=O)′
S_6	$r_{2,7} - r_{4,9}$	ν(C=O)″
S_7	$4r_{3,4} - r_{5,4} - r_{1,5} - r_{2,1} - r_{3,2}$	ν_1(ring)
S_8	$r_{5,4} + r_{1,5} - r_{2,1} - r_{3,2}$	ν_2(ring)
S_9	$r_{5,4} - r_{1,5} - r_{2,1} + r_{3,2}$	ν_3(ring)
S_{10}	$r_{5,4} - r_{1,5} + r_{2,1} - r_{3,2}$	ν_4(ring)
S_{11}	$r_{3,4} + r_{5,4} + r_{1,5} + r_{2,1} + r_{3,2}$	ν_5(ring)
S_{12}	$r_{12,11} + r_{13,11} + r_{14,11}$	ν(CH_3)s
S_{13}	$2r_{12,11} - r_{13,11} - r_{14,11}$	ν(CH_3)$_{as}$′
S_{14}	$r_{13,11} - r_{14,11}$	ν(CH_3)$_{as}$″
S_{15}	$\beta_{2,4,3} - 0.809\beta_{3,5,4} - 0.809\beta_{3,1,2} + 0.309\beta_{1,4,5} + 0.309\beta_{2,5,1}$	δ_1 (ring)
S_{16}	$-1.118\beta_{3,5,4} + 1.118\beta_{3,1,2} - 1.809\beta_{1,4,5} + 1.809\beta_{2,5,1}$	δ_2 (ring)
S_{17}	$\beta_{4,8,3} - \beta_{2,8,3}$	δ(NH)″
S_{18}	$\beta_{3,7,2} - \beta_{1,7,2}$	δ(C=O)′
S_{19}	$\beta_{2,6,1} - \beta_{5,6,1}$	δ(NH)′
S_{20}	$\beta_{3,9,4} - \beta_{5,9,4}$	δ(C=O)″
S_{21}	$-\beta_{1,11,5} - \beta_{4,11,5} - \beta_{1,10,5} - \beta_{4,10,5} + 4\beta_{11,10,5}$	γ(CH)
S_{22}	$\beta_{1,10,5} - \beta_{4,10,5}$	δ(CH)
S_{23}	$\beta_{1,11,5} - \beta_{4,11,5}$	δ(C-CH_3)
S_{24}	$\beta_{1,11,5} + \beta_{4,11,5} - \beta_{1,10,5} - \beta_{4,10,5}$	γ(C-CH_3)′
S_{25}	$2\beta_{12,14,11} - \beta_{12,13,11} - \beta_{13,14,11}$	γ(CH_3)$_{as}$′
S_{26}	$\beta_{12,14,11} - \beta_{13,14,11}$	γ(CH_3)$_{as}$″
S_{27}	$2\beta_{13,5,11} - \beta_{12,5,11} - \beta_{14,5,11}$	δ(CH_3)$_{as}$′
S_{28}	$\beta_{12,5,11} - \beta_{14,5,11}$	δ(CH_3)$_{as}$″
S_{29}	$\beta_{13,5,11} + \beta_{12,5,11} + \beta_{14,5,11} - \beta_{12,13,11} - \beta_{12,14,11} - \beta_{13,14,11}$	δ(CH_3)$_s$
S_{30}	$0.309\tau_{3,4,5,1} + 0.309\tau_{2,3,4,5} - 0.809\tau_{4,5,1,2} - 0.809\tau_{1,2,3,4} + \tau_{5,1,2,3}$	τ_1 (ring)
S_{31}	$-1.118\tau_{1,2,3,4} + 1.118\tau_{4,5,1,2} - 1.809\tau_{2,3,4,5} + 1.809\tau_{3,4,5,1}$	τ_2 (ring)
S_{32}	$\tau_{4,5,11,12} + \tau_{4,5,11,13} + \tau_{4,5,11,14}$	τ(CH_3-ring)
S_{33}	$\gamma_{6,5,1,2}$	γ(NH)′
S_{34}	$\gamma_{7,3,2,1}$	γ(C=O)′
S_{35}	$\gamma_{8,4,3,2}$	γ(NH)″
S_{36}	$\gamma_{9,5,4,3}$	γ(C=O)″

[a] See Scheme 3.1 for atom numbering. [b] $r_{i,j}$ is the distance between atoms A_i and A_j; $\beta_{i,j,k}$ is the angle between vectors A_kA_i and A_kA_j; $\tau_{i,j,k,l}$ is the dihedral angle between the plane defined by A_i, A_j, A_k and the plane defined by A_j, A_k, A_l atoms; $\gamma_{i,j,k,l}$ is the angle between the vector A_kA_i and the plane defined by atoms A_j, A_k, A_l. [c] w, wagging; tw, twisting; γ, rocking; ν, stretching; δ, bending; τ, torsion; s, symmetric; as, anti-symmetric.

Table 3.13 Infrared spectrum of monomeric 5-MH in argon matrix (10 K) and DFT(B3LYP)/6-311G++(d,p) calculated infrared spectrum and potential energy distributions (PED).[a]

Experimental (Ar matrix; 10 K)	Calculated		
Freq.[b]	Freq.	I_{IR}[c]	PED[d] (%)
3510/3499	3501	54	ν(NH) ′(100)
3491/3487/3481	3481	84	ν(NH) " (100)
2990	3059	10	$\nu(CH_3)_{as}$" (93)
2947	3046	17	$\nu(CH_3)_{as}$' (93)
2920	2978	15	$\nu(CH_3)_s$ (99)
2988	2954	16	ν(CH) (87)
1811	1812	238	$\nu(C=O)_s$ (79)
1768/ ~1753	1776	1024	$\nu(C=O)_{as}$ (76)
1459	1467	2	$\gamma(CH_3)_{as}$' (87)
1454	1465	8	$\gamma(CH_3)_{as}$" (85)
1403/1399	1395	32	δ(NH) '(41) + $\delta(CH_3)_s$ (12) + δ(CH) (11)
1390	1383	43	$\delta(CH_3)_s$ (77)
1367	1360	102	ν(NH) ′(15)+ ν(C=O)′ (11) + ν_4(ring) (11)
1341	1330	52	δ(NH)″(49) +ν_1(ring) (20)
1324/1317	1315	60	γ(CH) (43) + δ(NH)″(13) + $\gamma(C\text{-}CH_3)$' (10)
1284	1267	84	δ(CH) (28)+ ν_4(ring) (12)+ δ(NH)' (10)
1179	1166	67	δ(CH) (29)+ ν_1(ring) (18)+ ν_3(ring) (11)+ δ_2(ring) (11)
1119	1106	7	$\delta(CH_3)_{as}$" (23) +δ(CH) (13)+ δ(NH)' (12)+ ν_4(ring) (11)+ ν_2(ring) (10)
1088	1091	14	$\delta(CH_3)_{as}$' (36)+ ν(CC) (35) + $\gamma(C\text{-}CH_3)$' (13)
1036	1027	25	$\delta(CH_3)_{as}$" (20)+ $\delta(CH_3)_{as}$' (15) + ν(CC) (13)
982/978	972	26	ν_2(ring) (26) + ν_5(ring) (21)+ ν_1(ring) (11)
943/940/937/936	931	10	$\delta(CH_3)_{as}$' (26)+ δ_2(ring) (21) + ν_4(ring) (14)+ ν_1(ring) (11)
782	793	10	ν_5(ring) (25)+ $\delta(CH_3)_{as}$' (14)+ γ(C=O)" (11)
756	747	14	γ(C=O)' (87)
729	717	6	γ(C=O)" (35)
664/662	653	12	δ_2(ring) (17) + γ(C=O)" (16) + ν_3(ring) (15)
629/627	616	14	δ_1(ring) (49)+ ν_5(ring) (16)+ δ_2(ring) (10)
570/565	568	99	γ(NH)" (64) + δ(C=O)' (16)+ δ(C=O)" (12)
555/550	548	65	γ(NH)" (38) + δ(C=O)' (20)+ δ_2(ring) (14)+ δ(C=O)" (13)
n.i.	433	16	$\gamma(C\text{-}CH_3)$' (15) + τ_1(ring) (69) + γ(NH)' (72)
n.i.	377	15	δ(C=O)' (31)+ δ(C=O)" (26)
n.i.	347	67	γ(NH)' (72) + $\gamma(C\text{-}CH_3)$' (15) + $\delta(C\text{-}CH_3)$ (13)
n.i.	237	6	$\delta(C\text{-}CH_3)$ (56) + γ(C=O)" (12) + $\gamma(C\text{-}CH_3)$' (10)
n.i.	227	0.3	$\tau(CH_3\text{-ring})$ (96)
n.i.	130	0.4	τ_2(ring) (76) + τ_1(ring) (18)
n.i.	78	6	τ_1(ring) (69) + τ_2(ring) (23)

[a]See Table 3.12 for the definition of symmetry coordinates and Scheme 3.1 for atom numbering. Abreeviation: s, symmetric; as, anti-symmetric; scis, scissoring; wag, wagging; twist, twisting; rock, rocking; ν, stretching; δ, in-plane bending; **γ**, out-of-plane bending; τ, torsion. [b]Wavenumbers in cm^{-1}; n.i., not investigated. [c]IR intensities in km mol^{-1}. [d]PED's lower than 10% not shown.

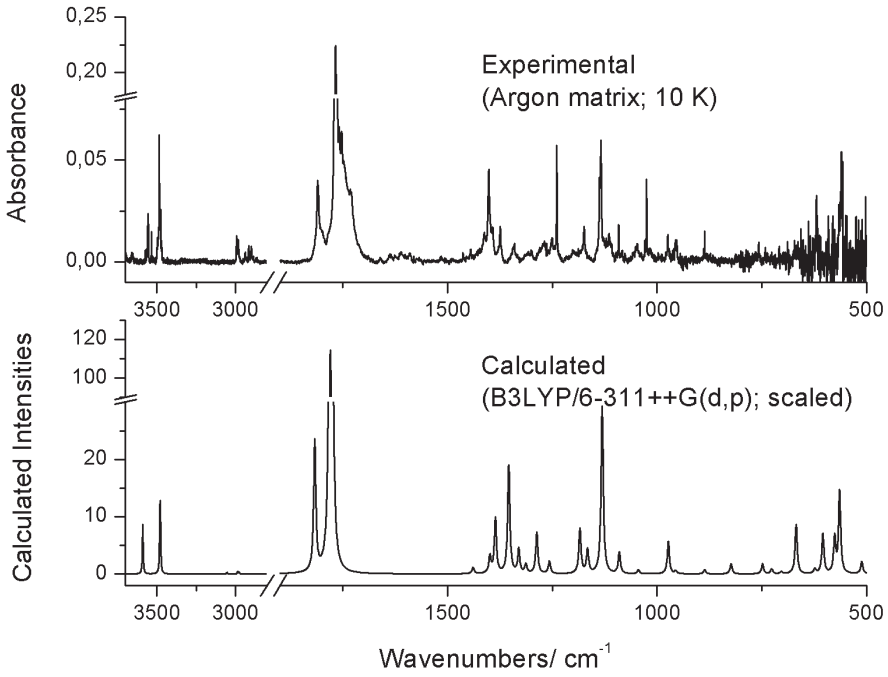

Figure 3.3 – Experimental infrared spectrum of monomeric 5-HAA isolated in an argon matrix at 10 K (*top*) and simulated spectrum of 5-HAA monomer using Lorentzian functions centered at the scaled B3LYP/6-311++G(d,p) calculated wavenumbers (*bottom*). Note that the calculated intensities correspond, in the simulated spectrum, to the areas below the Lorentzian functions, not to peak intensities.

As explained before, we can anticipate that the NH related bands undergo large changes when going from the matrix-isolated monomer to the neat solid state, as we will discuss in Section 3.5. The calculated values for the observed NH modes (3501, 3481, 1395, 1330, 568 cm^{-1}, respectively) show a good concordance with the experimental spectra.

The tentative assignments for the bands in the CH stretching region are shown in Table 3.13. The assignments for the CH and CH_3 bending and rocking modes are unequivocal and correspond to the bands at 1459, 1454, 1390, 1324/1317, 1179, 1119, 1088, 1036 and 943/940/937/936 cm^{-1} (see Table 3.13 and Figure 3.2).

The ring skeletal vibrations are well predicted by the calculations. The band calculated at 1166 $cm^{-1,}$ which appears in the experimental spectrum at 1179 cm^{-1}, corresponds to the ν_1(ring) and ν_3(ring) modes and is predicted by the calculations to have a strong contribution from the δ(CH) coordinate.

For 5-HAA, the experimental and calculated spectra (presented in Figure 3.3) show also a good overall agreement, once again assuring a reliable assignment of the experimental IR bands.

Table 3.14 Internal coordinates used in the normal modes analysis of 5-HAA

Coordinate	Definition [b]	Approximate description [c]
S_1	$r_{1,6}$	ν (NH)′
S_2	$r_{3,8}$	ν (NH)″
S_3	$r_{5,10}$	ν(CH)
S_4	$r_{5,11}$	ν(CC)
S_5	$r_{2,7} + r_{4,9}$	ν(C=O)′
S_6	$r_{2,7} - r_{4,9}$	ν(C=O)″
S_7	$4r_{3,4} - r_{5,4} - r_{1,5} - r_{2,1} - r_{3,2}$	ν_1(ring)
S_8	$r_{5,4} + r_{1,5} - r_{2,1} - r_{3,2}$	ν_2(ring)
S_9	$r_{5,4} - r_{1,5} - r_{2,1} + r_{3,2}$	ν_3(ring)
S_{10}	$r_{5,4} - r_{1,5} + r_{2,1} - r_{3,2}$	ν_4(ring)
S_{11}	$r_{3,4} + r_{5,4} + r_{1,5} + r_{2,1} + r_{3,2}$	ν_5(ring)
S_{12}	$r_{11,12} + r_{11,13}$	$\nu(CH_2)_s$
S_{13}	$r_{11,12} - r_{11,13}$	$\nu(CH_2)_{as}$
S_{14}	$\beta_{2,4,3} - 0.809\beta_{3,5,4} - 0.809\beta_{3,1,2} + 0.309\beta_{1,4,5} + 0.309\beta_{2,5,1}$	δ_1 (ring)
S_{15}	$-1.118\beta_{3,5,4} + 1.118\beta_{3,1,2} - 1.809\beta_{1,4,5} + 1.809\beta_{2,5,1}$	δ_2 (ring)
S_{16}	$\beta_{4,8,3} - \beta_{2,8,3}$	δ(NH)"
S_{17}	$\beta_{3,7,2} - \beta_{1,7,2}$	δ(C=O)'
S_{18}	$\beta_{2,6,1} - \beta_{5,6,1}$	δ(NH)'
S_{19}	$\beta_{3,9,4} - \beta_{5,9,4}$	δ(C=O)"
S_{20}	$-\beta_{1,11,5} - \beta_{4,11,5} - \beta_{1,10,5} - \beta_{4,10,5} + 4\beta_{11,10,5}$	γ(CH)
S_{21}	$\beta_{1,10,5} - \beta_{4,10,5}$	δ(CH)
S_{22}	$\beta_{1,11,5} - \beta_{4,11,5}$	$\delta(CCH_3)$
S_{23}	$\beta_{1,11,5} + \beta_{4,11,5} - \beta_{1,10,5} - \beta_{4,10,5}$	$\gamma(CCH_3)$
S_{24}	$4\beta_{12,13,11} - \beta_{12,5,11} - \beta_{13,5,11} - \beta_{12,14,11} - \beta_{13,14,11}$	$\delta_{scis}(CH_2)$
S_{25}	$\beta_{12,5,11} + \beta_{13,5,11} - \beta_{12,14,11} - \beta_{13,14,11}$	$w(CH_2)$
S_{26}	$\beta_{12,5,11} - \beta_{13,5,11} - \beta_{12,14,11} + \beta_{13,14,11}$	$tw(CH_2)$
S_{27}	$\beta_{12,5,11} - \beta_{13,5,11} + \beta_{12,14,11} - \beta_{13,14,11}$	$\gamma(CH_2)$
S_{28}	$\beta_{5,14,11}$	δ(CCC)
S_{29}	$\tau_{4,5,11,12} + \tau_{4,5,11,13} + \tau_{4,5,11,14}$	τ(CCC)
S_{30}	$\tau_{16,14,11,5} + \tau_{16,14,11,12} + \tau_{16,14,11,13}$	τ(CCO)
S_{31}	$0.309\tau_{3,4,5,1} + 0.309\tau_{2,3,4,5} + 0.809\tau_{4,5,1,2} - 0.809\tau_{1,2,3,4} + \tau_{5,1,2,3}$	τ_1 (ring)
S_{32}	$-1.118\tau_{1,2,3,4} + 1.118\tau_{4,5,1,2} - 1.809\tau_{2,3,4,5} + 1.809\tau_{3,4,5,1}$	τ_2 (ring)
S_{33}	$\gamma_{6,5,1,2}$	γ(NH)'
S_{34}	$\gamma_{7,3,2,1}$	γ(C=O)'
S_{35}	$\gamma_{8,4,3,2}$	γ(NH)"
S_{36}	$\gamma_{9,5,4,3}$	γ(C=O)"
S_{37}	$r_{14,15}$	ν(C=O)
S_{38}	$r_{14,16}$	ν(CO)
S_{39}	$r_{16,17}$	ν(OH)
S_{40}	$r_{11,14}$	ν(CC)
S_{41}	$\beta_{11,15,14}$	δ(CC=O)
S_{42}	$\beta_{11,16,14}$	δ(CCO)
S_{43}	$\beta_{14,17,16}$	δ(COH)
S_{44}	$\tau_{15,14,16,17}$	τ(O=COH)
S_{45}	$\tau_{11,15,14,16}$	τ(O=CCO)

[a] See Scheme 3.1 for atom numbering. [b] $r_{i,j}$ is the distance between atoms A_i and A_j; $\beta_{i,j,k}$ is the angle between vectors A_kA_i and A_kA_j; $\tau_{i,j,k,l}$ is the dihedral angle between the plane defined by A_i, A_j, A_k and the plane defined by A_j, A_k, A_l atoms; $\gamma_{i,j,k,l}$ is the angle between the vector A_kA_i and the plane defined by atoms A_j, A_k, A_l. [c] w, wagging; tw, twisting; γ, rocking; ν, stretching; δ, bending; τ, torsion; s, symmetric; as, anti-symmetric.

Table 3.15 Infrared spectrum of monomeric 5-HAA in argon matrix (10 K) and DFT(B3LYP)/6-311G++(d,p) calculated infrared spectrum and potential energy distributions (PED).[a]

Experimental Ar matrix	Calculated		
Freq[b]	Freq[b]	I_{IR}[c]	PED[d] (%)
3557/3534	3590	81	ν(OH) (100)
3485	3482	40	ν(NH)' (98)
3477	3479	100	ν(NH)" (98)
2994	3054	3	$\nu(CH_2)_{as}$ (81) +$\nu(CH_2)_s$ (19)
2985	2986	4	$\nu(CH_2)_s$ (81) +$\nu(CH_2)_{as}$ (19)
2939/2917/2899	2978	3	ν(CH) (99)
1810	1817	214	ν(C=O)′ (80)
1767/~1753	1781	979	ν(C=O)″ (63) + ν(C=O) (16)
1752	1775	376	ν(C=O) (70) + ν(C=O)″ (14)
1444	1439	10	$\delta_{scis}(CH_2)$ (98)
1401	1399	28	δ(NH)' '(46) + δ(CH) (15)
1374	1386	91	$w(CH_2)$ (26) + γ(CH) (16) + ν(CC) (10)
1340	1353	177	ν_1(ring) (21)+ ν_4(ring) (15) + δ(C=O)' (14)
1306	1330	40	δ(NH)" (16) +ν_1(ring) (13)
1300	1313	15	γ(CH) (36) + δ(COH) (17)
1269	1288	68	$w(CH_2)$ (17)+ δ(CH) (13)+ $tw(CH_2)$ (13) + ν_4(ring) (12) + δ(NH)' (10)
1250/1239	1257	20	$w(CH_2)$ (30)+ δ(COH) (26)+ δ(CH) (16)
1174	1184	74	$tw(CH_2)$ (45) δ(COH) (10)
n. obs.	1166	40	δ(CH) (26)+ ν_1(ring) (18) + δ_2 (ring) (10)
1137/1133	1131	275	ν(CO) (35)+ $tw(CH_2)$ (17) + δ(COH) (17)
1091	1090	35	ν(CC) (25) + ν_3(ring) (14)+ ν_2(ring) (11) + δ(NH)' (10)
1028/1024	1044	6	ν(CC) (33)+ ν_4(ring) (16)
974	973	54	$\gamma(CH_2)$ (19)+ ν_2(ring) (19)+ ν_1(ring) (12)
955/953/951	955	5	ν_5(ring) (27) + $\gamma(CH_2)$ (24)
889/886	886	7	ν(CC) (44) + ν(CO) (11)
814/811/787	823	17	ν_5(ring) (21) + δ_2 (ring) (15)
757/741	748	17	γ(C=O)' (86)
725	726	8	ν_3(ring) (23) + ν_2(ring) (20)+ γ(C=O)" (11)
709/707	703	4	γ(C=O)" (41) + $\gamma(CH_2)$ (10)
688/671	668	81	τ(O=COH) (63) + τ(O=CCO) (13)
631	623	8	δ_1 (ring) (44)+ ν_5(ring) (21)
611/609	604	65	δ(CC=O) (31) + δ(CCO) (17) + δ_2(ring) (10)
581	575	58	γ(NH)" (46) + δ(C=O)' (19) + δ(C=O)" (14)
565/559	564	135	γ(NH)" (49) + τ(O=CCO) (10) + τ(O=COH) (10)
512/510	511	20	τ(O=CCO) (31) + δ(C=O)' (11)
467	457	49	γ(NH)' (52) + τ_1 (ring) (13)
433	426	58	γ(NH)' (33) + δ(CCO) (31) + δ(CC=O) (10)
n.i.	393	10	δ(C=O)" (31) + δ(C=O)' (21)
n.i.	312	6	δ(CCO) (18) + $\gamma(CCH_3)$ (18) + ν(CC) (14)
n.i.	247	5	$\delta(CCH_3)$ (40) + δ(CCC) (17)
n.i.	172	2	δ(CCC) (33) + τ_1 (ring) (19) + $\delta(CCH_3)$ (18)
n.i.	139	1	τ_2 (ring) (63) + τ_1 (ring) (27)
n.i.	74	0.1	τ(CCC) (29) + τ_2 (ring) (24) + τ_1 (ring) (19) + δ(CCC) (12)
n.i.	60	2	τ(CCO) (38) + τ(CCC) (31) + τ_1 (ring) (12)
n.i.	39	2	τ(CCO) (58) + τ(CCC) (31)

[a]See Table 3.14 for the definition of symmetry coordinates and Scheme 3.1 for atom numbering. Abreeviation: s, symmetric; as, anti-symmetric; scis, scissoring; wag, wagging; twist, twisting; rock, rocking; ν, stretching; δ, in-plane bending; **γ**, out-of-plane bending; τ, torsion. [b]Wavenumbers in cm^{-1}; n.i., not investigated. [c]IR intensities in km mol^{-1}. [d]PED's lower than 10% not shown.

The most intense feature in the infrared spectra of 5-HAA is due to the anti-symmetric carbonyl stretching vibration, analogously to what happens in both the 1-MH and 5-MH molecules. This band has its maximum at 1767 cm^{-1}. As for the other two studied hydantoins, and also for the parent hydantoin[16], a relatively intense band observed at ~1753 cm^{-1} corresponds to the second component of the Fermi doublet resulting from the interaction between the $\nu(C=O)_{as}$ stretching and the first overtone of a ring skeletal vibration (for 5-HAA the corresponding fundamental vibration appears at 814/883 cm^{-1}). The rather intense band observed at 1810 cm^{-1} is associated with the symmetric carbonyl stretching vibration (calculated at 1817 cm^{-1}).

The NH groups stretching vibrations (ν(NH)) are observed at 3485 and 3477 cm^{-1} and were calculated at 3482 and 3479 cm^{-1}, for N1–H6 and N3–H8, respectively. The in-plane bending (δ(NH)) modes are observed at 1401 and 1306 cm^{-1}, while the out-of-plane rocking (γ(NH)) modes are observed at 581, 565/559, 467 and 433 cm^{-1}. There are only two out-of-plane rocking NH modes, but they appear as four bands because these coordinates contribute to several vibrations of the molecule (see Table 3.15). These bands were calculated at 1399, 1330, 575, 564, 457 and 426 cm^{-1}. All these bands can be anticipated to have large shifts in spectra obtained in different conditions, namely when going from the matrix-isolated monomer to the neat solid states. As for 1-MH and 5-MH, the CH stretching bands of 5-HAA are observed with low intensities and, for this reason, the assignments proposed for these modes are tentative (see Table 3.15).

The ring skeletal vibrations in 5-HAA could be assigned with ease, since they are well predicted by the calculations. The combined stretching ν_1(ring) and ν_4(ring) mode is observed at 1340 cm^{-1} (calculated at 1353 cm^{-1}). The ν_5(ring) vibration corresponds to the bands observed at 955/953/951 cm^{-1} (calculated at 955 cm^{-1}) and 814/811/787 cm^{-1} (predicted theoretically at 823 cm^{-1}), which have also contributions from the out-of-plane bending of the CH_2 group and the in-plane bending motion δ_2 of the ring, respectively (see Table 3.15).

The OH stretching mode is observed at 3557/3534 cm^{-1} (calculated at 3590 cm^{-1}). Finally, one of the most intense observed features is due to the stretching vibration of the CO bond of the acid group, which is observed as a matrix site-split band at 1137/1133 cm^{-1} and is predicted theoretically at 1131 cm^{-1}, also in good agreement with the experimental data.

The bond lengths of the carbonyl bonds are shorter in 5-MH and 5-HAA compared to 1-MH (see Tables 3.1, 3.2 and 3.3). As a consequence, the symmetric carbonyl stretching vibration appears at higher frequencies for 5-MH and 5-HAA (1811 and 1810 cm^{-1}, respectively) in comparison with 1-MH (1805/1803 cm^{-1}) as it is presented in Tables 3.11, 3.13 and 3.15. Also, the relative values of N1-H6 bond length in 5-MH and 5-HAA (1.007 and 1.009 Å, respectively) reflects in the stretching frequencies of this bond (3510/3499 and 3485 cm^{-1}).

3.4 UV-induced Photolysis of Matrix-Isolated 1-MH

Scheme 3.3. Photoinduced Fragmentation Pathways of 1-MH monomer in an Argon Matrix upon 230 nm Excitation[a]

(a)

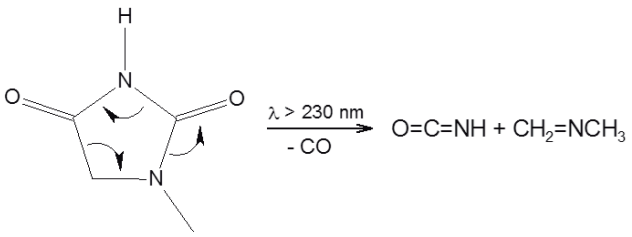

(b)

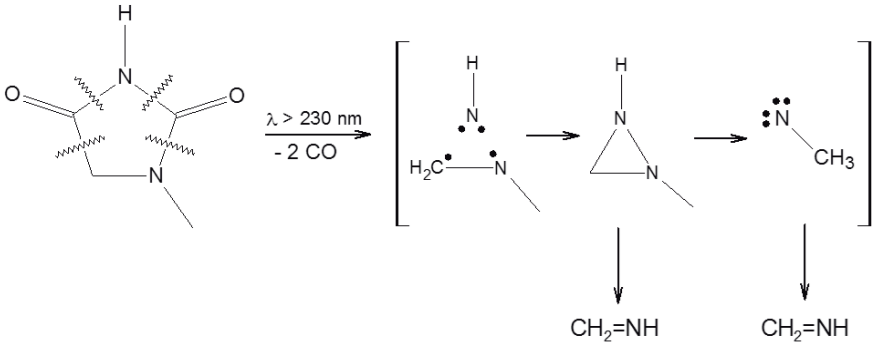

[a]Suggested intermediate species in the brackets were not observed (as discussed in the text).

In order to investigate the photochemistry of 1-methylhydantoin, the matrix-isolated 1-MH monomer was subjected to UV irradiation using two different experimental approaches: irradiation was performed through the outer quartz window of the cryostat either with broadband UV light produced by a Hg(Xe) lamp or narrowband UV light coming out from a laser/MOPO system (λ = 230 nm; fwhm 0.2 cm^{-1}), as described in Section 2.1.4. The broadband was found to lead to photochemical transformation of the compound only when the 234 nm filter was used (filters with a longer wavelength cutoff preclude the photoreaction to take place). Under these conditions, after around 7 hours of consecutive irradiation, the amount of 1-MH in the sample was reduced to ca. 25% of the initial. The experiments with the narrowband irradiation (λ = 230 nm) were found to be considerably more efficient than those performed with broadband excitation, though the observed spectral changes indicate that the induced photoprocesses are the same in the two experiments. Upon laser/MOPO irradiation of the sample, the initial amount of 1-MH was reduced to 25% after only about 1 hour of consecutive irradiation. The results of the performed photochemical experiment are compiled in Scheme 3.3, Figure 3.4 and Table 3.16.

Table 3.16 Infrared spectrum of the photolysed 1-MH in argon matrix (10 K, λ = 230 nm, 1 h), B3LYP/6-311G++(d,p) calculated spectra for the observed photoproducts and relevant literature data. [a]

		Calculated		Experimental	
		Freq.	I_{IR}	This study	Lit. Freq. [b]
	Isocyanic acid				
1	ν(NH)	3531	170	3339, 3336	3517, 3506
2	$\nu(NCO)_{as.}$	2292	783	2268, 2262, 2247, 2238	2259
3	$\nu(NCO)_{s.}$	1311	1	n.o.	n.o.
4	δ(HNC)	749	200	730	770
5	δ(NCO)	557	97	567	574
6	γ(NCO)	620	4	605	n.o.
	4+5			1327	1315
	Carbon monoxide				
	ν(CO)	2167	89	2145-2134	2138 (monomer)
	N-methyl-methylenimine				
1	$\nu(CH_2)_{as.}$	3064	28	3014	
2	$\nu(CH_3)_{as.}''$	3021	16	2977	
3	$\nu(CH_3)_{as.}'$	3003	24	2969	
4	$\nu(CH_2)_{s.}$	2916	90	2869	
5	$\nu(CH_3)_{s.}$	2905	44	2862	
6	ν(CN)	1699	19	1721, 1716	
7	$\delta(CH_2)$	1477	23	1472	
8	$\delta\ (CH_3)_{as.}'$	1449	2	1441	
9	$\delta\ (CH_3)_{as.}''$	1446	6	1436	
10	$\delta\ (CH_3)_{s.}$	1406	1	1412, 1411, 1405, 1403	
11	$w(CH_2)$	1213	15	1260, 1239, 1237	
12	$\gamma(CH_3)_{as.}''$	1117	1	n.o.	
13	$\gamma\ (CH_3)_{as.}'$	1101	<1	n.o.	
14	$\gamma\ (CH_2)$	1045	22	1039, 1034	
15	$\nu(NCH_3)$	944	15	962, 946, 935	
16	τ(C–N)	682	1	655	
17	δ(CNC)	469	6	495	
18	$\tau\ (CH_3)$	212	9	n.i.	
	methylenimine				
1	ν(NH)	3286	2	3301, 3298, 3295, 3292	3263[c]
2	$\nu(CH_2)_{as.}$	3050	33	3014	3085[d] 3036[e]
3	$\nu(CH_2)_{s.}$	2951	53	2932	2926[e]
4	ν(CN)	1673	25	1666	1650[d] 1641[e]
5	$\delta(CH_2)$	1463	7	1459, 1458	1460[d] 1453[e]
6	δ(HNC)	1343	35	1391, 1380	1358[d] 1348[e]
7	$w(CH_2)$	1139	47	1128, 1125, 1122, 1120	1113[d] 1123[e]
8	τ (C–N)	1083	18	1068, 1066	1072[d] 1063[e]
9	$\gamma(CH_2)$	1052	34	1046, 1044	1040[d] 1059[e]

[a] Wavenumbers in cm^{-1}; IR intensities in km mol^{-1}. Abbreviations: s, symmetric; as, anti-symmetric; w, wagging; ν, stretching; δ, in-plane bending; γ, rocking; τ, torsion; n.o., not observed; n.i., not investigated. [b] Literature data for isolated monomers: isocyanic acid,[105] carbon monoxide,[106] methylenimine: [c]-107, [d]-108, [e]-109.

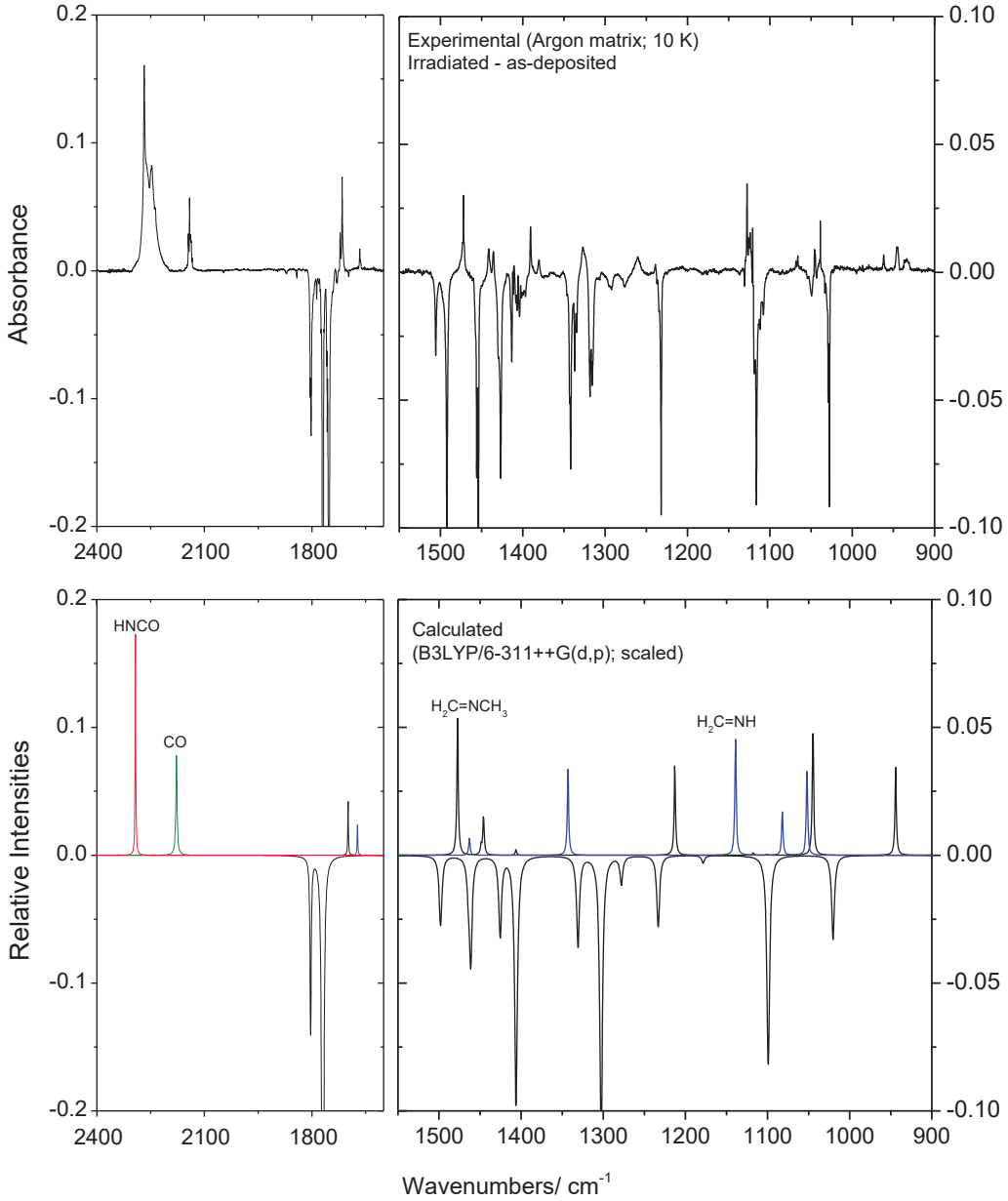

Figure 3.4 Experimental infrared difference spectrum: irradiated 1-MH matrix (λ= 230 nm; 1 h) *minus* as-deposited 1-MH matrix (*top*) and simulated difference spectrum based on the B3LYP/6-311++G(d,p) calculated (scaled) spectra of 1-MH, HNCO, CO, $H_2C{=}NH$ and $H_2C{=}NCH_3$ (*bottom*). The intensities of the different photoproducts in the simulated spectrum were multiplied by arbitrary factors to allow an easier comparison with the experimental data.

According to the observations, the 230 nm induced photolysis of the matrix-isolated 1-MH occurs through two different pathways: *(a)* OCNH + CO + $H_2C{=}NCH_3$ and *(b)* 2CO + $2H_2C{=}NH$. Since we were not able to capture any of the proposed intermediate species (see Scheme 3.3), the precise mechanisms of fragmentation are tentative.

The first pathway presented in Scheme 3 (pathway *a*) is most likely a concerted process where the weaker C2–N3 and C4–C5 bonds are cleaved, producing an isocyanic acid molecule (OCNH), and promote the cleavage of the stronger N1–C2 bond, yielding CO and *N*-methyl-methylenimine ($H_2C{=}NCH_3$). It should be noted that this pattern of fragmentation respects the theoretical indication[110] that the most strained fragment in the 1-MH molecule corresponds to the C5C4N3C2 moiety, i.e., that the elimination of isocyanic acid should be a favored fragmentation process in 1-methylhydanoin.

It should also be noted that the detachment of isocyanic acid from 1-MH has also been observed in other types of experiments, particularly electron-ionization mass spectrometry.[86,111–113] Furthermore, pathway *a* is identical to that previously reported in case of the 230 nm photoinduced transformation of the parent hydantoin molecule isolated in an argon matrix and subjected to identical experimental conditions.[16]

On the other hand, the second pathway presented in Scheme 3, pathway *b*, is most probably a more complex process, where extrusion of two molecules of carbon monoxide should led to formation of the NH radical, which then reacts with the remaining fragment, CH_2NCH_3, to produce two methylenimine molecules. This process may eventually occur *via* a cyclic *N*-methyl-diaziridine intermediate resulting from the radical recombination. Although this mechanism is only tentatively proposed, methyl nitrene shall be involved in the process (which shall convert to methylenimine by [1,2]-H shift). However, this putative intermediate species was also not detected in the present experiments.

The key products of *a* and *b* pathways are HCON and *N*-methyl-methylenimine in one side, and methylenimine in the other, as CO is produced in both pathways. As presented in Figure 3.4 and in Table 3.16, the presence of these products in the photolyzed 1-MH argon matrix is unequivocal. The small differences found in the positions of some of the bands of these species compared to literature data[105–109] result from the fact that in the present case the molecules are interacting in the matrix cage where they are formed with other species formed simultaneously from the same precursor molecules.

3.5 Investigation of Thermal Properties of 1-MH, 5-MH and 5-HAA

3.5.1 1-methylhydantoin

The crystalline structure of the purchased sample of 1-MH was identified as being the one described by Puszyńska-Tuszkanow et al.[86] and designated in a previous work as polymorph I.[110] According to the DSC studies that were performed, the melting of polymorph I occurs at T_{fus} = (155.7±0.7) ºC, with an enthalpy of fusion $\Delta_{fus}H$ = (21.5 ± 0.3) kJ mol^{-1} (curve 1, Figure 3.5). There were no other observed events during the heating process, as demonstrated by the thermal microscopy images in Figure 3.6.1.

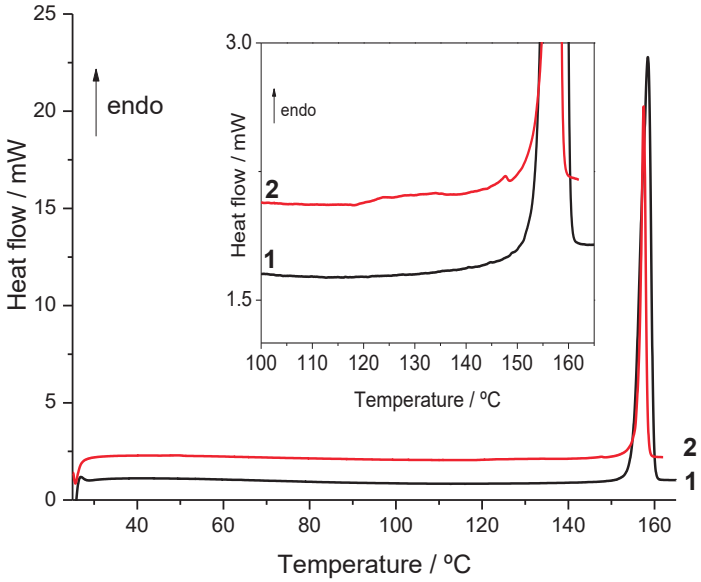

Figure 3.5 1-MH DSC heating curves from 25 ºC to 162 ºC, β = 10 ºC min^{-1}. 1. Original 1-MH substance (polymorph I),[86] mass m = 1.91 mg 2. 1-MH sample obtained by sublimation (at T =100 ºC, p = 103 Pa, cold finger at about 20 ºC, polymorph II), m = 0.79 mg.

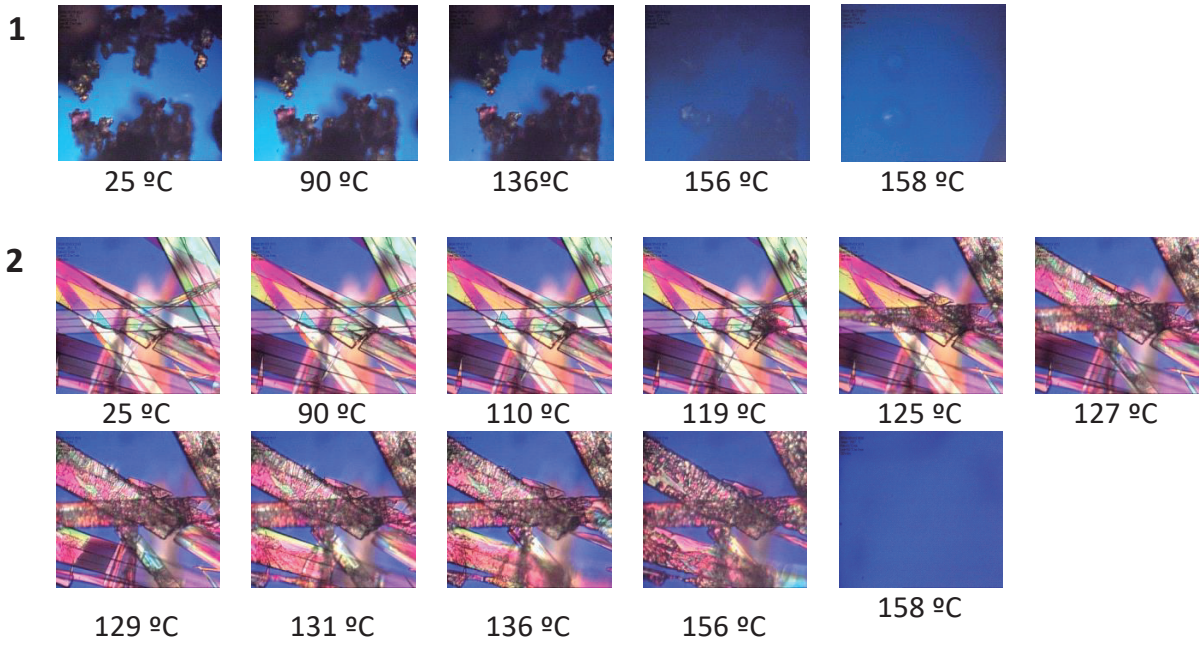

Figure 3.6 Polarized light thermal microscopy images collected in 1-MH heating processes from 25 ºC to 162 ºC, β = 10 ºC min^{-1}, amplification 200x. 1. Original 1-MH substance (polymorph I 2. 1-MH sample obtained by sublimation (at T =100 ºC, p = 103 Pa, cold finger at about 25 ºC), polymorph II.

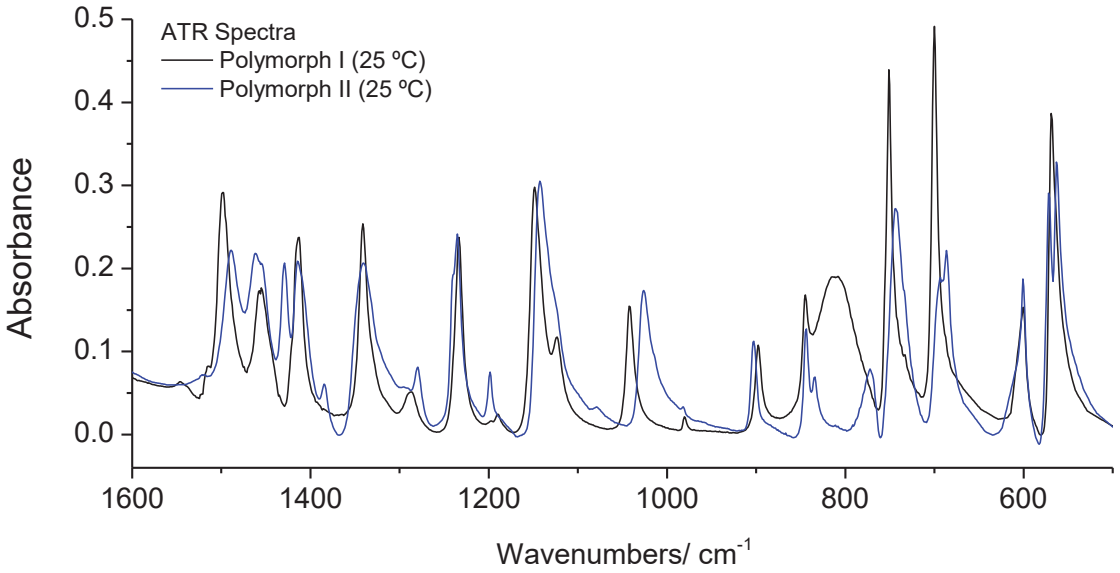

Figure 3.7 1-MH attenuated reflectance IR spectra (1600-500 cm^{-1} range): original 1-MH substance (polymorph I)[86] (black line); 1-MH sample obtained by sublimation (at T =100 ºC, p = 103 Pa, cold finger at about 25 ºC; polymorph II) (blue line).

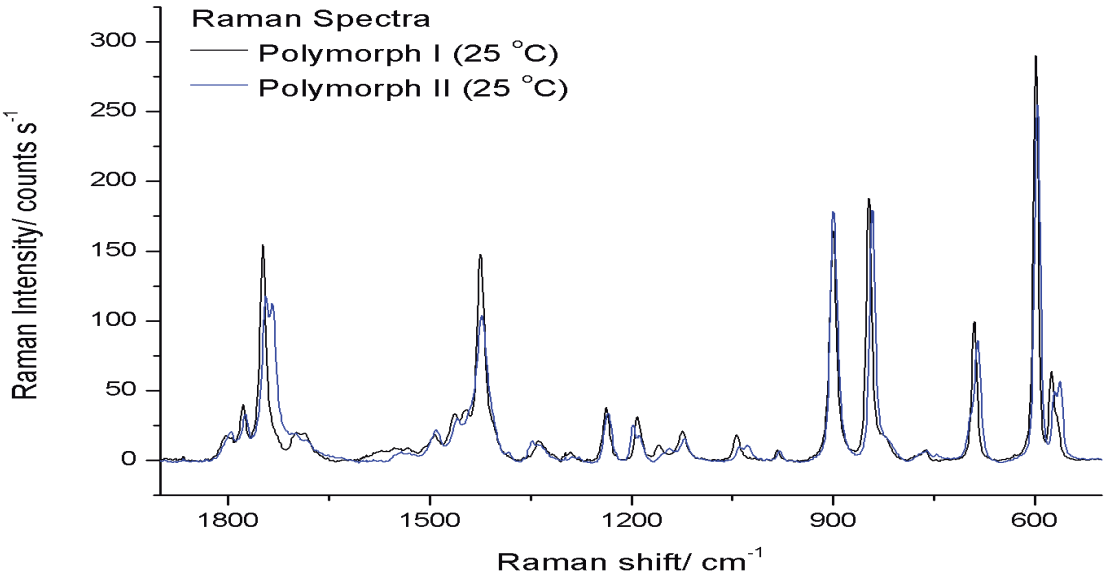

Figure 3.8 1-MH Raman spectra (1900-500 cm^{-1} range): original 1-MH substance (polymorph I)[86] (black line); 1-MH sample obtained by recrystallization in methanol solution (polymorph II) (blue line).

Another 1-MH samples were obtained by: *(a)* sublimation at T = 100 ºC, p =103 Pa, using the cold finger technique, with water at about 20 ºC as the freezing fluid and *(b)* recrystallization from methanol, acetone and tetrahydrofuran (THF) solutions at room temperature. The crystalline structure of these new samples, crystals with uniform acicular habit, differs from that of polymorph I, as supported by the ATR spectra presented in Figure 3.7 (1600-500 cm^{-1} region) and by the Raman spectra shown in Figure 3.8 (1900-500 cm^{-1} region).

Furthermore, when heating the new solid form, II, a low energy solid-solid transition takes place, extending from about 110 ºC to 135 ºC, as evidenced by PLTM images in Figure 3.6.2 and also presented in curve 2 in the inset of Figure 3.5. The solid-solid transition gives rise to polymorph I, as the thermodynamic values obtained for the fusion process are indistinguishable from those of this form. This conclusion is also supported by IR and Raman spectroscopy, as detailed below.

The infrared spectra of both purchased and obtained by recrystallization in methanol samples diluted in KBr pellets were recorded at room temperature (see Figure 39). These spectra are identical to the corresponding ATR spectra shown in Figure 3.7 and, demonstrate that the process of preparation of the KBr pellets did not lead to any structural change in both polymorphs. Then, polymorph II sample was submitted to a temperature program similar to those used in the DSC and thermal microscopy experiments. Figure 3.10 compiles the observed changes in the spectra in two representative spectral regions along the temperature variation experiments. These two spectral regions [showing the bands due to $\gamma(CH_3)'$ (1060-980 cm^{-1}), and δ(C=O7) and δ_2(ring) modes (590-540 cm^{-1}), respectively] were chosen because they are very much sensitive to phase changes, but do not vary much with temperature for a given polymorph, so that phase transitions can be easily detected (on the other hand, the spectral region corresponding to the γ(NH) vibration, between 850 and 600 cm^{-1}, is the most sensitive region to structural changes, but the large shifts with temperature in the same phase makes this region less illustrative to phase transition observations). In the two chosen spectral regions, the two polymorphs have quite diverse vibrational signatures, with polymorph I giving rise to two single bands at 1043 and 571 cm^{-1}, while polymorph II exhibit a single band at 1028 cm^{-1} and a doublet at 572/564 cm^{-1}. In consonance with the DSC and PLTM results, the IR spectroscopy results clearly show that, upon heating, polymorph II converts into polymorph I, which then melts at about 155 ºC, as expected for this polymorph. As shown in Figure 3.10, the spectrum obtained at 155 ºC reveals a still incomplete melting, while the spectrum registered at 165 ºC corresponds to that of liquid 1-MH (see Figure 3.9). Also as in the DSC and PLTM experiments, the solid-solid II→I transition was found to take place in an extended range of temperature. However, the process could be spectroscopically detected to have already started around 95 ºC (see Figure 3.10), a somewhat lower temperature compared to those found in the DSC and PLTM experiments. This may be assigned to the dissimilar experimental conditions in the different experiments.

The band assignments for the room temperature infrared spectra of the two polymorphs of 1-MH and for the matrix-isolated molecule (at 10 K; in argon matrix) are presented in Table 3.17. The comparison of the frequencies of the matrix-isolated compound with the solid 1-MH in the different phases was found to be

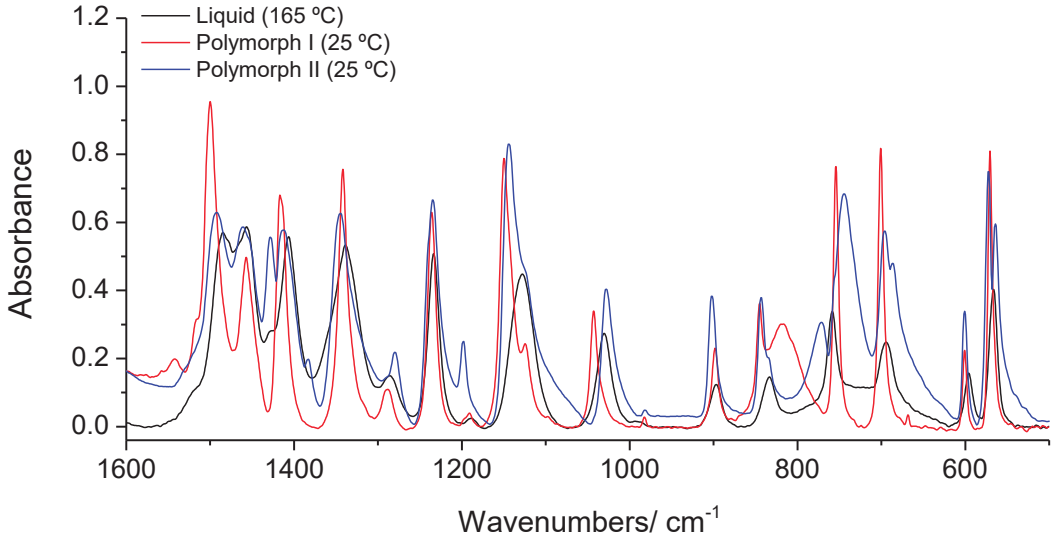

Figure 3.9 Infrared spectra (1600-500 cm^{-1} region) of liquid 1-MH, at 165 ºC (black line), and of the two crystalline polymorphs of the compound at room temperature (25 ºC) (polymorph I, red line; polymorph II, blue line).

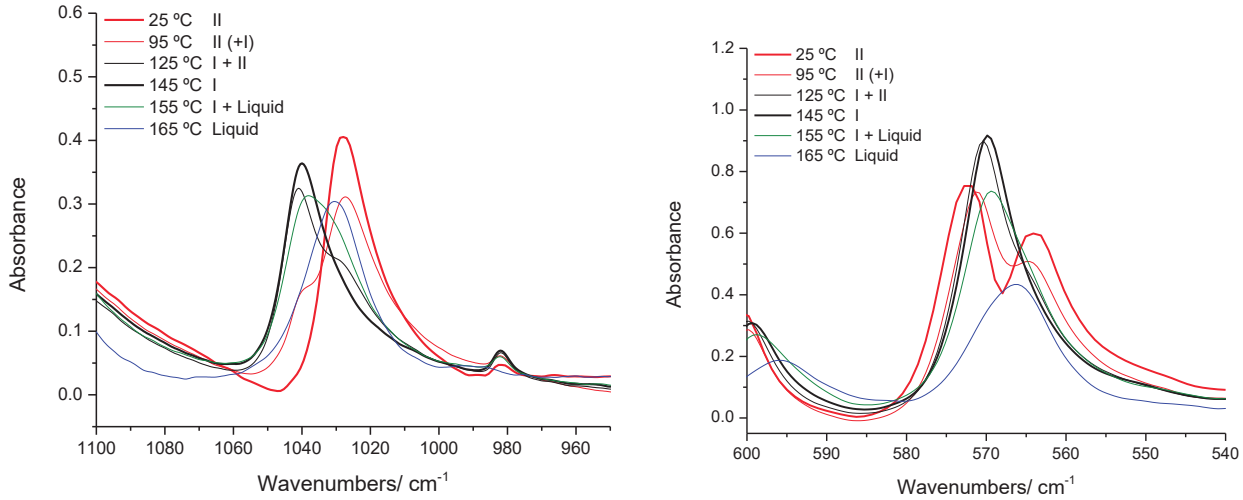

Figure 3.10 Infrared spectra (selected spectral regions) showing the evolution with temperature of a sample of polymorph II of 1-MH.

Table 3.17. Infrared bands (cm^{-1}) of matrix-isolated 1-MH, at -263.15 ºC, and of the two observed polymorphs (I and II) of the compound (in KBr pellet; T = 25 ºC), with assignments.[a]

Ar matrix (-263.15 ºC) Freq[b]	Crystal (25 ºC) Polymorph I Freq[b]	Polymorph II Freq[b]	Assignment[a]
3488/3482	3202/ 3142/ 3045/ 2819/ 2776/ 2744	3257/ 3192/ 3128/ 3072/ 3047/ 2752/ 2723	ν(NH)
n.obs.	2983	2984	$\nu(CH_3)_{as}'$
2962/2960	2957	2952	$\nu(CH_3)_{as}''$
2951	2957	2939	$\nu(CH_2)_a$
2930	2933	2928	$\nu(CH_2)_s$
2927	2886	2886	$\nu(CH_3)_s$
1805/1803	1800/ 1770	1803/ 1770	ν(C=O9)
1771/1768	1748/ 1727/ 1709/ 1688	1751/ 1728/ 1709/ 1687	ν(C=O7)
1505/1492	1516	1517	$\delta(CH_3)_{as}'$
1343/1342/ 1337/1335	1500	1489	δ(NH)
1457/1455	1457	1462	$\delta(CH_3)_{as}''$
1456/1454	1452	1456	$\delta(CH_2)$
1430/1427	1421	1427	$\delta(CH_3)_s$
1413/1412/ 1407/1404/ 1401/1396	1417/1415	1414/ 1383	ν_2(ring)
1319/1316	1342	1343	ν_4(ring) [c]
1295/1292	1289	1291/ 1280	ν(NC)
1237/1235/ 1232	1236	1240/ 1235	$w(CH_2)$
1180/1176	1198/ 1191	1198	$tw(CH_2)$
1131	1125/ 1114	1125	$\gamma(CH_3)''$
1121/1119/ 1116/1112/ 1108	1150/ 1145	1145	ν_1(ring)[c]
1029/1028	1043	1028	$\gamma(CH_3)'$
995/986	983	982	$\gamma(CH_2)$
884/883	898	901	ν_5(ring)
816	845	844/ 835	ν_3(ring)
530/527	817	771	γ(NH)
752	754	745	γ(C=O7)
688	701	700/ 687	δ_1 (ring)
594/591/ 588/586/ 582	601	601	γ(C=O9)
555/554	571 / 571	572 / 564	δ(C=O7) / δ_2 (ring)

[a] See Scheme 3.1 for atom numbering; assignments correspond to approximate descriptions of the vibrations chosen as the main coordinate contributing to the vibration (avoiding repetition) and are based on the PED's obtained for the isolated monomer (see Table 5); abbreviations: w, wagging; tw, twisting; γ, rocking; ν, stretching; δ, bending; τ, torsion; s, symmetric; as, anti-symmetric. [b] Wavenumbers in cm-1; n.obs., not observed; n.i., not investigated. [c] Also with a significant contribution from the δ(NH) coordinate.

particularly useful for identification of the bands associated with the NH hydrogen-bond donor fragment, which were anticipated to be very much sensitive to phase changes (see Section 3.2).

As it is shown in Table 3.17, the spectra of the solid 1-MH phases resemble very well the spectrum collected for the matrix-isolated compound, except for the bands that concern the NH group, which acts as H-bond donor in both polymorphs. This result indicates that the prevalent hydrogen intermolecular bonding does not perturb extensively the intramolecular potential, except for the NH donor moiety, for which pronounced effects of the hydrogen bonding interactions are distinctly visible in the spectra. In the *ν*(NH) stretching region, the expected and usual frequency downshift is observed and in the case of NH bending modes (in plane bending, *δ*(NH), and out-of-plane rocking, *γ*(NH)) it is evident the predicted frequency shift to higher wavenumbers.[114,115]

These observed frequency shifts in the *ν*(NH) and *γ*(NH) bands upon hydrogen bond formation are particularly relevant, since the shift of the first mode to lower frequencies and of the later to higher wavenumbers are correlated, because both parameters correlate with hydrogen bond energy.[114,115] The empirical correlation has the form $\Delta\nu_{\gamma(NH)}{}^2 = 2.5\left(\left|\Delta\nu_{\gamma(NH)}\right|\right)^{1/2} - 18$, where $\Delta\nu_{\gamma(NH)}{}^2 = \left(10^{-2}\nu_{H\gamma(NH)}\right)^2 - \left(10^{-2}\nu_{0\gamma(NH)}\right)^2$, and $\Delta\nu_{\nu(NH)} = \nu_{H\nu(NH)} - \nu_{0\nu(NH)}$, the subscripts *H* and *0* referring to hydrogen bonded and free molecules, respectively, and the frequencies are expressed in cm^{-1}. For 1-MH, the application of this empirical correlation using the *ν*(NH) frequency of the matrix-isolated compound as reference, led to estimated frequencies for *γ*(NH) of 821 and 808 cm^{-1} for polymorph I and polymorph II at room temperature, which are in good agreement with the experimental values: 817 and 771 cm^{-1} (Table 3.17). Interestingly, for 1-methylhydantoin the correlation seems to apply also when the *δ*(NH) in-plane bending mode is considered instead of the out-of-plane *γ*(NH) rocking mode. In this case, the estimated frequency values obtained using the empirical correlation are 1479 and 1472 cm^{-1}, which also are in good agreement with the corresponding observed values presented in Table 3.14: 1500 and 1489 cm^{-1}.

From the observed shifts in NH frequencies upon H-bonding an estimation of the hydrogen bond energies can also be obtained. The H-bond energy (in kJ mol^{-1}) and the shifts (in cm^{-1}) in the ν(NH) and γ(NH) bands were shown to obey (to within 10%) the empirical correlations, $(\Delta H)^2 = 1.92[\Delta\nu_{\nu(NH)} - 40]$, and $-\Delta H = 0.67\times10^4 \times \Delta\nu_{\gamma(NH)}{}^2$. Using these relationships, the average energies of the H-bonds present in both polymorphs of 1-MH at room temperature (25 ºC) were estimated as equal to ca. −28 and −26 kJ mol^{-1}, for polymorph I and II, respectively, *i.e.*, H-bond networks in the two polymorphs were estimated to have similar strengths. Nevertheless, though the difference between these two values is of the same order of magnitude as the uncertainty of the empirical correlation in determining absolute H-bond enthalpy values (and then cannot be taken quantitatively), the results point to an average slightly stronger H-bond network in polymorph I, which is in fact confirmed by the analysis of the X-ray data as we will see later in Section 3.6.

A similar temperature program of those used in DSC, thermal microscopy and IR-temperature variation experiments, was performed for a sample of 1-MH polymorph II in the Raman microspectrometer.

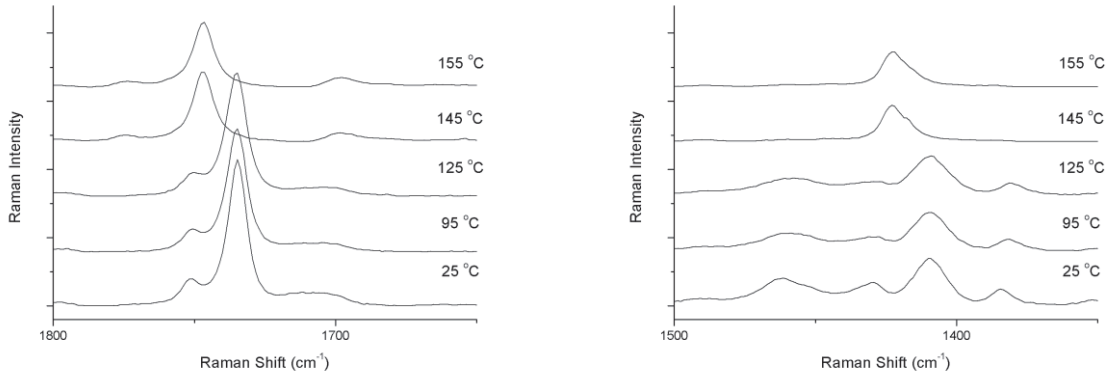

Figure 3.11 Raman spectra (selected spectral regions) showing the evolution with temperature of a sample of polymorph II of 1-MH.

The evolution of the Raman spectra along temperature variation in two representative spectral regions is presented in Figure 3.11.

In consonance with the DSC, thermal microscopy and IR spectroscopy results, the temperature variation-Raman results clearly show a conversion of polymorph II into polymorph I at a temperature between 125 and 145 ºC. In Figure 3.11, the shifts of the $\nu(C{=}O)_{as}$ and the $\delta(CH_3)$ modes from 1735 and 1409 cm^{-1} to 1747 and 1423 cm^{-1}, respectively, as a result of the solid-solid transition between polymorph II into polymorph I that occurred during the heating process are shown for illustration (these differences in both spectra are also visible in Figure 3.8).

3.5.2 5-methylhydantoin

The purchased sample of 5-MH, from now on named as polymorph I, was studied and characterized by infrared and Raman spectroscopies (the infrared spectrum is shown in Figure 3.12 and the Raman spectrum in Figure 3.13). The infrared spectrum of the compound shows a large frequency downshift of the stretching ν(NH) vibrations compared with the spectrum of 5-MH in the argon matrix. The bands corresponding to NH stretching modes appear at 3314 and 3140 cm^{-1} in the solid state spectrum (see Figure 3.12), while in the spectrum of the monomeric isolated the same bands are observed at 3510/3499 and 3491/3487/3481 cm^{-1} (see Figure 3.2 and Table 3.13).

According to the performed DSC studies, the melting of the 5-MH polymorph I occurs at T_{fus} = (147.2 ± 0.6) ºC with an enthalpy of fusion of $\Delta_{fus}H$ = (17.2 ± 0.2) kJ mol^{-1} (curve 1, Figure 3.14). As also proven by

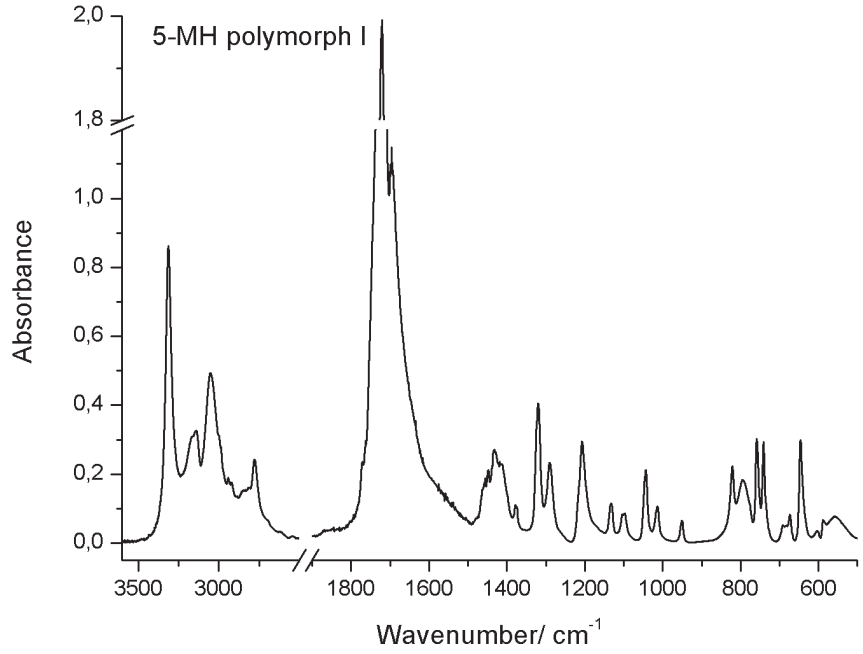

Figure 3.12 Attenuated reflectance IR spectrum of 5-MH commercial sample (polymorph I).

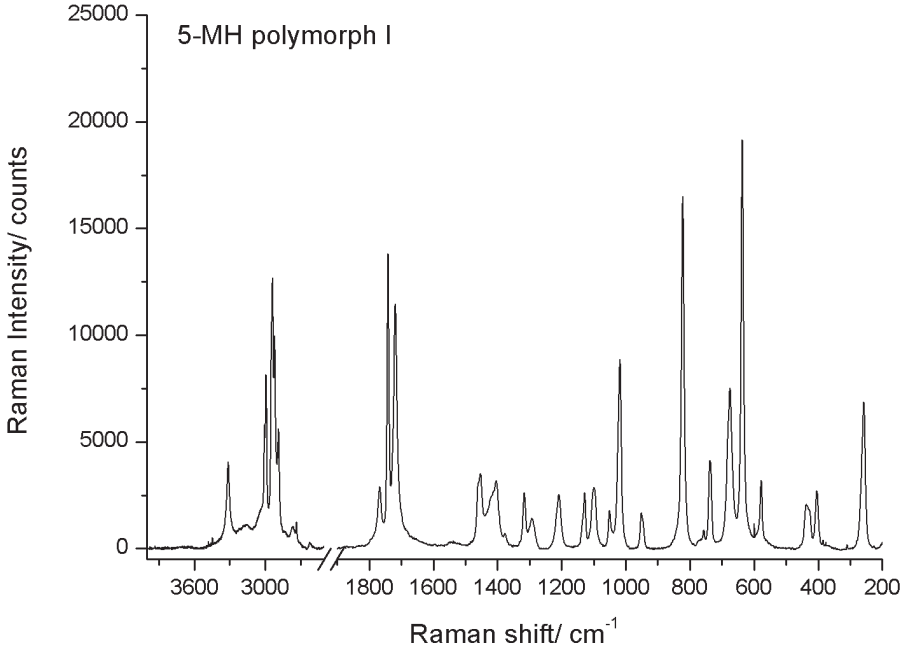

Figure 3.13 Raman spectrum of 5-MH commercial sample (polymorph I).

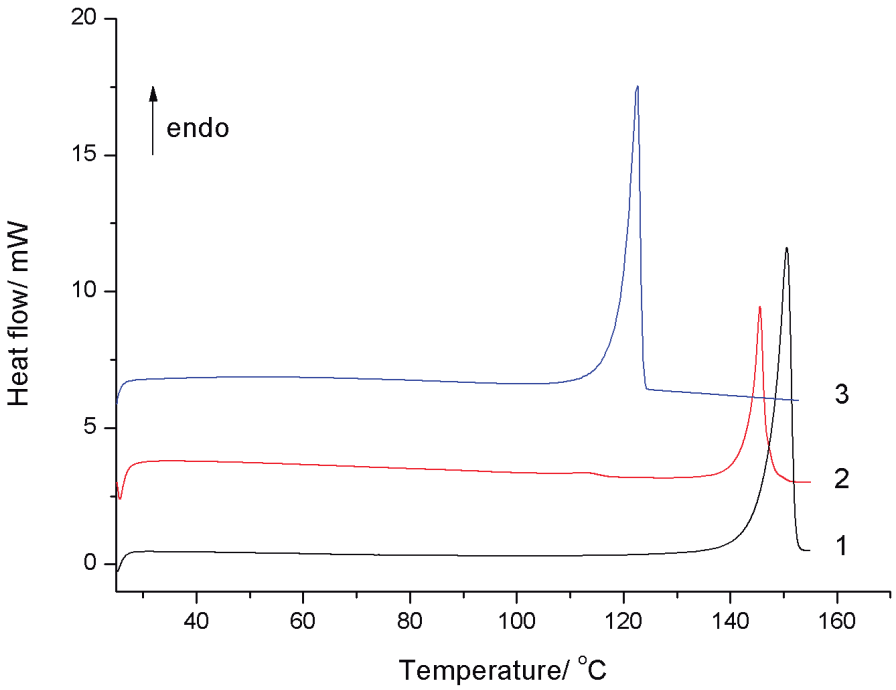

Figure.1.14 5-MH DSC heating curves from 25 to 155 ºC, β = 10 ºC min^{-1}. (1) Original 5-MH substance (polymorph I), mass= 1.76 mg. (2) 5-MH sample obtained by recrystallization in THF solution (polymorph II),), mass= 1.18 mg. (3) 5-MH sample obtain by recrystallization of the melted original sample (polymorph III)), mass= 1.97 mg.

polarized light thermal microscopy (Figure 3.15, part 1) no further events were observed during the heating process of polymorph I, besides the described melting of the sample.

By differential scanning calorimetry it was possible to identify another polymorph (polymorph II) of 5-MH. This polymorph II was obtained by recrystallization of 5-MH from a THF solution, which originated a heterogenic polymorphic mixture of crystals, and also by recrystallization of the melted compound, followed by heating. Two solid-solid transitions take place (as it is shown in the polarized light thermal microscopy images, Figure 3.15, part 2), after which polymorph II is formed. The melting of polymorph II occurs at T_{fus} = (143.0 ± 0.4) ºC with an enthalpy of fusion of $\Delta_{fus}H$ = (12.0 ± 0.2) kJ mol^{-1}, according to the performed DSC studies (Figure 3.14, curve 2). The later solid-solid transition that originates polymorph II, occurs at ca. 115-118 ºC, according to the PLTM studies (part 2, Figure 3.15). The polymorphic form of 5-MH before this transition is a new polymorph (polymorph III), which was also possible to identify in the DSC experiments (curve 3, Figure 3.14). This polymorph has a melting point of T_{fus} = (120.1 ± 0.8) ºC and an enthalpy of fusion of $\Delta_{fus}H$ = (13.1 ± 0.1) kJ mol^{-1}. It was also possible to obtain polymorph III by recrystallization of the liquid compound, when heated at ca. 107 ºC, as shown in part 3 of Figure 3.15.

1

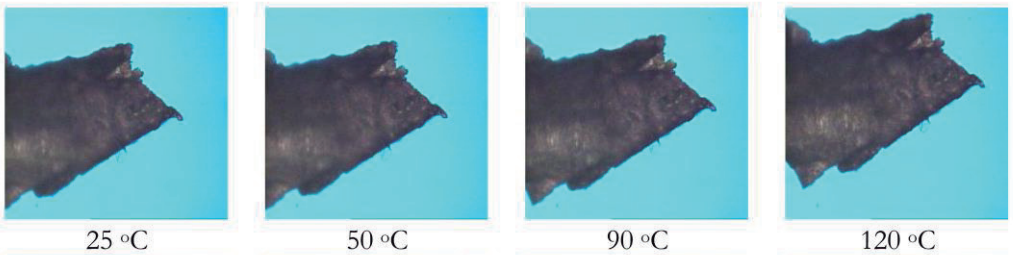

25 °C | 50 °C | 90 °C | 120 °C

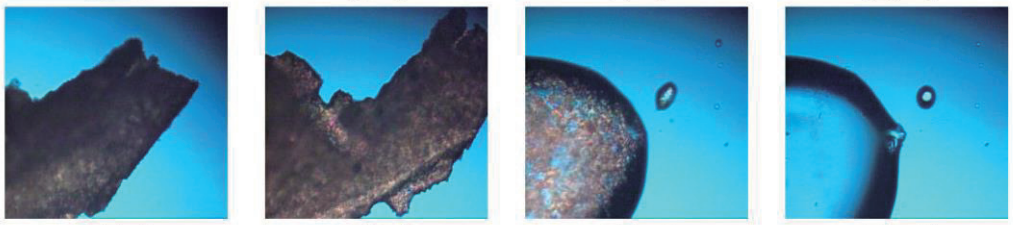

146 °C | 148 °C | 150 °C | 152 °C

2

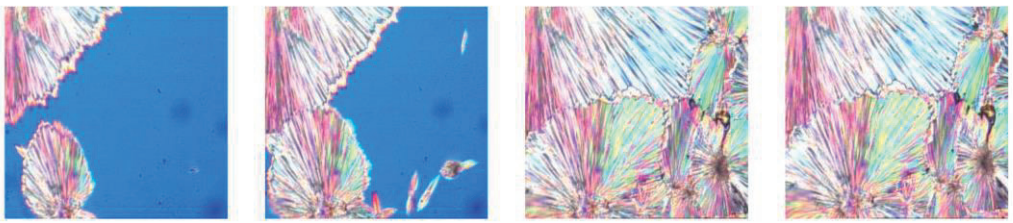

25 °C | 40 °C | 50 °C | 80 °C

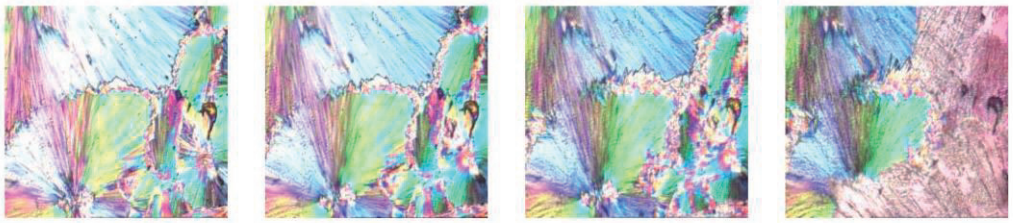

90 °C | 100 °C | 112 °C | 117 °C

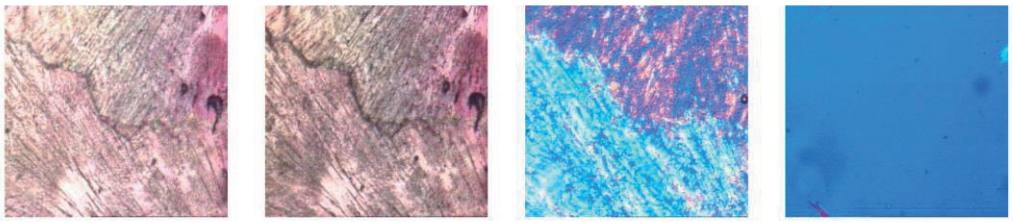

120 °C | 130 °C | 146 °C | 147 °C

3

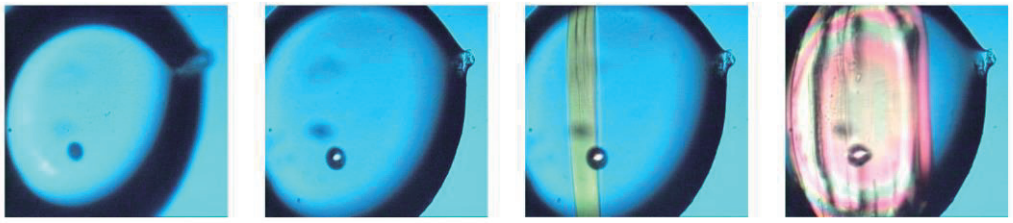

95 °C | 106 °C | 107 °C | 111 °C

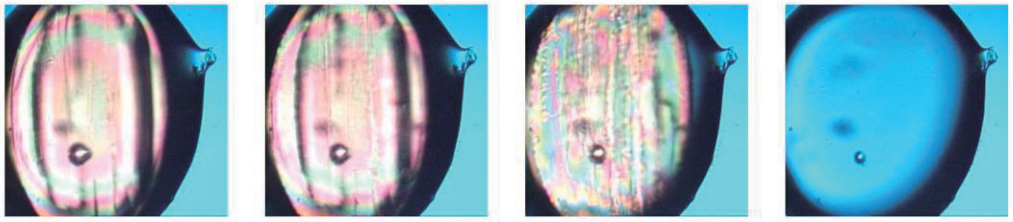

114 °C | 119 °C | 120 °C | 124 °C

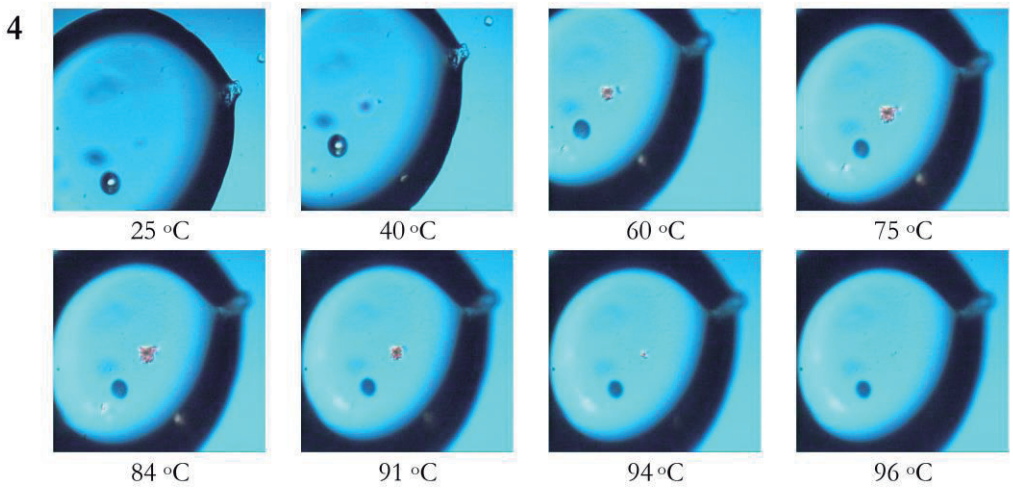

Figure 3.15 Polarized light thermal microscopy images collected in 5-MH heating process from 25 ºC to 155 ºC, β = 10 ºC min^{-1}, amplification 200x. (1) Melting of the commercial 5-MH substance (polymorph I) (2) 5-MH sample obtained by recrystallization of the melted compound and melting of polymorph II (3) 5-MH sample obtained by recrystallization of the melted compound and melting of polymorph III (4) 5-MH sample obtained by recrystallization of the melted compound and melting of polymorph IV.

In the PLTM experiments, it was possible to found an additional crystallographic form of 5-MH (polymorph IV). When cooling the melted compound, the liquid starts to crystallize at ca. 40-44 ºC. The crystal growth is interrupted at temperatures lower than 30 ºC, once the motion of the molecules is obstructed by the higher viscosity of the liquid at lower temperatures. As the sample is heated again, at temperatures higher than 32-36 ºC, the crystals start to grow again and the new polymorph, IV, converts to polymorph III in a very slow and gradual solid-solid transition that starts at 60 ºC and lasts for ca. 40 ºC (third to seventh image of part 2, Figure 3.14) or melts at ca. 94-96 ºC (part 4, Figure 3.15).

Polymorph IV was not possible to identify in the DSC studies, either because we were not able to generate it in such conditions, or because the solid-solid transition is imperceptible in this technique, as the range of temperature that it last is too broad. Nevertheless, we could characterize this polymorph, as well as all the other three polymorphic forms, by Raman spectroscopy, as shown in Figure 3.16.

The Raman spectra of polymorphs I and II are essentially the same, except for a small band appearing at 492 cm^{-1} in the spectrum of polymorph II. This means that the orientation of the 5-MH molecules in both crystals is very similar. Another not so evident difference is the ratio between the carbonyl intensities to the bands due to the N-H stretching vibrations, which is higher for the case of polymorph II. The Raman spectrum of polymorph III presents more clear differences compared to those of polymorphs I and II, specifically in the C=O stretching region, with the first two polymorphs having a single band at 1768 cm^{-1} and a site-split doublet at 1742/1721 cm^{-1} and polymorph III giving rise to two bands at 1752 and 1701 cm^{-1}, assignable to the symmetric and anti-symmetric carbonyl stretching vibrations. This difference suggests a significant difference in the H-bonding of polymorph III compared to polymorphs I and II. The Raman

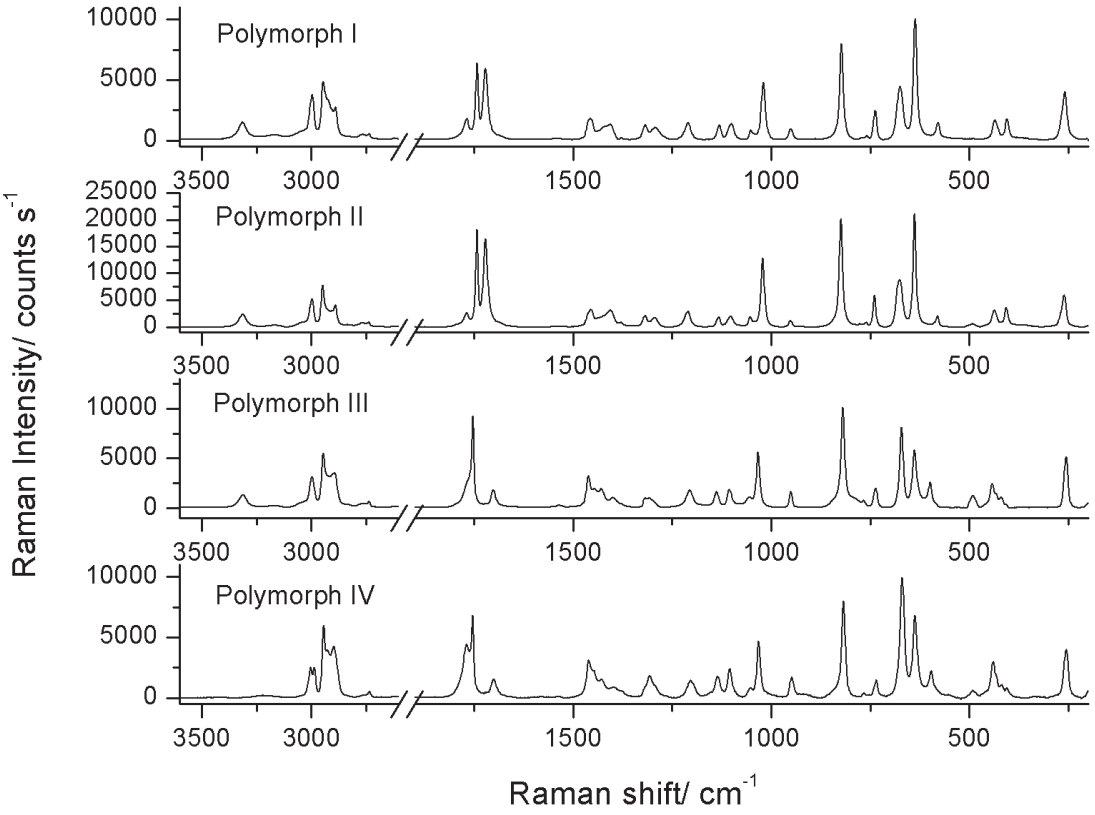

Figure 3.16 Raman spectra of the four different polymorphs of 5-MH.

spectrum of polymorph IV is quite similar to that of polymorph III, with two significant differences: *(a)* the appearance of a site-split doublet for the symmetric stretching carbonyl vibration, at 1769/1753 cm^{-1} and *(b)* a broader, less intense and shifted to lower frequencies band in the N-H stretching region. Both differences point out to a difference in the hydrogen bonding of these two polymorphs but, nonetheless, the other vibrations are not significantly affected by these different intermolecular interactions, so that the structure of these two polymorphic variations shall also present a light degree of similarity.

3.5.3 5-hydantoin acetic acid

The 5-HAA commercial sample, labeled as polymorph I, was characterized by infrared and Raman spectroscopies (Figures 3.17 and 3.18, respectively) and it was also studied by differential scanning calorimetry and by polarized light thermal microscopy (Figures 3.19 and 3.20 – part 1, respectively). The infrared spectrum shows the already discussed (see Section 3.3) frequency downshift of the stretching ν(NH)

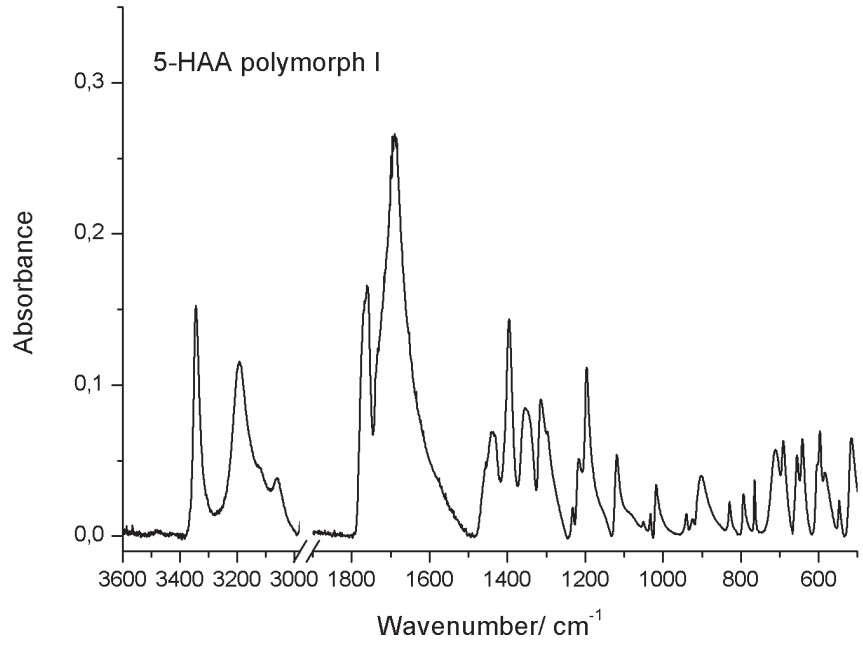

Figure 3.17 Attenuated reflectance IR spectrum of 5-HAA commercial sample (polymorph I).

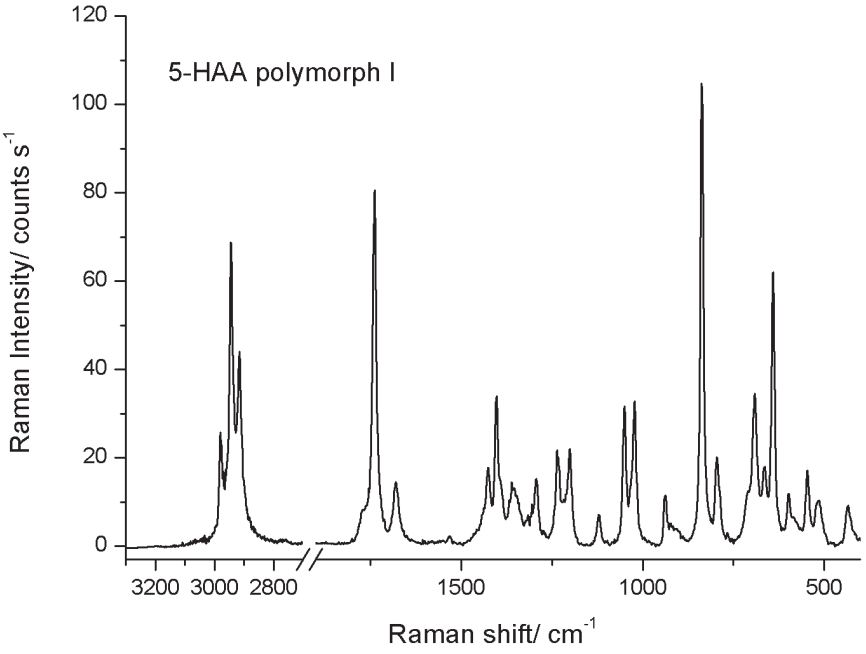

Figure 3.18 Raman spectrum of 5-HAA commercial sample (polymorph I).

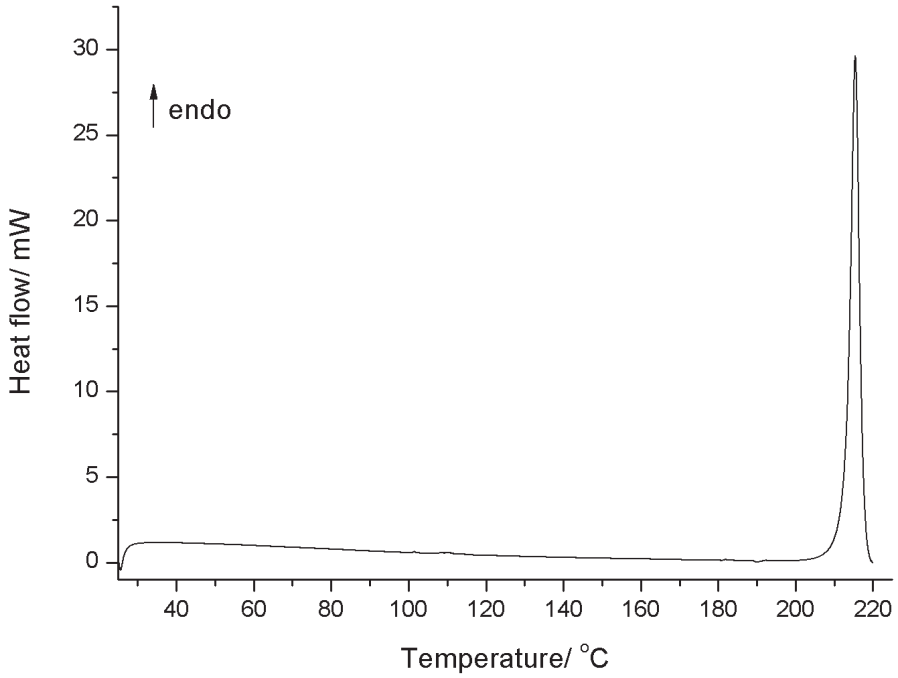

Figure 3.19 DSC heating curve from 25 to 222 ºC, β = 10 ºC min^{-1} of original 5-HAA substance (polymorph I), mass= 1.61 mg.

vibration in the neat solid state to 3345 and 3194 cm^{-1}, comparing with the spectrum of the monomeric isolated compound, where the same bands appear at 3485 and 3194 (see Figure 3.3 and Table 3.15).

According to the performed DSC studies, the melting point of polymorph I occurs at T_{fus} = (214.3 ± 0.8) ºC with an enthalpy of fusion of $\Delta_{fus}H$ = (37.0 ± 1.5) kJ mol^{-1}. Besides the melting of the sample, no other events were observed during the heating of the compound, as it is also proven by the thermal microscopy images (Figure 3.20, part 1). In part 2 of Figure 3.20, it is possible to see the clear degradation of 5-HAA immediately after the melting point. For that reason, it was not possible to study the polymorphism of the compound by recrystallization of the liquid. Nevertheless, it was possible to found other polymorphic forms of 5-HAA *via* recrystallization from THF and 1,4-dioxane solutions, which led to heterogenic polymorphic mixtures of polymorphs I, II and III, in the first case, and I and IV in the later. The melting of these new polymorphs is shown in the PLTM images to occur at ca. 184-185 ºC, for polymorph II (part 2, Figure 3.19), at ca. 175-178 ºC for polymorph III (part 3, Figure 3.19), and at ca. 198-200 ºC for polymorph V, which results from a solid-solid transition (at ca. 180-185 ºC) of polymorph IV. Polymorphs II, III and IV were also characterized by Raman spectroscopy (Figure 3.20), but it was not possible to isolate polymorph V to be characterized spectroscopically.

One of the major differences between the Raman spectra of the four polymorphs accessed by Raman spectroscopy is the different position of the maximum of the anti-symmetric C=O stretching band (1738,

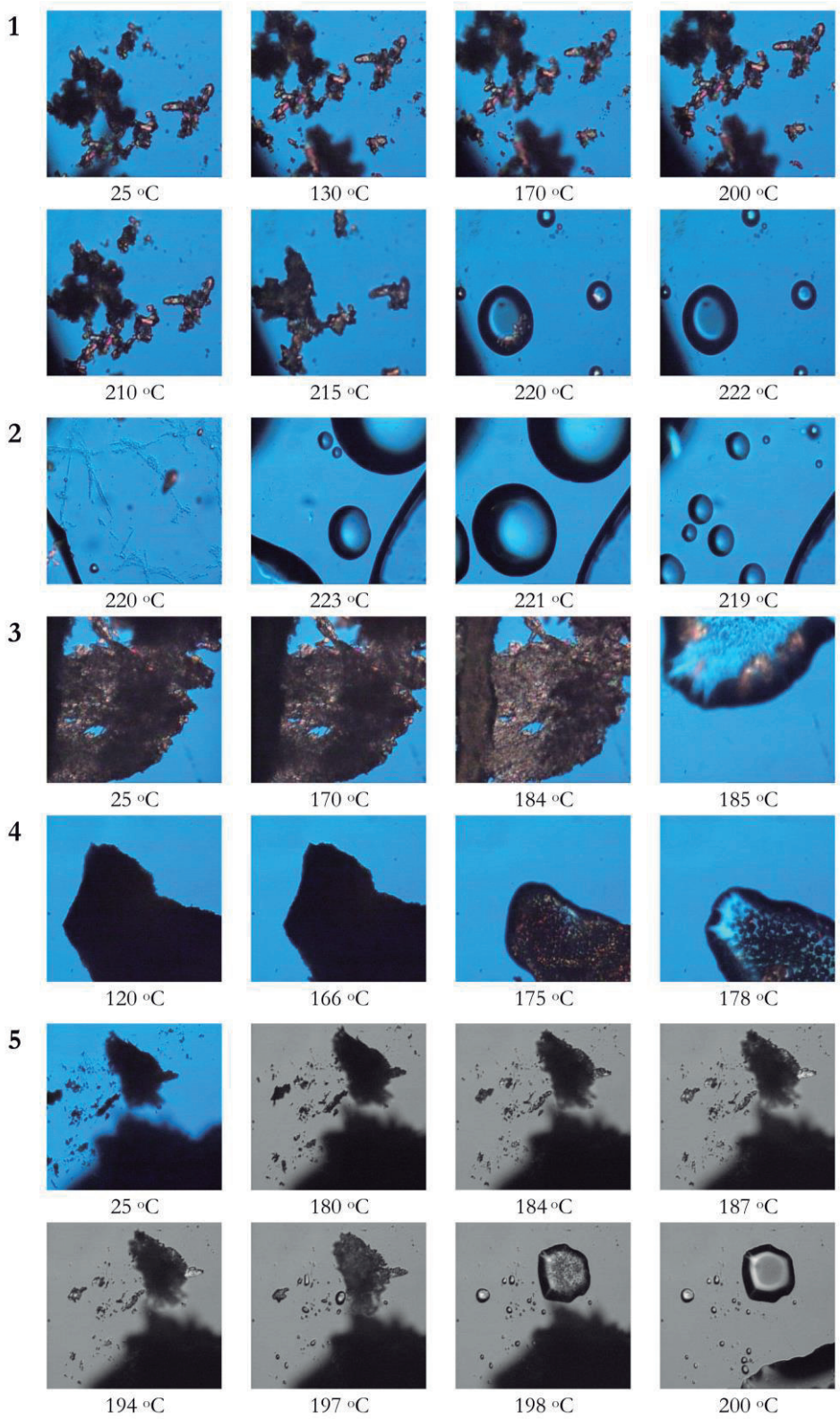

Figure 3.20 Polarized light thermal microscopy images collected in 5-HAA heating process from 25 ºC to 224 ºC, β = 10 ºC min^{-1}, amplification 200x.(1) Melting of the commercial 5-HAA substance (polymorph I) (2) 5-HAA liquid sample degradation (3) 5-HAA sample obtained by recrystallization in a THF solution and melting of polymorph II (4) 5-HAA sample obtained by recrystallization in a THF solution and melting of polymorph III (5) 5-HAA sample obtained by recrystallization in a 1,4-dioxane solution and melting of polymorph IV.

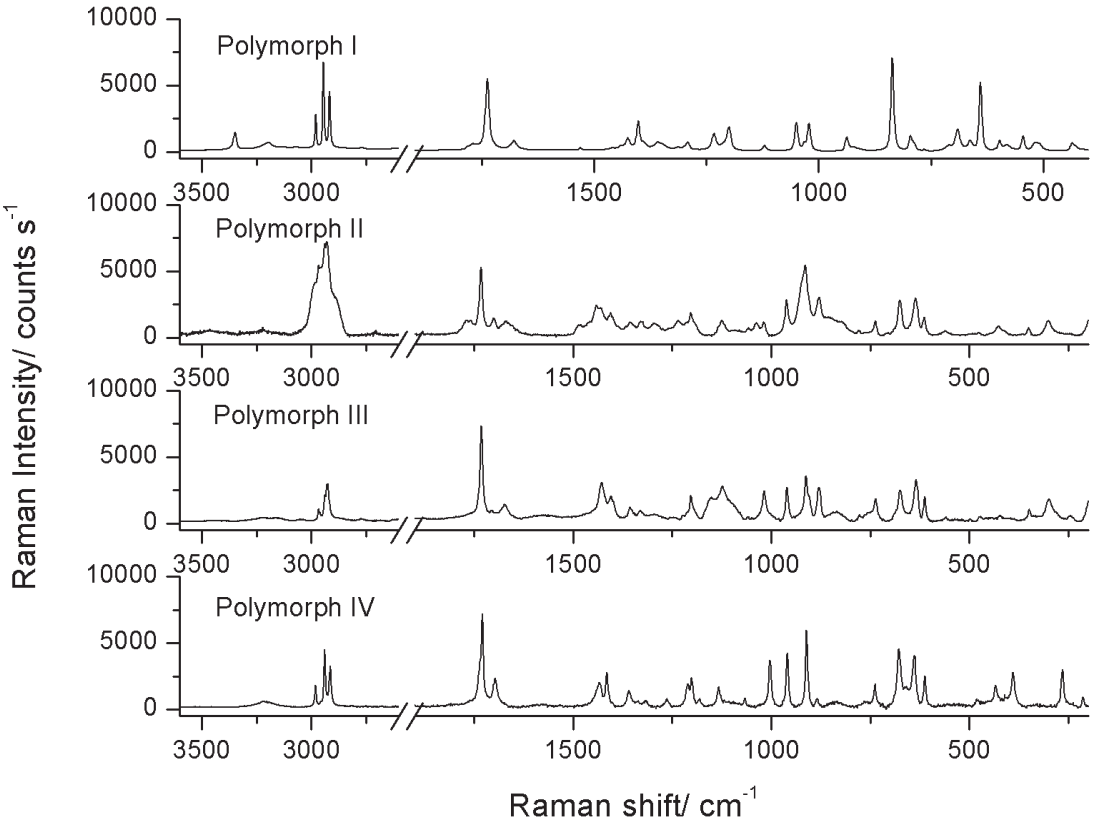

Figure 3.21 Raman spectra of the four different polymorphs of 5-HAA.

1733, 1731 and 1729 cm^{-1} for polymorphs I, II, III and IV respectively). The CH stretching region (3100-2800 cm^{-1}) shows also remarkably different features in the spectra of the different polymorphs, with the spectra of polymorphs I and IV being very similar in this region, only with a minor frequency downshift shown by the bands of polymorph IV in this region. On the other hand, the spectra of polymorphs II and III are completely different from each other and also from the spectra of the other two polymorphs (see Figure 3.21).

3.6 X-ray analysis and hydrogen bonding in 1-MH

Note: Due to longstanding problems with the diffractometer used in the single crystal X-ray measurements, it was not possible to carry out experiments for 5-MH and 5-HAA, though we were able to produce suitable

Table 3.18. Crystallographic parameters for the two polymorphs of 1-MH .

Unit cell dimensions	Polymorph I	Polymorph II
a (Å)	5.601(10)	19.0258(4)
b (Å)	12.178(3)	3.91210(10)
c (Å)	8.090(2)	6.82880(10)
α (°)	90	90
β (°)	105.62(2)	90
γ (°)	90	90
Volume (Å^3)	531.4(2)	508.273(18)
Z	4	4
D_{calc} (g cm^{-3})	1.426	1.491
Absorption coefficient (mm^{-1})	0.116	0.121
F (0 0 0)	240	240

single crystals for most of the polymorphs. Nevertheless, once these problems with the diffractometer are resolved, we expect to continue this investigation, in order to correlate the differences in the spectra of the different polymorphs of 5-MH and 5-HAA with their crystalline structures and the way they are obtained, namely, the use of different solvents in the recrystallization processes.

As mentioned in Section 3.5.1, two polymorphs of 1-MH were identified, one corresponding to the purchased sample, and a second one (polymorph II) obtained by sublimation at T = 100 ºC, p =103 Pa, using the cold finger technique, with water at about 20 ºC as the freezing fluid, as well as upon crystallization from methanol acetone and THF solutions (the methanol solution gave rise only to polymorph II and the last two solutions gave rise to a mixture of both polymorphs, polymorph I being the major component). Crystals of the two polymorphs suitable for structure determination were collected from samples and investigated by single crystal X-ray diffraction. The results obtained for the crystal of polymorph I replicated those previously reported in the literature.[86] The crystal is monoclinic, $C2/c$; Z = 4, a = 5.601(10) Å , b = 12.178(3) Å,

Table 3.19. Hydrogen bond parameters for the two polymorphs of 1-MH.

Hydrogen bond D-H··A	Distance DH (Å)	Distance HA (Å)	Distance DA (Å)	Angle DHA (°)
		Polymorph I		
N3-H8··O7	0.93(2)	1.888(19)	2.8148(17)	173.5(16)
C6-H14··O9	0.7(1)	2.75(3)	3.450(2)	136(2)
C5-H10··O7	0.973(18)	2.598(19)	3.455(2)	147.2
		Polymorph II		
N3-H8··O7	0.80(3)	2.02(3)	2.816(2)	172(3)
C5-H10··O9	0.97	2.64	3.371(2)	132.9
C5-H11··O9	0.97	2.52	3.395(2)	149.5
C6-H13··O7	0.95(3)	2.50(3)	3.381(3)	155(3)

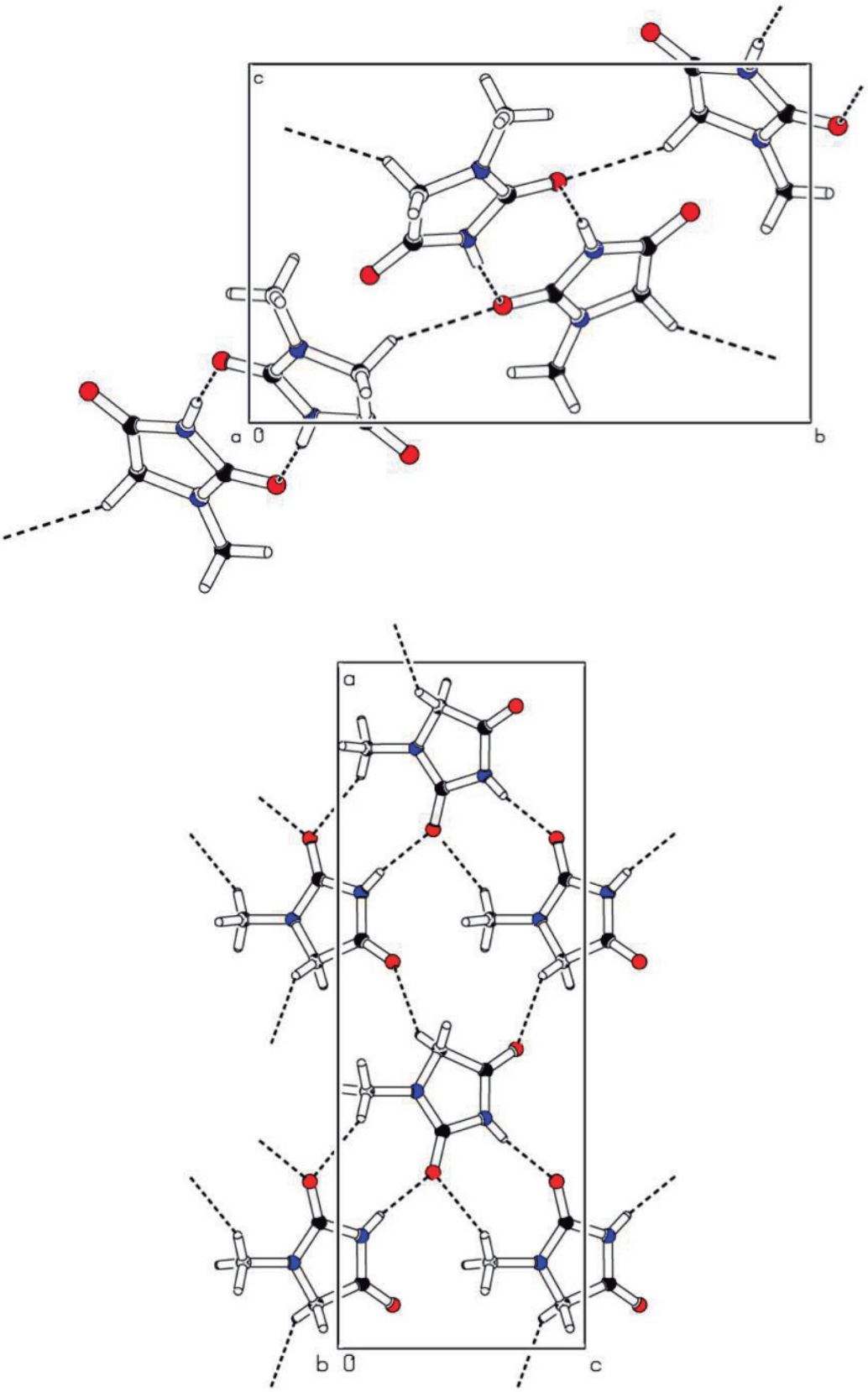

Figure 3.22 Crystallographic unit cell of the two polymorphs of 1-MH (Top: polymorph I; bottom: polymorph II).

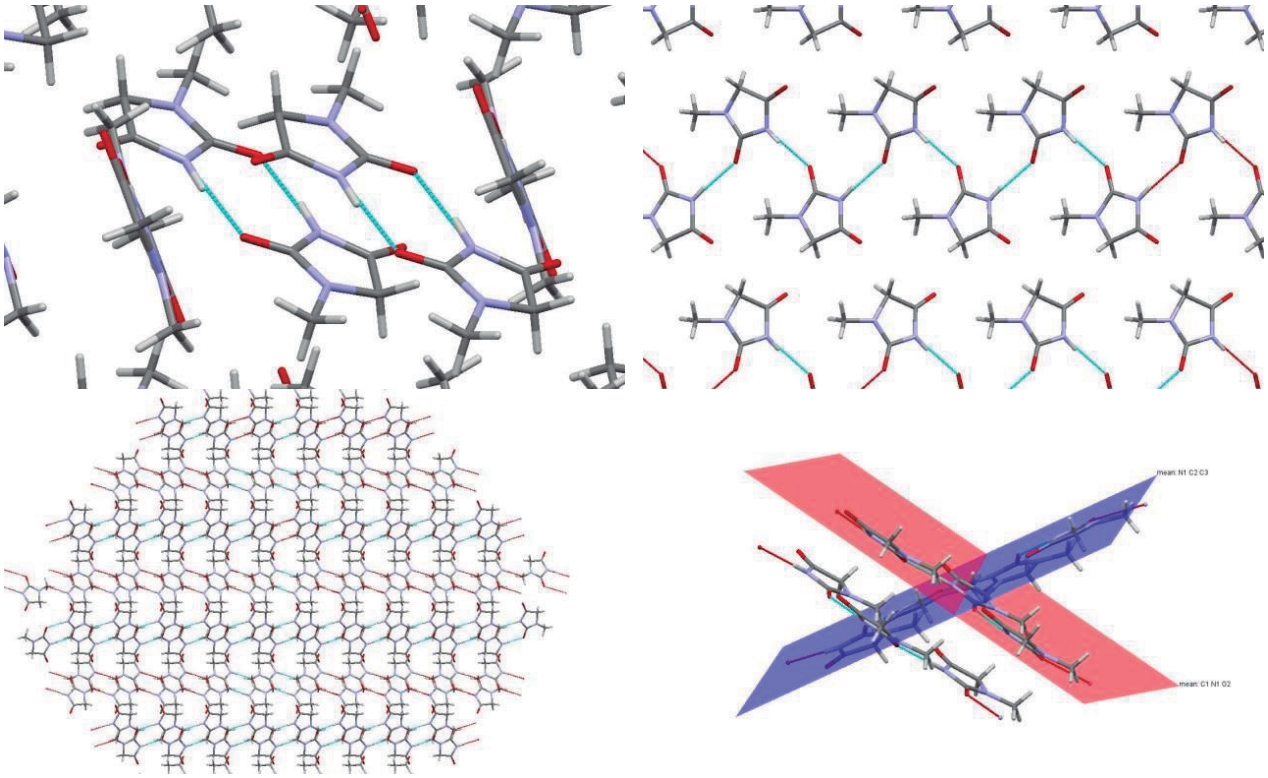

Figure 3.23 H-bonding schemes for the two polymorphs of 1-MH (N3-H8··O7 bond shown). Left: polymorph I; right: polymorph II.

c = 8.090(2) Å, $\alpha = \gamma = 90^{\circ}$ and $\beta = 105.62(2)^{\circ}$ (crystallographic parameters presented in Table 3.18). 1-MH molecules are linked by N-H···O strong hydrogen bonds, forming an eight member centrosymmetric ring $R_2^2(8)$, and by non-conventional C-O···H hydrogen bonds C6-H14···O9 and C5-H10···O7 atoms (see table 3.19 and Figure 3.22). An interesting result regarding the crystallographic study of polymorph I of 1-MH is that the O9 atom does not participate in any classic hydrogen bond, participating exclusively in a non-conventional C-H···O H-bond with the C6-H14 group.

This non-conventional hydrogen bonds act as positional stabilizers between the 1-MH dimers that are formed with the stronger conventional H-bonds (see Figures 3.22 and 3.23). These latter, not only have short donor-acceptor distances but also have donor-hydrogen-acceptor (DHA) angles closer to 180º (see Table 3.19). The combination of the three hydrogen bonds presented in Table 3.19, and the sp^3 hybridization of the C5 atom, generates an undulated pattern of parallel planes (see Figure 3.23).

Polymorph II, whose crystallographic structure has been determined here for the first time, is orthorhombic, *C*2/*c*; *Z* = 4, a = 19.0258(4) Å , b = 3.91210(10) Å, c = 6.82880(10) Å. The 1-MH molecules are linked by a N-H···O strong hydrogen bond, the same as in polymorph I, but also by three non-conventional and weaker C-H···O H-bonds (see Table 3.19 and Figure 3.22). Each molecule participates in two asymmetric nine member ring formed by a classic N-H···O interaction and by a non-classic C-H···O interaction (see Figure

3.22). The other two non-conventional C-H···O bonds take part in a larger 14 member ring composed by four different 1-MH molecules, together with the previous two discussed H-bonds (see Figure 3.22).
In polymorph II, the molecules form a pattern of several zigzag chains which are interspersed with other chains forming an angle of ca. 36° (see Figure 3.23 – bottom right image).
The crystallographic data concerning H-bonding confirm our previous proposition in relation to the relative strength of the H-bonds associated with the NH fragment (as donor) in the two polymorphs, which has been extracted based on simple empirical correlations between the observed NH frequency shifts (for both the ν(NH) and γ(NH) modes) in going from the isolated molecule to the crystalline forms and the H-bond enthalpies (see Section 3.4.1). The estimations obtained from the empirical correlations, for the room temperature crystals, suggested slightly stronger N-H bonds in polymorph I than in polymorph II (-28 and -26 kJ mol^{-1}, respectively). Accordingly, the data shown in Table 3.19 reveal that the donor-acceptor H-bond distance (N3-H8··O7) is indeed slightly shorter and the H-bond angle closer to linearity in polymorph I than in polymorph II, which favors the strength of the bonding.

3.7 Metal complexes with 1-MH

In order to expand the available knowledge on 1-MH complexation to a metal, different aqueous solutions of 1-MH were prepared and mixed with the salt of the metal of interest. The metal ions chosen for this study were Mg (II), Fe (II) and Cu (I), since they are a hard, a borderline and a soft Lewis acid, respectively. The aim of this synthesis was to investigate how these different metal ions can interact with 1-MH and, if they bound, how are the structures of the coordination complexes.
Though it was not possible to determine yet the structure of the different obtained crystals by single crystal X-ray diffraction and compare these results with the results of other 1-MH metallic complexes already published, we were able to characterize these three different crystals by Raman spectroscopy. The spectra of the complexes are compared with that of the commercial sample of the free ligand (polymorph I) in Figure 3.24.
The Raman spectra of the three new coordination complexes are, as expected, quite similar to the spectrum of the free ligand. However, there are some new bands appearing in the spectra of the complexes which are related with the coordination bonds between the central metal ion and the ligand. In the spectra of the Mg(II)·1-MH complex, a new band appears at 397 cm^{-1}, possibly corresponding to the ν(Mg-O) stretching vibration.[116,117] The spectrum of the Fe(II)·1-MH complex presents a new peak at 332 cm^{-1}, that might results from the new Fe-N bond generated by complexation.[118] In the Cu(I)·1-MH complex, a new peak is observed at 253 cm^{-1}, which can be explained by the new Cu-N bond of the complex, whose stretching mode is expected to appear in this spectral region.[119,120]

These results are in agreement with the HSAB theory[121,122], once the hard Mg^{2+} acid binds with the hard base C=O and the soft acid Cu^{+} binds with the softer deprotonated nitrogen. According to the same theory, Fe(II) belongs to a large group of metal ions exhibiting a borderline hardness, and for that reason could eventually bind both with the hard acid C=O and with the softer deprotonated nitrogen, though in the Raman spectra of the Fe(II)·1-MH complex only the band ascribable to the Fe-N stretching vibration could be identified. This result suggests that in the present complex the Fe^{2+} ion is only bound to the N3 atom of 1-MH.

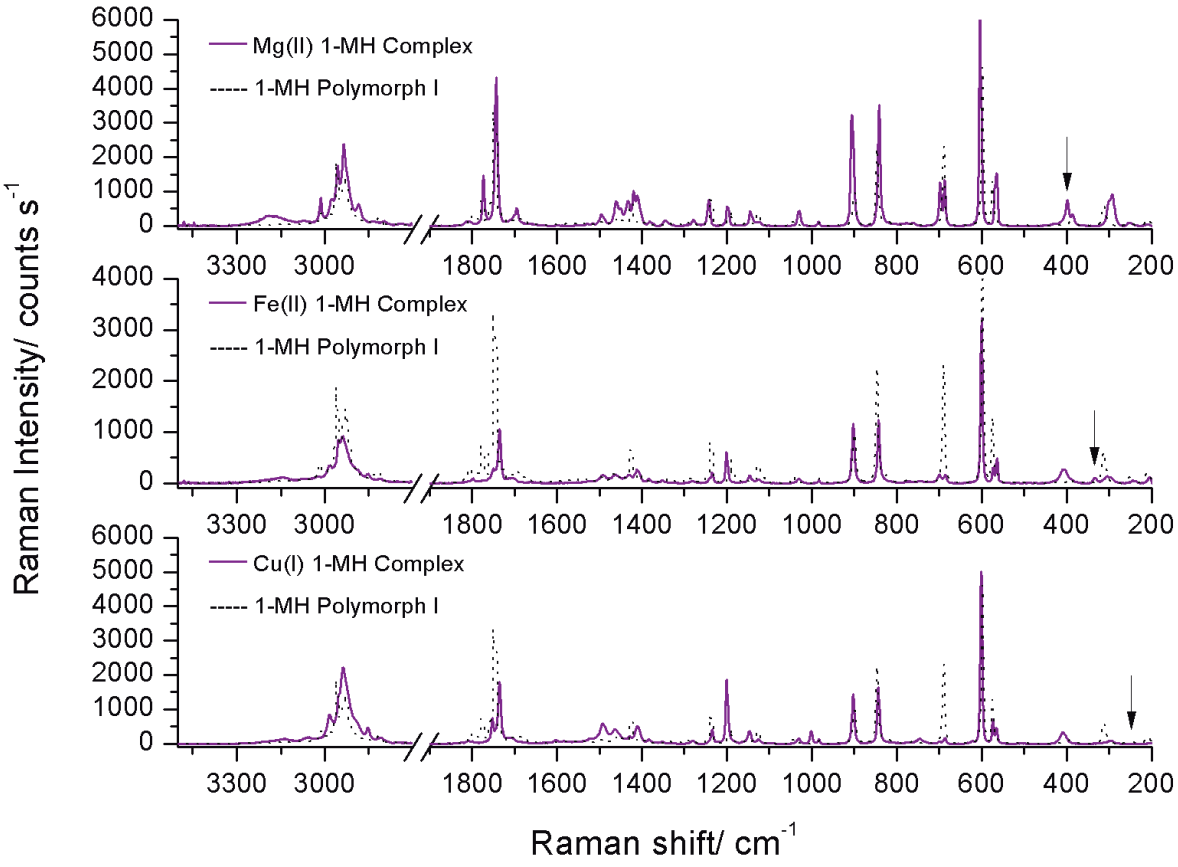

Figure 3.24 – Raman spectra of Mg (II) 1-MH, Fe (II) 1-MH and Cu (I) 1-MH coordination complexes compared with the 1-MH commercial sample (polymorph I) spectrum. Arrows pointing to the new bands corresponding to the ligand-metal bonds.

Chapter 4

Conclusions and perspectives for the future

Chapter 4

Conclusions and perspectives for the future

In this work, the FTIR spectra of monomeric 1-MH, 5-MH and 5-HAA molecules isolated in argon matrices were recorded and interpreted. The assignment of the vibrational modes were done based on DFT (B3LYP)/6-311++G(d,p) theoretical calculations and on normal coordinate analysis.

The molecular structure and the detailed electronic structure in the ground state of the three compounds were also theoretically investigated through natural bond orbital (NBO) analysis. The symmetry of the structures that correspond to the minima in the potential energy surfaces of the molecules were determined, being C_s for 1-MH and C_1 for 5-MH and 5-HAA. 1-MH, 5-MH and 5-HAA mesomeric structures help to understand the interesting fact, observed in all three molecules, that NBO partial π charge is superior in O7 atom than in O9 atom and the π charge in N3 atom is superior than in N1 atom, as result of the predominant stabilizing interactions between the molecule orbitals.

The 230 nm induced photolysis of monomeric matrix-isolated 1-MH was found to occur *via* two different pathways, which lead to fragmentation to one molecule of isocyanic acid, one molecule of carbon monoxide and one molecule of *N*-methyl-methylenimine in the preferred pathway, but also to two molecules of carbon monoxide and two molecules of methylenimine *via* the minor one.

The study of the thermal properties of 1-MH allowed the observation of two polymorphs of the compound, a previously reported form, I,[86] and a new form, II, which was obtained by recrystallization of 1-MH in methanol, acetone and THF solutions and also by sublimation at T = 100 ºC, p = 103 Pa, using the coldfinger technique, with water at about 20 ºC as the freezing fluid. Polymorph II converts into polymorph I upon heating in a transition that, for the neat compound at the warming rate of 10 ºC min^{-1}, extends from ca. 110 to 135 ºC. This transition was observed by DSC, PLTM and Raman spectroscopy techniques. The H-bond energies in both polymorphs were estimated from the comparison of the positions of the NH stretching, in-pane bending and out-of-plane rocking bands for the neat solid compound spectrum and for the matrix-isolated molecule. It was concluded that, at room temperature, polymorph II has a slightly weaker average H-bond network than polymorph I. This estimation was confirmed by the single crystal X-ray diffraction measurements, where the structure of polymorph II (orthorhombic; polymorph I is monoclinic) was presented for the first time.

The 5-MH thermal analysis study allowed the observation of four different polymorphs of the compound, including the commercial one, which melts at ca. 147 ° C. Polymorphs II (that was obtained by recrystallization in THF solutions and also by the recrystallization of the melted compound), III and IV (that were also obtained by recrystallization of the melted compound) have melting points of approximately 143,

120 and 94-96 ºC, respectively. The first three polymorphic forms were characterized by DSC, PLTM and Raman spectroscopy techniques, while polymorph IV was only characterized by the latter two techniques.
The investigation of the thermal properties performed on 5-HAA revealed the existence of five polymorphs of the compound. The commercial polymorphic form, labeled as polymorph I, presents a melting point of ca. 214 ºC. 5-HAA recrystallization in THF solution lead to polymorphs II and III, which have melting points of approximately 184-185 ºC and 175-178 ºC, respectively. Polymorph IV was formed by recrystallization in 1,4-dioxane solution and it was found to convert into polymorph V, which melts at about 198-200 ºC. All five polymorphs were observed by PLTM technique, but only polymorphs I, II, III and IV were successfully characterized by Raman spectroscopy.
Three novel 1-MH metal complexes were synthetized, where the central metal ions were Mg (II), Fe (II) and Cu (I). The Raman spectroscopy studies of those complexes pointed out that Mg(II) 1-MH complex is formed by a Mg–O bond, while 1-MH binds to Fe(II) and Cu(I) *via* the deprotonated nitrogen. These results are in agreement with the HSAB principle.

For future work, it would be very interesting to obtain the crystallographic structures and IR spectra of all different polymorphs of 5-MH and 5-HAA molecules, and try to correlate their different H-bond energies with the different solvents used in their recrystallization.
There is also the intention to study the UV-induced photolysis of both 5-MH and 5-HAA molecules isolated in cryogenic matrices.
Also, there is the ambition to continue the investigation on hydantoins metal complexes, once the crystallographic structures of the already synthesized 1-MH complexes are resolved.

Bibliography

(1) Ananda Kumar, C. S.; Kavitha, C. V.; Vinaya, K.; Prasad, S. B. B.; Thimmegowda, N. R.; Chandrappa, S.; Raghavan, S. C.; Rangappa, K. S. *Invest. New Drugs* **2009**, *27* (4), 327.

(2) Block, S. S. *Disinfection, sterilization, and preservation*; Lippincott Williams & Wilkins, 2001.

(3) Kavitha, C. V; Nambiar, M.; Ananda Kumar, C. S.; Choudhary, B.; Muniyappa, K.; Rangappa, K. S.; Raghavan, S. C. *Biochem. Pharmacol.* **2009**, *77* (3), 348.

(4) Sarges, R.; Schnur, R. C.; Belletire, J. L.; Peterson, M. J. *J. Med. Chem.* **1988**, *31* (1), 230.

(5) Yang, K.; Tang, Y.; Iczkowski, K. A. *Am. J. Transl. Res.* **2010**, *2* (1), 88.

(6) Comber, R. N.; Reynolds, R. C.; Friedrich, J. D.; Manguikian, R. A.; Buckheit, R. W.; Truss, J. W.; Shannon, W. M.; Secrist, J. A. *J. Med. Chem.* **1992**, *35* (19), 3567.

(7) Cruz-Cabeza, A. J.; Schwalbe, C. H. *New J. Chem.* **2012**, *36* (6), 1347.

(8) Allen, F. H. *Acta Crystallogr. B.* **2002**, *58* (Pt 3 Pt 1), 380.

(9) Amharar, Y.; Petit, S.; Sanselme, M.; Cartigny, Y.; Petit, M.-N.; Coquerel, G. *Cryst. Growth Des.* **2011**, *11* (6), 2453.

(10) Bruno, I. J.; Cole, J. C.; Edgington, P. R.; Kessler, M.; Macrae, C. F.; McCabe, P.; Pearson, J.; Taylor, R. *Acta Crystallogr. B.* **2002**, *58* (Pt 3 Pt 1), 389.

(11) Coquerel, G.; Petit, M. N.; Robert, F.; IUCr. *Acta Crystallogr. Sect. C Cryst. Struct. Commun.* **1993**, *49* (4), 824.

(12) Coquerel, G.; Petit, S. *J. Cryst. Growth* **1993**, *130* (1-2), 173.

(13) Courvoisier, L.; Mignot, L.; Petit, M. N.; Coquerel, G. *Org. Process Res. Dev.* **2003**, *7* (6), 1007.

(14) Yu, F.-L.; Schwalbe, C. H.; Watkin, D. J. *Acta Crystallogr. Sect. C Cryst. Struct. Commun.* **2004**, *60* (10), 714.

(15) Ildiz, G. O.; Boz, I.; Unsalan, O. *Opt. Spectrosc.* **2012**, *112* (5), 665.

(16) Ildiz, G. O.; Nunes, C. M.; Fausto, R. *J. Phys. Chem. A* **2013**, *117* (4), 726.

(17) Jensen, F. *Introduction to Computational Chemistry*; John Wiley & Sons, 2007.

(18) Lewars, E. G. *Computational Chemistry*; Springer Netherlands: Dordrecht, 2011.

(19) Parr, R. G.; Yang, W. *Density-functional theory of atoms and molecules*; Oxford University Press, 1989.

(20) Szabo, A.; Ostlund, N. S. *Modern quantum chemistry : introduction to advanced electronic structure theory*; Dover Publications, 1996.

(21) Hohenberg, P.; Kohn, W. *Phys. Rev.* **1964**, *136* (3B), 864.

(22) Kohn, W.; Sham, L. J. *Phys. Rev.* **1965**, *140* (4A), 1133.

(23) Fermi, E. *Rend. Accad. Lincei.* **1927**, *6*, 602.

(24) Dirac, P. *Math. Proc. Cambridge* **1930**, *3*, 376.

(25) Thomas, L. H. *Math. Proc. Cambridge Philos. Soc.* **1927**, *23* (05), 542.

(26) Becke, A. D. *Phys. Rev. A* **1988**, *38* (6), 3098.

(27) Perdew, J. P.; Yue, W. *Phys. Rev. B* **1986**, *33* (12), 8800.

(28) Perdew, J. P.; Wang, Y. *Phys. Rev. B* **1992**, *45* (23), 13244.

(29) Lee, C.; Yang, W.; Parr, R. G. *Phys. Rev. B* **1988**, *37* (2), 785.

(30) Miehlich, B.; Savin, A.; Stoll, H.; Preuss, H. *Chem. Phys. Lett.* **1989**, *157* (3), 200.

(31) Vosko, S. H.; Wilk, L.; Nusair, M. *Can. J. Phys.* **1980**, *58* (8), 1200.

(32) McLean, A. D.; Chandler, G. S. *J. Chem. Phys.* **1980**, *72* (10), 5639.

(33) Clark, T.; Chandrasekhar, J.; Spitznagel, G. W.; Schleyer, P. V. R. *J. Comput. Chem.* **1983**, *4* (3), 294.

(34) Frisch, M. J.; Pople, J. A.; Binkley, J. S. *J. Chem. Phys.* **1984**, *80* (7), 3265.

(35) Wilson, E.; Decius, J.; Cross, P. **2012**.

(36) Fausto, R. In *Química Síntese e Estrutura*; Burrows, H. D., Pereira, M. M., Eds.; Escolar Editora: Lisboa, 2006; pp 109–168.

(37) Turrell, G.; Turrell, G. In *Encyclopedia of Analytical Chemistry*; John Wiley & Sons, Ltd: Chichester, UK, 2006.

(38) Whittle, E.; Dows, D. A.; Pimentel, G. C. *J. Chem. Phys.* **1954**, *22* (11), 1943.

(39) Dunkin, I. R. *Matrix-isolation techniques : a practical approach*; Oxford University Press, 1998.

(40) *Low Temperature Molecular Spectroscopy*; Fausto, R., Ed.; Springer Netherlands: Dordrecht, 1996.

(41) Meier, R. J. *Vib. Spectrosc.* **2007**, *43* (1), 26.

(42) Kayser, D. A.; Ault, B. S. *J. Phys. Chem. A* **2003**, *107* (33), 6500.

(43) Fausto, R.; Gómez-Zavaglia, A. In *Photochemistry*; Royal Society of Chemistry: Cambridge; pp 72–109.

(44) Fausto, R.; Maçôas, E. M. . *J. Mol. Struct.* **2001**, *563*, 27.

(45) Perutz, R. N. *Chem. Rev.* **1985**, *85* (2), 77.

(46) Lotta, T.; Murto, J.; Räsänen, M.; Aspiala, A. *J. Mol. Struct.* **1984**, *114*, 333.

(47) Lotta, T.; Murto, J.; Räsänen, M.; Aspiala, A. *Chem. Phys.* **1984**, *86* (1-2), 105.

(48) Barnes, A. J. *J. Mol. Struct.* **1984**, *113*, 161.

(49) Fausto, R.; Maçôas, E. M. S.; Kulbida, A. *J. Mol. Struct.* **1999**, *480*, 83.

(50) Lopes, S.; Gómez-Zavaglia, A.; Fausto, R. *Phys. Chem. Chem. Phys.* **2006**, *8* (15), 1794.

(51) Marushkevich, K.; Khriachtchev, L.; Lundell, J.; Räsänen, M. *J. Am. Chem. Soc.* **2006**, *128* (37), 12060.

(52) Marushkevich, K.; Khriachtchev, L.; Räsänen, M. *Phys. Chem. Chem. Phys.* **2007**, *9* (43), 5748.

(53) Gómez-Zavaglia, A.; Fausto, R. *J. Phys. Chem. A* **2004**, *108* (34), 6953.

(54) Olbert-Majkut, A.; Mielke, Z.; Tokhadze, K. G. *Chem. Phys.* **2002**, *280* (3), 211.

(55) Atkins, P. W. *Physical Chemistry*, 4th ed.; Oxford University Press: Oxford, 1992.

(56) Stuart, B. H. *Infrared Spectroscopy: Fundamentals and Applications*; Wiley: Chischester, UK, 2004.

(57) Larkin, P. J. *Infrared and Raman Spectroscopy: Principles and Spectral Interpretation*; Elsevier: Amsterdam, The Netherlands, 2011.

(58) Schrader, B.; Bougeard, D. *Infrared and Raman spectroscopy : methods and applications*; VCH, 1995.

(59) Smekal, A. *Naturwissenschaften* **1923**, *11* (43), 873.

(60) Raman, C. V.; Krishnan, K. S. *Nature* **1928**, *121* (3048), 501.

(61) Landsberg, G.; Mandelstam, L. *Naturwissenschaften* **1928**, *16*, 558.

(62) Singh, R. *Phys. Perspect.* **2002**, *4* (4), 399.

(63) Smith, E.; Dent, G. *Modern Raman spectroscopy : a practical approach*; J. Wiley, 2005.

(64) Long, D. A. *The Raman Effect*; John Wiley & Sons, Ltd: Chichester, UK, 2002.

(65) McCreery, R. L. *Raman Spectroscopy for Chemical Analysis*; John Wiley & Sons, Inc.: Hoboken, NJ, USA, 2000.

(66) Mojumdar, S. C.; Sain, M.; Prasad, R. C.; Sun, L.; Venart, J. E. S. *J. Therm. Anal. Calorim.* **2007**, *90* (3), 653.

(67) Brown, M. E. *Introduction to Thermal Analysis*; 1st ed., Kluwer Academic Publishers: Dordrecht, 2004; Vol. 1.

(68) Gonsalves, A. M. d´A. R.; Serra, M. E. S.; Eusébio, M. E. S. *Esteroquímica*, 1st ed.; Imprensa da Universidade de Coimbra: Coimbra, Portugal, 2011.

(69) Chew, S.; Sim, A. In *Proceedings of 5th International Symposium on the Physical and Failure Analysis of Integrated Circuits*; IEEE; pp 181.

(70) Kuhnert-Brandstätter, M. *Thermomicroscopy in the Analysis of Pharmaceuticals*; Pergamom Press: Oxford, 1971.

(71) Nichols, G. In *Polymorphism*; Wiley-VCH Verlag GmbH & Co. KGaA: Weinheim, FRG, 2006; pp 167.

(72) McCrone, W. C. Interscience Publishers 1957.

(73) McCrone, W. C.; McCrone, L. B.; Delly, J. G. *Polarized light microscopy*; Ann Arbor Science Publishers, 1978.

(74) Charsley, E. L.; Stewart, C.; Barnes, P. A.; Parkes, G. M. B. *J. Therm. Anal. Calorim.* **2003**, *72* (3), 1087.

(75) Clearfield, A.; Reibenspies, J. H.; Bhuvanesh, N. *Principles and applications of powder diffraction*; John Wiley and Sons, 2008.

(76) Fricker, S. P. *Dalt. Trans.* **2007**, *15* (43), 4903.

(77) Lippard, S. J. *Nat. Chem. Biol.* **2006**, *2* (10), 504.

(78) David, S. S.; Meggers, E. *Curr. Opin. Chem. Biol.* **2008**, *12* (2), 194.

(79) Cohen, S. M. *Curr. Opin. Chem. Biol.* **2007**, *11* (2), 115.

(80) Crichton, R. R. *Biological inorganic chemistry a new introduction to molecular structure and function*; Elsevier, 2012.

(81) Haas, K. L.; Franz, K. J. *Chem. Rev.* **2009**, *109* (10), 4921.

(82) Malik, N. A.; Sadler, P. J.; Neidle, S.; Taylor, G. L. *J. Chem. Soc. Chem. Commun.* **1978**, *16*, 711.

(83) Laurent, J. P.; Lepage, P.; Dahan, F. *J. Am. Chem. Soc.* **1982**, *104* (25), 7335.

(84) Puszynska-Tuszkanow, M.; Staszak, Z.; Misiaszek, T.; Klepka, M. T.; Wolska, A.; Drzewiecka-Antonik, A.; Faltynowicz, H.; Cieslak-Golonka, M. *Chem. Phys. Lett.* **2014**, *597*, 94.

(85) Puszyńska-Tuszkanow, M.; Grabowski, T.; Daszkiewicz, M.; Wietrzyk, J.; Filip, B.; Maciejewska, G.; Cieślak-Golonka, M. *J. Inorg. Biochem.* **2011**, *105* (1), 17.

(86) Puszyńska-Tuszkanow, M.; Daszkiewicz, M.; Maciejewska, G.; Staszak, Z.; Wietrzyk, J.; Filip, B.; Cieślak-Golonka, M. *Polyhedron* **2011**, *30* (12), 2016.

(87) Pearson, R. G.; Songstad, J. *J. Am. Chem. Soc.* **1967**, *89* (8), 1827.

(88) M. J. Frisch, G. W. Trucks, H. B. Schlegel, G. E. Scuseria, M. A. Robb, J. R. Cheeseman, G. Scalmani, V. Barone, B. Mennucci, G. A. Petersson, H. Nakatsuji, M. Caricato, X. Li, H. P. Hratchian, A. F. Izmaylov, J. Bloino, G. Zheng, J. L. Sonnenberg, M. Had, and D. J. F. Gaussian, Inc: Wallingford CT 2009.

(89) Becke, A. D. *Phys. Rev. A* **1988**, *38* (6), 3098.

(90) Lee, C.; Yang, W.; Parr, R. G. *Phys. Rev. B* **1988**, *37* (2), 785.

(91) McLean, A. D.; Chandler, G. S. *J. Chem. Phys.* **1980**, *72* (10), 5639.

(92) Schachtschneider, J. H.; Mortimer, F. *Vibrational Analysis of Polyatomic Molecules, VI: FORTRAN IV Vibrational Analysis of Polyatomic Molecules, VI*; Shell Development: Emeryville, CA, 1969.

(93) Pulay, P.; Fogarasi, G.; Pang, F.; Boggs, J. E. *J. Am. Chem. Soc.* **1979**, *101* (10), 2550.

(94) Reed, A. E.; Curtiss, L. A.; Weinhold, F. *Chem. Rev.* **1988**, *88* (6), 899.

(95) Weinhold, F.; Landis, C. R. *Valency and Bonding: A Natural Bond Orbital Donor-Acceptor Perspective*; Cambridge University Press: New York, 2005.

(96) Sabbah (France, Chairman), R.; Xu-wu (China), A.; Chickos (USA), J. S.; Leitão (Portugal), M. L. P.; Roux (Spain), M. V.; Torres (México), L. A. *Thermochim. Acta* **1999**, *331* (2), 93.

(97) Bruker AXS Inc.: Madison, Wisconsin, USA 2006.

(98) Sheldrick, G. M. *Acta Crystallogr. Sect. C Struct. Chem.* **2015**, *71* (1), 3.

(99) Fox, M. A.; Whitesell, J. K. *Organische Chemie : Grundlagen, Mechanismen, bioorganische Anwendungen*; Spektrum Akadem. Verl, 1995.

(100) Fausto, R.; de Carvalho, L. A. E. B.; Teixeira-Dias, J. J. C.; Ramos, M. N. *J. Chem. Soc. Faraday Trans. 2* **1989**, *85* (12), 1945.

(101) McKean, D. C. *Chem. Soc. Rev.* **1978**, *7* (3), 399.

(102) Castiglioni, C.; Gussoni, M.; Zerbi, G. *J. Chem. Phys.* **1985**, *82* (8), 3534.

(103) Fausto, R. *J. Mol. Struct. THEOCHEM* **1994**, *315*, 123.

(104) Wiberg, K. B.; Laidig, K. E. **2002**.

(105) Teles, J. H.; Maier, G.; Andes Hess, B.; Schaad, L. J.; Winnewisser, M.; Winnewisser, B. P. *Chem. Ber.* **1989**, *122* (4), 753.

(106) Abe, H.; Takeo, H.; Yamada, K. M. . *Chem. Phys. Lett.* **1999**, *311* (3), 153.

(107) Halonen, L.; Duxbury, G. *Chem. Phys. Lett.* **1985**, *118* (3), 246.

(108) Gómez-Zavaglia, A.; Reva, I. D.; Frija, L.; Cristiano, M. L.; Fausto, R. *J. Phys. Chem. A* **2005**, *109* (35), 7967.

(109) de Oliveira, G.; Martin, J. M. L.; Silwal, I. K. C.; Liebman, J. F. *J. Comput. Chem.* **2001**, *22*, 1297.

(110) Nogueira, B. A.; Ildiz, G. O.; Canotilho, J.; Eusébio, M. E. S.; Fausto, R. *J. Phys. Chem. A.* **2014**, *118(31)*, 5994.

(111) Shen, J. X.; Brodbelt, J. *J. Mass Spectrom.* **1996**, *31* (12), 1389.

(112) Corral, R. A.; Orazi, O. O.; Duffield, A. M.; Djerassi, C. *Org. Mass Spectrom.* **1971**, *5* (5), 551.

(113) Schoch, S.; Blos, I.; Rüdiger, W. *Org. Mass Spectrom.* **1975**, *10* (9), 797.

(114) Rozenberg, M. S. *Spectrochim. Acta Part A Mol. Biomol. Spectrosc.* **1996**, *52* (11), 1559.

(115) Rozenberg, M.; Shoham, G.; Reva, I.; Fausto, R. *Spectrochim. Acta Part A Mol. Biomol. Spectrosc.* **2004**, *60* (1), 463.

(116) Ferraro, J. R. *Low-Frequency Vibrations of Inorganic and Coordination Compounds*; Springer US: Boston, MA, 1995.

(117) Nakamoto, K. *Infrared and Raman Spectra of Inorganic and Coordination Compounds*; John Wiley & Sons, Inc.: Hoboken, NJ, USA, 2008.

(118) Duncan, J. F.; Mok, K. F. *Aust. J. Chem.* **1966**, *19*, 701.

(119) Helios, K.; Wysokí Nski, R.; Pietraszko, A.; Michalska, D. *Vib. Spectrosc.* **2010**, *55*, 207.

(120) Parker, F. S. *Applications of Infrared Spectroscopy in Biochemistry, Biology, and Medicine*; Springer US: Boston, MA, 1971.

(121) Pearson, R. G. *J. Am. Chem. Soc.* **1963**, *85* (22), 3533.

(122) Koch, E.-C. *Propellants, Explos. Pyrotech.* **2005**, *30* (1), 5.